Civil Engineering

Civil Engineering Research

Modelling of Tsunami Ge
Underwater

prepared for: EQC Research Foundation

EQC Ref:6UNI1/506
2006-02

ISSN - 0110-3326

06

750
1596

University Project

Modelling of Tsunami Generated By Underwater Landslides

Reference

6UNI1/506

Project Duration

1 March 2005 – 28 February 2006

Prepared by

Langford P. Sue and Roger I. Nokes
Department of Civil Engineering, University of Canterbury
Christchurch, New Zealand

Roy A. Walters
National Institute for Water and Atmospheric Research
Christchurch, New Zealand

For

Earthquake Commission (EQC) Research Foundation

February 2006

Table of Contents

Technical Abstract

Tsunami are a fascinating but potentially devastating natural phenomenon that have occurred regularly throughout history along New Zealand's shorelines, and around the world. With increasing population and the construction of infrastructure in coastal zones, the effect of these large waves has become a major concern. Many natural phenomena are capable of creating tsunamis. Of particular concern is the underwater landslide-induced tsunami, due to the potentially short warning before waves reach the shore.

In an effort to test numerical models of underwater landslides, a number of benchmark experiments have been undertaken and published in the scientific literature. These benchmarks include two-dimensional and three-dimensional experiments with solid objects sliding down a submerged surface. From a range of landslide accelerations and initial submergences, water levels were measured, typically at a few points with electrical gauges.

Following this general procedure, sets of laboratory experiments are being undertaken at the University of Canterbury. A unique feature of these experiments is that a method has been developed to measure water surface variation continuously in both space and time rather than at discrete points. Water levels are obtained using an optical technique based on laser induced fluorescence, which is shown to be comparable in accuracy and resolution to traditional electrical point wave gauges. The ability to capture the spatial variations of the water surface along with the temporal changes has proven to be a powerful tool with which to study the wave generation process.

In the experiments, the landslide density and initial submergence are varied and detailed information of wave heights, lengths, propagation speeds, and shore run-up is measured. Particle tracking velocimetry is used to record the landslide position time-history and sub-surface water velocities. The experiments highlight the non-linear interaction between slider kinematics and initial submergence, and the wave field.

By comparing the instantaneous position and speed of the landslide relative to the wave field, it is found that the 1st crest forms over the front half of the landslide and a trough forms over the rear. The point at which these two waves meet is centred above the landslide centre of mass and remains there as the block slides down the slope. Water surface profiles also indicate that the wavelengths of individual waves increase as they propagate into deeper water. Fourier analysis of the wave profiles indicates an absence of waves with lengths shorter than the landslide length. The dispersion of the waves is also evident, as waves further behind in the wave train propagate more slowly than those in front. New waves are continually generated at the trailing end of the wave train.

The ability to resolve water levels spatially and temporally allows wave potential energy time histories to be calculated. It is observed that the time of occurrence of maximum wave potential energy is later than that for the maximum landslide kinetic energy. Conversion efficiencies range from 32.9%-50.4% for landslide potential energy into landslide kinetic energy. Rates for conversion between landslide kinetic energy and wave potential energy range between 2.8% and 13.8%.

The wave trough initially generated above the rear end of the landslide propagates in both upstream and downstream directions. The upstream-travelling trough causes the large initial draw-down at the shore. The magnitude of the maximum run-down is directly related to the maximum downstream-propagating 1^{st} wave trough amplitude. A wave crest generated by the landslide as it decelerates at the bottom of the slope causes the maximum wave run-up height observed at the shore.

The visualisation of sub-surface velocities using particle tracking velocimetry allows the generation mechanism of the wave field to be examined. The upward flow over the front of the sliding block creates a region of high pressure that forces the water directly above into a wave crest. The accelerating flow over the top and rear of the landslide creates a region of low pressure that draws down the water surface into a wave trough. Once generated the crest is free to propagate, whereas the trough remains with the landslide until the block begins to slow at the base of the slope, and the associated low pressure region dissipates. It is also observed that several large rotating eddies are left behind in the wake of the sliding block. The fluid particles below the waves move in elliptical orbits that tend to flatten towards the bottom of the water column, with purely horizontal motions at the flume floor.

Simplified Abstract

Tsunami are a fascinating but potentially devastating natural phenomenon that have occurred regularly throughout history along New Zealand's shorelines, and around the world. With increasing population and the construction of infrastructure in coastal zones, the effect of these large waves has become a major concern. Many natural phenomena are capable of creating tsunamis. Of particular concern is the underwater landslide-induced tsunami, due to the potentially short warning before waves reach the shore.

The underwater landslide research community have designed several standardised experiments to test the accuracy of computer tsunami models. These standard tests usually model underwater landslides with solid blocks sliding down submerged slopes. The landslide mass and initial submergence, the starting distance of the landslide below the water surface, are varied and the wave heights are measured at a few points with electrical sensors.

Using a similar approach, several laboratory tests are being performed at the University of Canterbury. A new method, shown to be as accurate as traditional electrical sensors, has been developed to measure the water levels at all positions within the wave tank. This technique involves illuminating the water with fluorescent dye and recording its motion with a digital video camera. The ability to measure the entire water surface, instead of at a few specific points, has allowed the tsunami generation process to be looked at in more detail.

In these latest experiments, the mass and initial submergence of the landslide are varied and information about the waves, such as height, shape, speed, and run-up at the shore, is measured. The speed and acceleration of the model landslide and the motions of the water below the waves are also recorded. The experiments highlight the complex interaction between the generated waves and the landslide.

By comparing the position and speed of the landslide relative to the waves, it is found that the 1st crest forms over the front half of the landslide and a trough forms over the rear. The point at which these two waves meet is located above the centre of the landslide as it slides down the slope. The changing shape of the water surface also indicates that the wavelengths of individual waves increase as they propagate into deeper water. Waves shorter than the length of the landslide are not generated. Waves further behind in the wave train propagate more slowly than those in front, and new waves are continually generated at the trailing end of the wave train.

The ability to measure water levels across space and time allows wave potential energy time histories to be calculated. It is observed that the maximum wave potential energy occurs later than the maximum landslide kinetic energy. Between 32.9% and 50.4% of the landslide potential energy is converted into landslide kinetic energy. Between 2.8% and 13.8% of landslide kinetic energy is converted into the potential energy of the waves.

The wave trough that initially forms above the rear end of the landslide propagates in both upstream and downstream directions. The upstream-travelling trough causes the large initial draw-down at the shore. A wave crest generated by the landslide as it suddenly slows at the bottom of the slope causes the maximum wave run-up height observed at the shore.

The visualisation of the velocities of the water beneath the surface allows the generation mechanism of the wave field to be examined. The water is forced up over the block as it slides, forming the 1st wave crest. The water over the block travels faster than the surrounding water and causes the water above the landslide to form a wave trough. Once generated the crest propagates freely, whereas the trough remains attached to the slider until it reaches the base of the slope. Several large rotating eddies are left behind in the wake of the sliding block. The fluid particles below the waves move in elliptical orbits that tend to flatten towards the bottom of the water column, with purely horizontal motions at the flume floor.

Nomenclature

block E_p	Landslide potential energy
C	Constant
ΔC	Abe's source region correction factor
c	Soil cohesion
d	Initial water depth directly above the landslide centre of mass
dv	Vertical displacement relative to initial RWG submergence
g	Acceleration of gravity
H	Horizontal distance of camera from laser light sheet
$H_{r\ max}$	Maximum tsunami run-up height
$\overline{H}_r$	Mean tsunami run-up height
IS	Initial Submergence
i_s	Soloviev's tsunami intensity
L_{crest}	Distance from camera to positive water level
L_o	Distance from camera to still water level
L_{trough}	Distance from camera to negative water level
M_t	Abe's tsunami magnitude scale
m_b	Unsubmerged mass of landslide
m_m	Imamura-Iida's tsunami magnitude scale
m_o	Mass of water displaced by the landslide
SG	Specific Gravity
t	Time
u	Horizontal landslide velocity
V	Output voltage
V	Vertical distance of camera above still water level
v	Vertical landslide velocity
v_b	Landslide volume
vel	Total landslide velocity
WL	Refraction-corrected water level (positive and negative)
$WL_{corrected}$	Water level corrected for camera angle-induced scaling errors
w	Landslide or flume width
wave E_p	Wave potential energy
x	Horizontal landslide position
y	Vertical landslide position
ϕ	Internal friction angle
η	Water level
θ	Slope angle
ρ_o	Density of water
σ	Normal stresses on the slope
τ_s	Soil shear strength
ξ	Pore water pressure

Chapter 1: Introduction

Unlike tidal waves, tsunami are not a phenomena associated with the tides, but instead are water waves generated by seismic events in and around the oceans. The word 'tsunami' originates from the Japanese word which means 'harbour wave', and has been adopted by the western world to differentiate between waves generated seismically and those related to tidal effects.

There are several reasons tsunami are hazardous. Firstly it is their size, with waves several hundred metres in height known to have occurred in the past (Murty 2003; New Scientist 2004). Secondly, tsunami can travel at considerable speeds, upwards of many hundreds of kilometres per hour. Lastly, tsunami occurrences are unpredictable. Seismic events such as earthquakes and landslides, the generation mechanisms of tsunami, occur sporadically in time and space, and not all seismic events have generated significant waves.

After the events in the Indian Ocean on the 26th of December 2004, the existence of powerful tsunami cannot be disputed. Studies of historical records and forensic analysis of coastal geology have shown significant wave events occur frequently across the world. With the increasing population in communities and the development of infrastructure around the coastal fringes, the possible impact of these large waves is becoming a major concern.

This report focuses on the class of tsunami generated by underwater landslides. Sections of sediment or rock on the seabed can slide into deeper water, and this movement translates into a disturbance on the water surface above.

Chapter 2 summarizes the literature associated with underwater landslides and the water waves that they create in nature and in the laboratory. Chapter 3 contains information pertaining to the laboratory experiments conducted at the University of Canterbury. Details of the experimental set-up are given, along with information on the methods developed to measure the wave phenomena and the equipment and computer software required. The key results are given and discussed in Chapter 4, followed by some concluding remarks in Chapter 5.

Chapter 2: Literature Review

This chapter begins with a review of basic tsunami characteristics. The major historical events from around the world and New Zealand are then presented, followed by a brief discussion of the soil mechanics of slope failures and natural sediments and their importance in the understanding of terrestrial and underwater landslides and their causes. Further background is then given with the presentation of previous experimental work on the generation and run-up of landslide tsunami waves. Lastly, the numerical simulation of these phenomena is reviewed briefly.

2.1 Tsunami Characteristics

Earthquake generated tsunami can produce large wave heights and have far-reaching effects. They are strongly related to the magnitude of the seismic event which allows tsunami heights to be estimated from the size of the earthquake (de Lange and Moon 2004). Wavelengths of these are typically several hundred kilometres, and they exhibit little wave height decay due to weak energy attenuation. Waves lose energy proportional to their frequency, with higher frequencies having greater attenuation.

For landslide-induced events, large waves are produced along areas of coast close to the source, typically 10-15 km either side of the slide area (Papadopoulos and Kortekaas 2003). Tsunami may be observed over a considerably greater distance if the landslide is exceptionally large or if it is combined with co-seismic sources. The effects of landslide tsunami are geographically constrained, but their danger lies in the short travel times compared to seismically generated waves and their higher amplitudes in the near field.

There are several indicators that a tsunami was possibly landslide-generated as opposed to earthquake-generated. Landslide-tsunami have a more localised effect and greater dissipation, such that damage is generally isolated to small areas close to the origin, and far field effects may be negligible. However, this near field damage may be more severe than from seismically generated tsunami. Damage may also be more intense in certain areas due to directivity associated with radiation away from a point source. Tsunami with landslide origins often have fewer waves in the wave train, and attenuate more rapidly due to their higher frequencies. Submarine landslide tsunami can be distinguished from the earthquake generated tsunami in a co-seismic event by earlier or delayed arrival times or waves larger than expected from an earthquake of that magnitude.

During the initial stages of a submarine landslide, the motion of the failure mass downwards pulls the water surface down. The surrounding water will be driven into this depression due to the horizontal pressure gradients. Waves then propagate due to gravitational forces, given the initial perturbation of the water surface. Wave trains travel both upslope and forward parallel with the slide, and are thus more focussed that those created by earthquakes. While there is still no consensus as to the characteristics of these waves with regard to wavelength components, linearity, and dispersion, it is clear that tsunami waves are affected significantly by the local bathymetry as they approach the shore.

Tsunami are often quantified by means of a magnitude or intensity scale. A common measure for characterising tsunami is the Imamura-Iida scale, developed in tsunami-prone Japan from approximately 100 Japanese tsunami records between 1700 and 1960 (Shuto 1991).

$$m_m = \log_2 H_{r\max} \qquad \textbf{(2.1)}$$

where m_m = Imamura-Iida's tsunami magnitude scale (dimensionless)

$H_{r\max}$ = maximum tsunami run-up height (m)

Imamura-Iida's magnitude scale is now commonly used globally. However, maximum wave run-up heights were considered too variable, so Soloviev proposed a more general scale (Horikawa and Shuto 1981).

$$i_s = \log_2(\sqrt{2}\overline{H}_r) \qquad \textbf{(2.2)}$$

where i_s = Soloviev's tsunami intensity (dimensionless)

$\overline{H}_r$ = mean tsunami run-up height along a stretch of coast (m)

Both these scales peak around a value of 4 and can produce magnitudes with negative values. Abe (1981) suggests a remedy to this with the following scale, which has become widely used.

$$M_t = \log_{10} H_{r\max} + 9.1 + \Delta C \qquad \textbf{(2.3)}$$

where M_t = Abe's tsunami magnitude scale (dimensionless)

ΔC = source region correction factor (eg. Hilo, -0.3; California, 0.2; Japan, 0.0)

On the open ocean tsunami wave amplitudes are small, noticed only as a slight swell, but as they approach the shore shoaling effects increase the wave heights. Tsunami wave heights are usually measured at the shore, where their heights are at a maximum. Run-up height is the vertical elevation reached by the wave relative to the intersection of the still water level with the original beach location. Run-up length is the horizontal distance the tsunami propagated inland, also measured relative to the beach-to-still water level intersection.

2.2 Historical Underwater Landslide-Induced Tsunami

Tsunami waves have been recorded throughout history, with the earliest accounts from as long ago as 4000 years in China, 2500 years in the Mediterranean, and 1300 years in Japan (Bryant 2001). Recent underwater landslide-induced events often quoted in the literature are those at Grand Banks in 1929, Alaska in 1964 and 1994, and Papua New Guinea in 1998. These caused widespread damage and loss of life. Tsunami created by landslides are responsible for most of Alaska's tsunami fatalities, unlike the rest of the USA. These local waves arrive in a few minutes and give little or no opportunity for warning or evacuation. New Zealand experiences a similar frequency of tsunami (seismically- and landslide-induced), with amplitudes greater than one metre, as Hawaii and Indonesia and about a third of that experienced by Japan.

One of the more recent submarine landslide events was that in Izmit Bay, Turkey, in 1999. Although still under ongoing investigation, reports of slope movements along the coast after the magnitude 7.4 Kocaeli earthquake causing a tsunami (Watts et al. 2005; Wright and Rathje 2003), illustrates the close association between landslide-generated tsunami and seismic activity. A computer recreation of the landslide is shown in Figure 2.1.

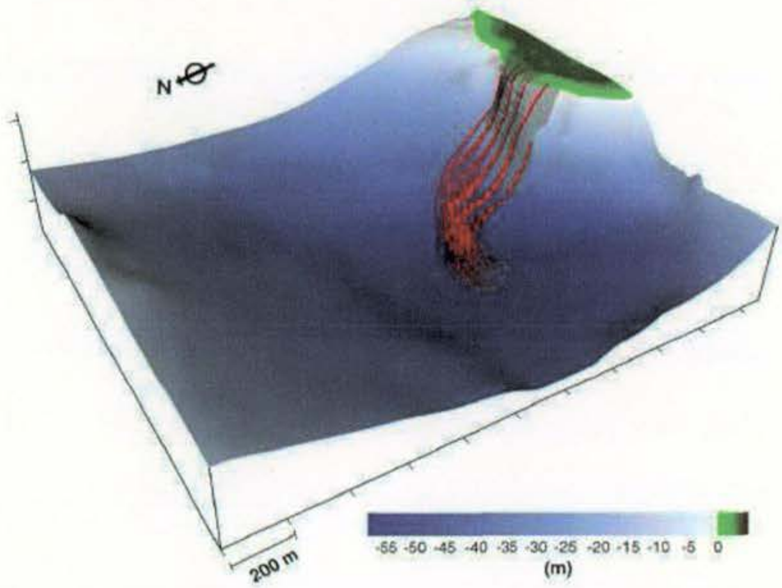

Figure 2.1. 3D computer recreation of the Izmit Bay underwater landslide (Tinti et al. 2006).

The most recent of the large tsunami occurred in 1998 along the shores of the Sissano Lagoon, Papua New Guinea. Shortly after a magnitude 7.1 earthquake, wave run-up heights of 15 m were observed along an isolated stretch of coastline. A photo of the tsunami inundation is shown in Figure 2.2. The arrival time and wave heights were inconsistent with the magnitude of the seismic event itself, spurring further investigations as to the cause. Due to the scale of devastation, a comprehensive investigation was initiated starting with survivors' accounts, on and off shore surveys, seabed imaging, geological interpretation, seismic interpretation, and computer simulations.

The earthquake originated along Northern Papua New Guinea on the boundary of the Australian and Pacific Plates. Numerical simulations indicate that this was the source of a far-reaching tsunami recorded as far away as Japan. However, further simulations show that the fault dislocation was unable to produce the time and wave height distribution observed in the near field. A submarine slump source was proposed and evidence was found to support this (Tappin et al. 2001).

From the detailed offshore surveys that were conducted, evidence was found of a large amphitheatre-shaped rotational slump, along with evidence of recent seabed disturbance (fissures, angular blocks, vertical slopes). The slide material was thought to be 750 m thick and contain 5 to 10 million m^3 of cohesive sediment (Tappin et al. 2001). This provided investigators with a possible cause for the disaster that destroyed 3 villages, badly damaged 4 others, killed 2,200 people and left 12,000 homeless.

Further evidence was found through the analysis of records from surrounding hydrophone stations. An event was recorded 13 minutes after the main shock and found to have originated within the amphitheatre structure. The exceptionally long duration and the frequency content recorded by the hydrophone indicated a slump was the source of the signal, not a fault dislocation of the seabed (Okal 2003).

The tsunami, consisting of three large waves, arrived approximately 20 minutes after the main shock. Interviews with survivors determined that all three waves, spaced about 500 m to 600 m apart, were approximately 4 m in height as they approached the shore near Sissano. Shoaling effects and coastal topography amplified this height considerably, with wave run-up heights consistently higher than 10 m along a 15 km to 20 km stretch of coastline (Imamura and Hashi 2003; Lynett et al. 2003). Observers of the tsunami wave train stated that the maximum run-up height of 15 m was due to the second of the waves, which surged up the beach atop the first wave that had not yet receded fully (Davies et al. 2003).

Figure 2.2. Looking towards Arop Community School, this photograph of the aftermath of the Papua New Guinea tsunami shows mature trees uprooted for a distance of 500 m inland (Davies et al. 2003).

The port of Swagway, Alaska, experienced landslide-generated tsunami in November 1994. 8-11 m waves were observed at the shoreline after approximately 16 km^3 of material slid down the harbour, with the death of one worker and damage to the port facilities (Murty 2003; Papadopoulos and Kortekaas 2003; Rzadkiewicz et al. 1997; Watts et al. 2005).

Another example of a seismically induced tsunami occurred on December 1992 when an earthquake with a surface magnitude of 7.5 struck the Indonesian island of Flores (Bardet et al. 2003; Tinti and Bortolucci 2000). A detailed survey followed the earthquake and tsunami. Measurements of wave run-up and penetration were found to be up to four times higher than the mean value of the area surrounding Riangkroko on the eastern flanks of the island. The maximum run-up height of 26 m, higher than that caused by the earthquake itself, was due to what was assumed to be localised submarine landslides offshore from this area, and direct evidence of coastal slumping and land sliding was consequently found. The death toll from the combined seismic and submarine landslide-generated tsunami was approximately 2,000, of which 122 were directly associated with the localised event offshore of Riangkroko.

The event at Nice, France, in 1979 is an example of how the disturbance of an initial underwater landslide can initiate subsequent larger landslides. An underwater slide with an initial volume of 10 million m^3 situated 15 km offshore evolved into a turbidity current, with a volume of 100 million m^3, and severed several submarine cables off Nice (Hampton et al. 1996; Papadopoulos and Kortekaas 2003; Rzadkiewicz et al. 1997). The small tsunami created a 3m draw-down along the previously stable Port of Nice, increasing shear stresses in the slope by only 1.5% to 2% (Wright and Rathje 2003). However, this small increase was enough to induce flow liquefaction in a sand layer and progressive failure of the slope.

A large submarine landslide involving between 10 million m^3 and 55 million m^3 of material occurred on the 27th April, 1975 in Kitimat Inlet, British Columbia, Canada (Jiang and Leblond 1992; Murty 2003). This generated at least two large waves, the height of the first was estimated to be roughly 8 m (Rzadkiewicz et al. 1997). The cause of this landslide was thought to be a combination of a low tide, the loading of man-made structures, and the expansive pressure of gas within the sediment (Hampton et al. 1996).

On Good Friday, 27 March 1964, one of the largest measured earthquakes in North America struck the Prince William Sound region of Alaska. The southward movement of Alaska over the Pacific Plate created a shallow dip fault rupture displacing 115-120 km^3 of crust. This displaced 25,000 km^3 of water, forming a large trans-Pacific tsunami. However, this was only one of the three major causes of tsunami to affect Prince William Sound during that time. The second was due to the numerous local landslides, and the third occurred much later and was due to resonance effects in the Port of Valdez region.

Large landslide-generated wave run-up was experienced at several communities along the coast of Prince William Sound. Waves were created immediately at Seward and Valdez following the failure of the steep submerged slopes of Resurrection Bay and Port Valdez respectively. These slides were peculiar in that they originated underwater but retrogressed back up the shore, sinking sections of coastal land and port facilities (Finn 2003; Hampton et al. 1996).

At Seward, the initial smaller slides created waves that initially drew down the water level at the coast, as observed by the rapid drop of ships at their berths at the Standard Oil Dock. The increase in pore water pressure due to the removal of water triggered a flow (shear or liquefaction) failure along a 1 km long section of waterfront containing the docks, rail yard, and oil tanks. This coastal land slid into Resurrection Bay approximately 40 seconds after the start of the strong shaking. This generated several 9 m to 10 m-high localised tsunami that struck the shore moments later bringing back with it burning oil from the damaged oil tanks. All this damage was due to the local slope failures, and it wasn't until 30 minutes later that the earthquake-generated tsunami arrived at Seward, causing further damage. In all, 13 people died at Seward.

The town of Seward was situated on the fan-delta of Lowell Creek, and it was the face of this that failed, destroying much of the town's infrastructure. The southern end of the port's breakwater was originally standing in 3 m of water, but was in 40 m of water after the landslide. The landslide material consisted of loose sediments, deposited at the angle of repose, and rocky debris. It also contained 10 m to 15 m high blocks of soil. This material extended for 500 m offshore at a slope of 25°, tapering to 5° at the toe of the slope (Lee et al. 2003). The loose sediments were severely stirred up and carried a great distance, and finally settled out as a thin layer on the floor of Resurrection Bay.

At Valdez, a similar submarine landslide was generated at the entrance to the port by a collapse of Shoup Glacier's terminal moraine. The tsunami generated carried debris as high as 67 m above sea level. Like Seward, Valdez itself was situated on a steep-fronted outwash delta. A 180 m wide and 1.2 km stretch of coast slid into the fjord, causing a 9 m high tsunami to surge through the remains of the town only minutes later. In all, 32 people were lost at Valdez.

Of the 106 lives taken by the various tsunami related to the Good Friday earthquake, 82 were attributed to the localised landslide events (Bryant 2001).

It was in the aftermath of the tsunami generated near Unimak Island along the Aleutian Trench in 1946 that the Pacific Tsunami Warning Centre was established to give coastal communities warning of trans-Pacific tsunami. This tsunami was created by a very large submarine landslide involving approximately 200 million m^3 that was triggered by an earthquake with a surface magnitude of 7.1. The head of the slide originated on the continental shelf in 150 m of water and came to rest at a depth of 6000 m in the Aleutian Trench, having slid over a mean slope of 4°. The tsunami wave ran up to a height of 35 m at Scott Cap lighthouse, directly onshore from the slide location (Enet et al. 2003; Grilli et al. 2002; Watts et al. 2005).

An earthquake, with a surface magnitude of 7.2, off the coast of Newfoundland and Nova Scotia, Canada, in 1929 induced many submarine landslides along Grand Banks. The slides, with a variety of slump depths ranging from 2 m thick to 30 m thick, occurred in 600 m of water along a 260 km width of the continental slope, which culminated over several hours into a large debris flow and turbidity current. This slide was famous as it was the first observation of a debris flow and turbidity current, detected as it severed several submarine Trans-Atlantic cables lying in its path. Later analysis of the sequence and times the cables were severed indicate the slide moved at an average velocity of 3 m/s, a maximum velocity of 20 m/s, and involved up to 500,000 million m^3 of material, with the turbidity current having travelled down slope at least 700 km from the source. After 11 hours of evolution the turbidity current reached its terminus having grown to a thickness of several hundred metres, eventually covering an area of 160,000 km^2 of seabed in a turbidite layer several metres thick (Fine et al. 2005; Jiang and Leblond 1992; Ruff 2003; Rzadkiewicz et al. 1997; Tinti and Bortolucci 2000).

The Grand Banks slides initiated a tsunami that caused damage and loss of life along Newfoundland and Nova Scotia's shores. Forty isolated fishing communities on the Burin Peninsula on the south coast of Newfoundland, directly opposite the headwall of the larger slides, were inundated by a 3 m high wave approximately two and a half hours after the earthquake. Run-up heights of 2 m to 7 m were observed, with a maximum value of 27 m at Taylors Bay. Diagrams of the Grand Banks area affected by the tsunami are presented in Figure 2.3. The waves approached the shore at 140 km/hr with two further waves following the first. The death toll from this event was 28 in Newfoundland, and due to the isolation of these villages news of the disaster did not reach the world until two days later. The damage to the communities was compounded as the tsunami surged in on top of a high spring tide. Nova Scotia felt a less devastating effect of the tsunami, with the death of only one person, as the wave had dissipated as it radiated out from the source area. A 0.5 m high wave was measured in Halifax, and was detected as far away as South Carolina and Portugal (Bryant 2001). The tsunami wave travel times are shown in Figure 2.4.

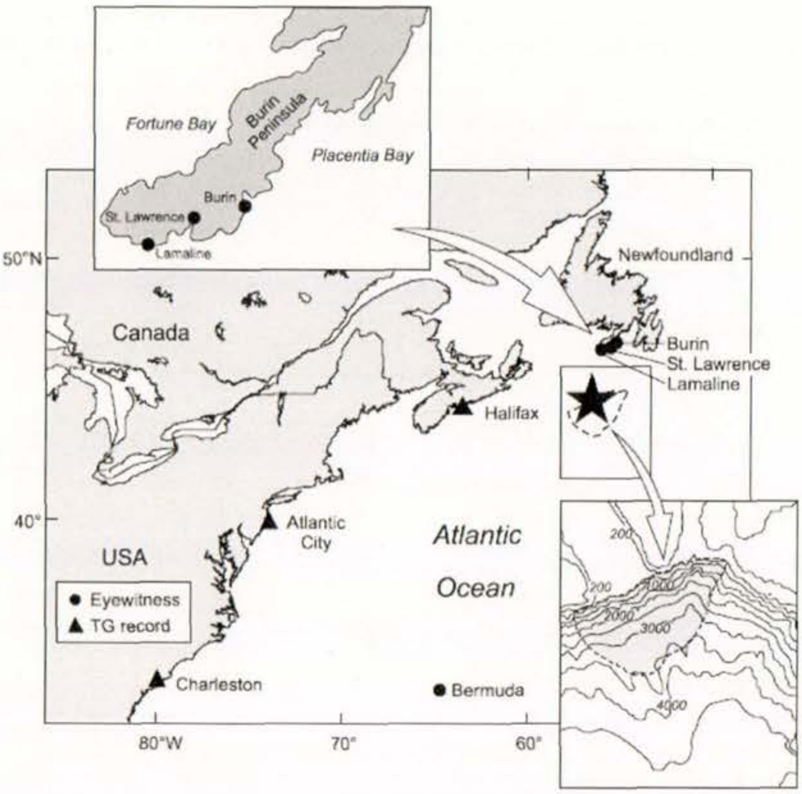

Figure 2.3. The earthquake, with the epicenter indicated by the star, initiates a landslide with an initial outline approximated by the shaded area in the lower-right inset (Fine et al. 2005).

New Zealand is not immune from submarine landslides and associated tsunami generation. The 1931 Napier earthquake caused a rotational slump in the Waikare estuary sweeping water onshore to a height of 15 m above sea level (Bryant 2001; de Lange and Moon 2004; Peacock 2002). A co-seismic tsunami was also generated, with a maximum height of 3 m to 5.5 m.

The events in March and May of 1947 off the coast of Gisborne, New Zealand, generated tsunami with maximum wave heights of 10m and 6 m respectively. These wave heights were considered too large to have been generated by the magnitude of their associated earthquakes, and appeared to be aperiodic and few in number, with successive waves arriving before the complete withdrawal of the previous wave. Also, the wave height distribution decayed more rapidly with distance from the source than was expected for an earthquake-generated tsunami. Later numerical modelling determined a submarine landslide with a thickness of 125 m, total length of 6000 m, and source area of 9 km^2 located at the head of the continental slope best replicated the observed 10 m tsunami on March 1947 (de Lange and Moon 2004; Peacock 2002).

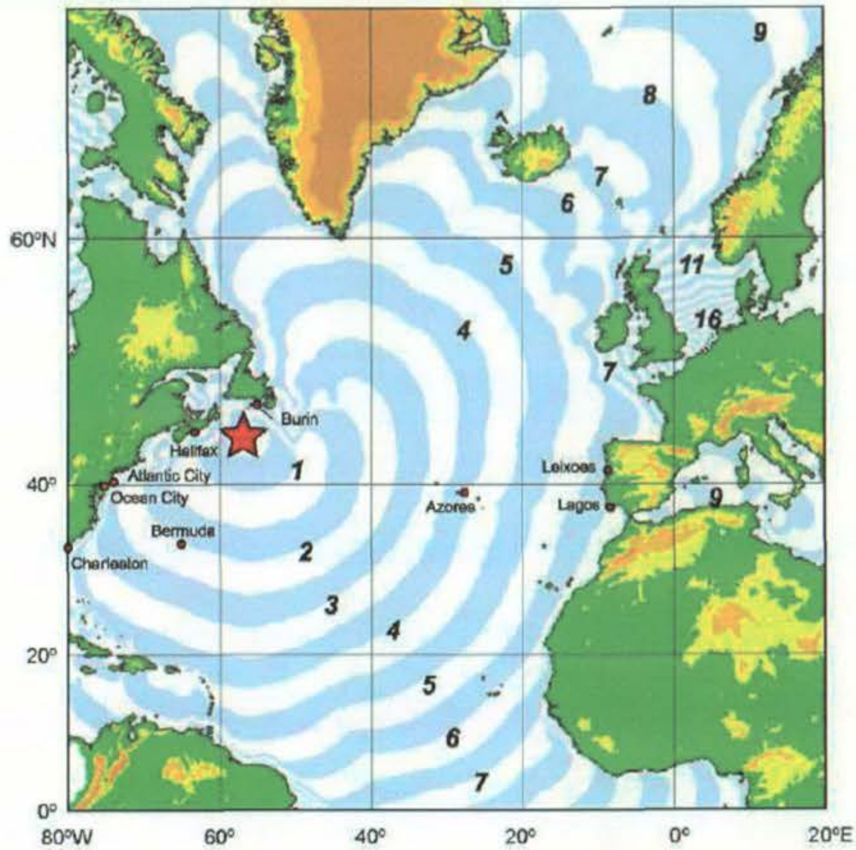

Figure 2.4. Map of estimated travel times (in hours) in the North Atlantic Ocean of the waves generated by the 1929 Grand Banks event (Fine et al. 2005).

2.3 Characteristics of Soils and Landslides

Soils are a natural substance, and as such, have a wide variety of characteristics and exhibit an equally wide range of behaviours. Some basic soil and slope mechanics are presented to detail the generation mechanism of underwater landslide-induced tsunami. How and why slopes fail is dependent on the characteristics of the soil within, and how they respond to external stimulation.

Naturally occurring soils fall into two categories, those that are formed in situ and those that have been transported to their current location. In situ soils are further divided into two categories, weathered rocks and peat. Weathered rocks consist of portions of rock fragmented by mechanical and chemical weathering, whereas peat consists of an amalgamation of organic material such as wood fibres and plant remnants. Transported soils are predominantly moved by water, wind, and ice, under the effects of gravity.

Soils are classified depending on their grain size. Based on the British Soil Classification System (BSCS) soils with grain sizes smaller than 2 μm are classed as clays, soils between 2 μm and 60 μm are silts, sands have grain sizes of between 60 μm and 2 mm, gravels between 2 mm and 60 mm, and cobbles between 60 mm and 200 mm (Barnes 2000). Soils found anywhere on the earth are made of different proportions of clays, silts, sands, gravels, and cobbles.

Soils can be further defined by particle density, shapes of the particles that compose it, distribution of particle sizes, density of the materials, cohesion, and moisture content. Even slight variations in these properties can cause soils to exhibit significantly different behaviour. A peculiar behaviour of sands and cohesionless silts is that when in the presence of water, they tend to dilate and liquify when subject to external loading.

Slope failure can be modelled by the Mohr-Coulomb failure criterion as follows (Barnes 2000; Bryant 2001):

$$\tau_s = c + (\sigma - \xi)\tan\phi \tag{2.4}$$

where τ_s = soil shear strength
c = soil cohesion
σ = normal stresses on the slope
ξ = pore water pressure
ϕ = internal friction angle

The key factor in this equation is pore water pressure. The greater the saturation of the soil, the more prone it is to failure. Changes in pore water pressure can reduce the $(\sigma - \xi)$ term to zero. This may come about in the very short term by the passage of seismic waves, in the medium term by changes in water level and air pressure associated with large atmospheric depressions, and in the very long term with changes in sea levels (Bryant 2001). With the normal stress negated by the pore water pressure, the soil strength is reliant solely on the cohesion of the soil or rock. Cohesion within the soil structure arises from the attraction between the clay and fine silt particles. Soils devoid of these, especially sands, are at greater risk of failure due to the lack of cohesion and a phenomenon known as liquefaction.

Large landslides tend to occur in materials susceptible to liquefaction (Finn 2003). When saturated pockets of loose sands and cohesionless silts encounter sufficient ground motions, they can exhibit a flowing tendency. Ground-shaking tends to compress these loose soils, but they are unable to do so due to the inability of the pore-fluid to escape from the soil void spaces in the relatively short time of shaking. Earthquake-induced liquefaction is even more likely in offshore environments as the soils are always saturated. It is interesting to note that failure is also possible some time after an event due to changes in soil strength through the redistribution of pore water (Wright and Rathje 2003).

If the driving stress is larger than the post-liquefaction strength, then a liquefaction flow failure develops resulting in large displacements. Sometimes, the liquefied soil may have enough residual strength to resist the static forces applied to it, but with the momentary addition of dynamic stresses with the passage of seismic waves may no longer have adequate strength. Limited displacement, or cyclic mobility, may then occur where movement only occurs when the combination of static and dynamic stresses momentarily exceed the soil strength.

The extent of deformation can range from minor cracking, to slumping, to full mobility where the slide material is essentially unimpeded until the retarding force on the slide finally exceeds the driving (gravitational) force (Ishihara 2002). Liquefaction of sands and cohesionless silts in a saturated state exhibit this peculiar type of behaviour clearly. Figure 2.5 illustrates the stress-strain behaviour of these soils. The external stresses imposed on the soil induce strains, and the soil deforms to a limited extent. The stresses can increase further until some value of maximum undrained strength is reached after which the structure collapses. The resistance drops to a low level that can be maintained for large values of strain, called residual strength, and is the controlling factor in determining the extent of post-liquefaction stability. If the driving gravitational shear stresses are considerably higher than the residual strength, then very large deformations and displacements can result. The initiation and continuance of liquefaction is controlled by the intensity and duration of the loading.

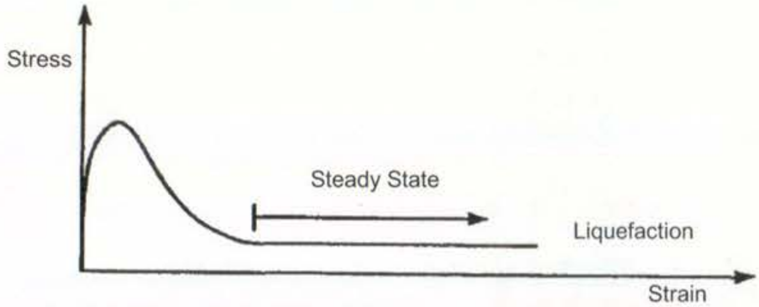

Figure 2.5. Stress-strain behaviour of soils (Finn 2003)

Triggering mechanisms of landslides vary widely. The most common cause is acceleration-induced sliding in which the inertial forces associated with earthquakes cause the driving forces to momentarily exceed the resistance of the soil, initiating movement. If the accelerations are strong, or continue for long enough, the slope may deform excessively or fail completely (Wright and Rathje 2003). Earthquakes also serve as triggers for initiating the movements that combine with other mechanisms, such as liquefaction, to cause the slope to fail.

2.4 Underwater Landslides

The marine and fresh water environments essentially experience the same mass failures as those found on land. As such, most of the submarine landslide geological theory has come from traditional terrestrial slope stability analysis. Much has been published on terrestrial landslides and is generally very well understood. Existing turbidity current mechanics comes from that of avalanches, as both are forms of gravity current, with solid particles suspended in a fluid.

2.4.1 Landslide Initiation

The advent of detailed side-scan sonar and other recent improvements in underwater survey and mapping techniques have helped to identify which tsunami were most likely created by submarine land sliding instead of earthquakes. However, earthquakes are often the mechanism for triggering the landslide initially. Other causes of underwater landslides are; storm wave loading, oversteepening, changes in sea levels, rapid accumulation and under-consolidation, gas charging, gas hydrate disassociation, low tides, seepage, glacial loading, and volcanic island processes (Locat and Lee 2002). Geological evidence of underwater slides includes headscarp features, large cracks, amphitheatre structures, and hummocky or blocky topography.

Acceleration, liquefaction, and fault rupture-induced landslides occur in both terrestrial and submarine environments. Some landslide triggering mechanisms are limited only to offshore situations, such as water wave-induced sliding. The seafloor in water depths less than 100m are at particular risk to disturbance from the large changes in stress caused by large ocean waves, such as those generated by severe low-pressure weather systems or by the passage of tsunami. The rapid draw-down of water levels at the shore as a tsunami approaches is also capable of removing the resisting force on the slope and could induce a slope failure leading to further tsunami generation mechanisms. Though widely accepted as a mechanism for potential instability in earth dams, any slope comprised of fine-grained soil that is marginally statically stable is susceptible to slope failure triggered by rapid water draw-down.

Surface fault ruptures can significantly change the surface profile of slopes, triggering sliding. Slopes that are marginally stable before the rupture can be more susceptible, and many offshore processes, such as sediment deposition on active river deltas and continental slopes, leave the soil in marginally stable states. Such landslides may only be small, affecting the local area around the rupture, but could be a prompt for a much larger slide.

A process known as under-consolidation can also increase pressures within the soil as natural gases, such as methane, are formed when organic matter in the soil decays anaerobically. Methane on the lower slopes of the deep ocean can often be locked into the sediment as a solid gas hydrate due to the extremely cold temperatures and pressures. As the hydrate decomposes back into methane, it can further increase the pressure with the release of gas, or form voids in the sediment to become planes of weakness.

2.4.2 Classification and Characteristics of Underwater Landslides

There are many types of submarine mass movements. These are summarised in Figure 2.6, and include rotational and translational slides, debris and mud flows, and turbidity currents. Each event consists of several distinct phases, starting with slide initiation, triggering mechanisms some of which were discussed earlier. Often, slides then transition into a debris flow regime, with subsequent generation of a turbidity current and its motion along the sea floor until final deposition.

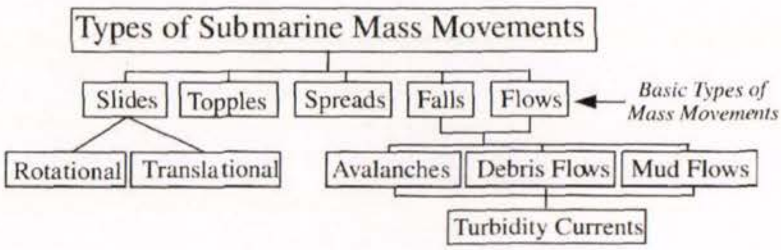

Figure 2.6. Classification of submarine mass movements (Locat and Lee 2002).

There is an extensive literature on landslide morphology and the papers of Barnes and Lewis (1991), Hampton et al (1996), Locat and Lee (2002), and Finn (2003), are typical works dealing with the theory of the interaction of soil and fluid. After the initial slope failure, some landslides can evolve from the limited displacement of slides and slumps into more mobile flow structures. This transition is not well understood but is related to the initial and final density of the slide material. Similar to snow avalanches, the flowing material separates into two layers, the suspension flow over-riding the dense flow. Dense flows can take the form of rock avalanches, debris flows, and mudflows. Suspension flows are generated by the drag forces on the upper interface of the dense flow and can become turbidity currents if they overtake the bottom denser layer. At some critical speed, thought to be approximately 5 m/s, hydroplaning can cause the nose of the dense flow to lift, reducing the shearing resistance along the sliding surface, and adding mobility to the flow. A continual regime of erosion and sedimentation will occur at the interface of the dense flow and the rigid base. These processes can occur on slopes as small as fractions of a degree, and are illustrated in Figure 2.7.

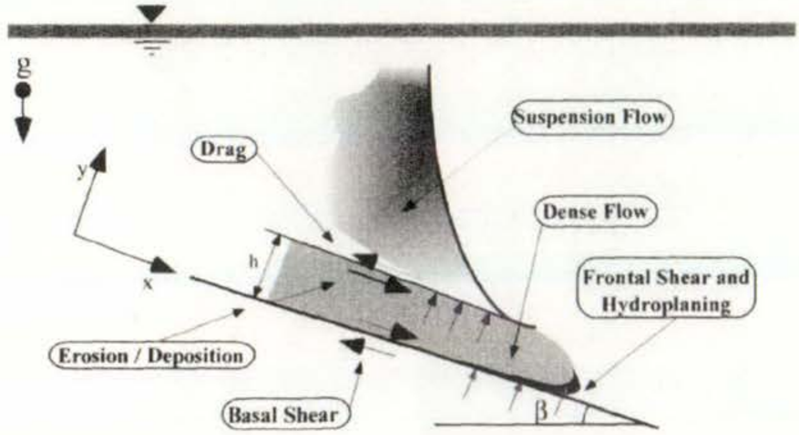

Figure 2.7. Schematic view showing the different flow structures for a hydroplaning dense flow (Locat and Lee 2002).

Submarine landslides are often found to occur on slopes less than 10 degrees (McAdoo et al. 2000). This indicates that although the vertical component of the landslide motion may be small, it is enough to create the initial disturbance of the water surface, causing a large wave to develop with the continuing motion of the failure mass. Landslides have a wide range of run-out distances, from short rockfalls and rotational slumps, to long run-out associated with debris flows and turbidity currents. The steepness of the slope adjacent to the failure has been found to be inversely proportional to the length of landslide run-out, indicating failures on steep slopes tend to have less run-out than failures on shallow slopes. Such long run-out lengths along shallow slopes, sometimes of the order of hundreds of kilometres, is only beginning to be understood but the main reason is thought to be hydroplaning of the failed mass (Locat and Lee 2002). Run-out length may well be influential in tsunami generation, but is currently not well researched.

Observations and computer modelling of both sub-aerial and submarine landslides show they tend, in plan, to have elliptical shapes, width-to-length ratios of 0.5-1 (Martel 2004), and mean thickness to length ratios of approximately 0.01 (Watts and Grilli 2003). Slide material from a rotational slump generally does not move far from its original position, whereas sheet slides can transport slide blocks considerable distances. This sustained movement of a sheet slide allows the material to disintegrate into a debris avalanche and possibly into a turbidity current if the landslide occurs in water.

2.4.3 Historical Underwater Landslides

One of the largest known submarine landslides occurred 200,000 years ago on the northern flanks of the island of Oahu, Hawaii (Bryant 2001). Known as the Nuuanu landslide, it involved the mobilisation of 5000 billion m^3 of material across a slide scar of 23,000 km^2. This slide ran down 220 km into the 4,600 m deep Hawaii Trough and back up the other side of the underwater canyon to a final water depth of less than 4,300 m. Calculations using the analogy of a frictionless roller coaster, the speed of the slide must have been approximately 80 m/s to be able to run up a height of 350 m (Ward 2001). 140 km offshore of Oahu is the Tuscaloosa Seamount, which with a size of 30 km in length, 17 km in width, and with a 1.8 km thickness, is actually a detached block from the Nuuanu debris avalanche (Hampton et al. 1996). A side-scan sonar mosaic of the Nuuanu landslide is shown in Figure 2.8. Numerical models of this landslide predict waves of up to 60 m in height striking the beaches of the Hawaiian Islands, and waves of 20 m along the North-west Pacific coastline.

Figure 2.8. Side-scan sonar image of the Nuuanu (off Ohau) and Wailau (off Molokai) debris avalanches, Hawaii. Individual displaced blocks, the largest being the Tuscaloosa Seamount, appear as distinct light areas, generally becoming smaller away from the islands (Hampton et al. 1996).

Three massive submarine landslides, with a combined volume of 5580 billion m^3, occurred off the west coast of Norway. The largest of these slides occurred 30,000 years ago at Storegga involving 3880 billion m^3 running 500 km down the continental slope from a water depth of 500 m to over 3000 m (Hampton et al. 1996; Ward 2001). Computations indicate 12 m and 6 m high wave run-ups would have reached Norway and Iceland within two hours of the start of the event respectively. A set of waves up to 15 m in height spread out across the Atlantic Ocean.

2.5 Previous Laboratory Underwater Landslide Experiments

Experimental research into submarine landslide-induced tsunami began in 1955 to dispel the belief of many at the time that disturbances such as submarine landslides were unlikely to cause tsunami. As discussed in previous sections, the type of submarine mass failure is based on the landslide geometry and on the characteristics of the failure material, such as chemical composition, grain size, and density. Due to the inherent difficulties with scaling of these factors, the landslide failure mass is often approximated experimentally by a solid mass, either triangular or semi-elliptical in shape.

For this reason, Wiegel (1955) preferred to experiment with sliding and falling blocks of various shapes, sizes, and densities, as opposed to granular slide experiments. These two-dimensional tests were performed in a constant depth channel, and factors such as initial submergence, slide angle, and water depth were varied, and the wave characteristics were measured using parallel-wire resistance wave gauges at both near and far field locations.

Surface time histories of the tests downstream of the disturbance showed a crest formed first, followed by a trough with amplitude one to three times that of the first crest, and followed by a crest with a similar magnitude to the trough. It was found that dispersive waves were generated, as crests and troughs continued to be generated with increasing distance, and the amplitudes of the waves diminished as they propagated. The magnitude of the wave heights were found to depend primarily on the block weight, initial submergence, and water depth. The period of the waves was found to increase with increasing block length and decreases in incline angle. A dimensional analysis concluded that no parameters could be neglected. Instead, certain parameters were found to be related in such a way that it was not possible to hold all but one constant to determine their individual effects. Computations indicated approximately 1% of the initial net submerged potential energy of the sliding block was transferred into wave energy, with this percentage increasing with reduced initial submergence and decreasing water depth.

Other experimentalists have chosen to simulate a submarine landslide with a right-triangular prism sliding down a 45° slope (Rzadkiewicz et al. 1997; Watts 1997; Watts 1998; Watts 2000; Watts and Grilli 2003). The two-dimensional experiments of Rzadkiewicz et al. (1997) were a short series of tests to produce data to compare directly with some of their numerical models. These tests involved right-triangular simulated landslide masses, consisting of solid material, and granular sand and gravel, sliding down 30° and 45° slopes. Side-on images were captured at 0.4 s and 0.8 s after slide release, and from these landslide material shape and water level profiles were determined.

Watts' (1997) experiments were similar, consisting of solid and granular slides along a 45° slope, as illustrated in Figure 2.9. However, a wider parameter space was investigated, with slide material, initial submergence, porosity, and density varied. Resistance wave gauges were used to measure water level time-histories at various locations downstream of the slide, and a micro-accelerometer recorded the landslide's centre-of-mass motion. Examples of the near and far field waves measured are plotted in Figure 2.10. A comparison of the motions of granular slide material with the motions of a solid block, by using a variety of granular materials to simulate the landslide failure mass, found that the centre of mass motion of a granular slide was similar to that of a solid block slider. This study also tried to develop a non-dimensional framework in which to predict maximum wave amplitudes (wave troughs) from specific landslide parameters such as landslide length and initial submergence.

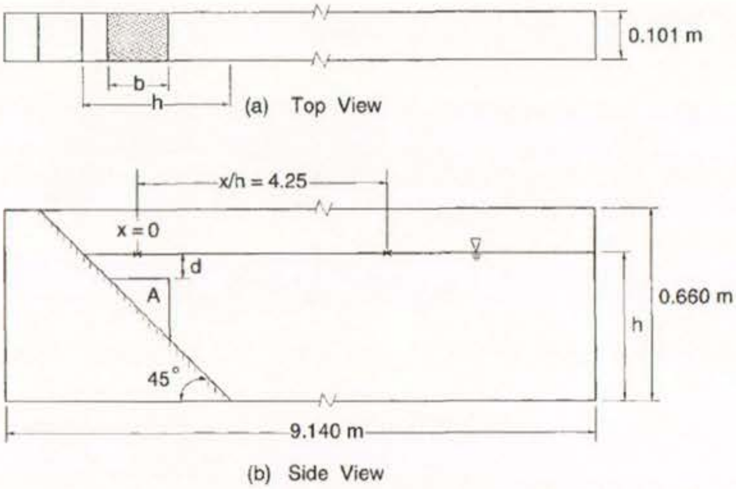

Figure 2.9. Diagram showing the test arrangement of Watts' (2000) 2-dimensional laboratory experiments with sliding triangular solid blocks. The positions of the resistance wave gauges used are shown at the top of the side view.

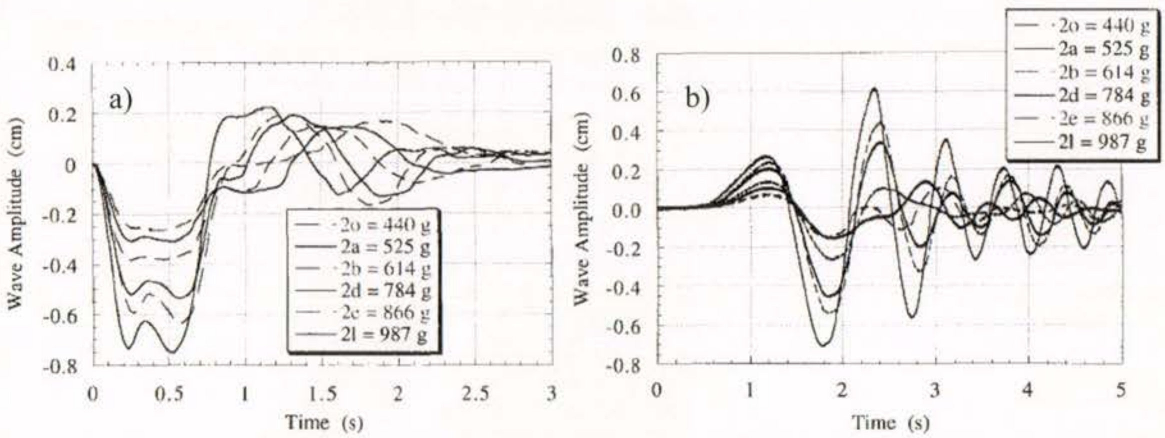

Figure 2.10. Water level time histories, from Watts' (2000) experimental tests, measured at the a) near field wave gauge, and b) far field wave gauge for six block densities. The initial submergence of these blocks was 74 mm.

Much of the latest experimental research appears to be in three-dimensional wave experiments with both angular, semi-hemispherical (Liu et al. 2005; Raichlen and Synolakis 2003), and streamlined solid block slider shapes (Enet et al. 2003). The large-scale tests of Raichlen and Synolakis (2003), attempting to minimise the effects of viscosity and capillary action, consisted of a 91 cm long, 46 cm high, and 61 cm wide triangular wedge-shaped block sliding down a planar (1 V:2 H) slope, as shown in the photographs in Figure 2.11. The 475.52 kg block started its slide at various submergences from fully submerged to partially aerial. A micro-accelerometer and position indicator recorded the block location time-histories, and an array of resistance wave gauges recorded the propagating waves and run-up heights on the beach behind the sliding mass. Examples of the measured wave run-up and water level time histories are plotted in Figure 2.12.

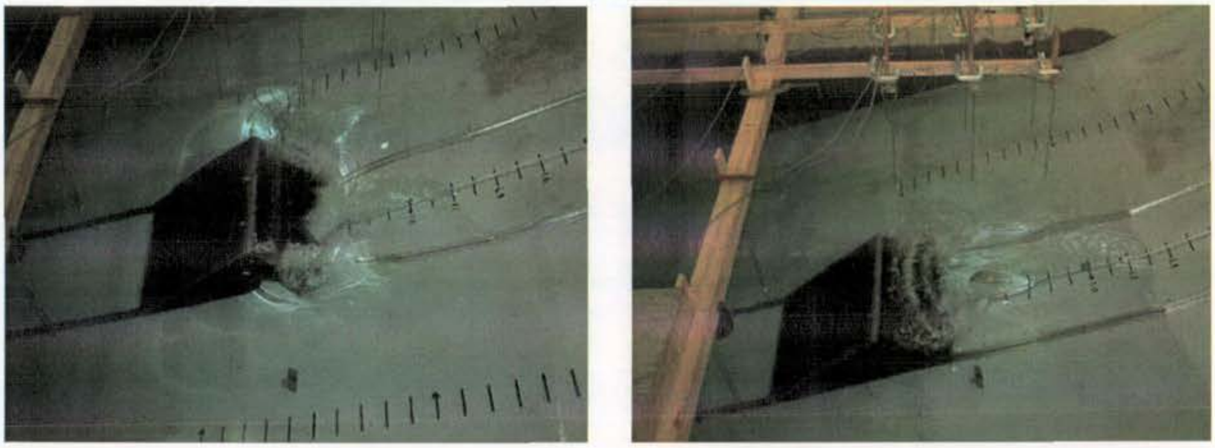

Figure 2.11. Photographs from Raichlen and Synolakis' (2003) 3-dimensional tests. The photo on the left shows the draw-down of the shore as the block begins to slide. The photo on the right shows the same wedge moments later when the wave runs back up the shore. The array of resistance wave gauges used to measure wave heights can be seen hanging above the block.

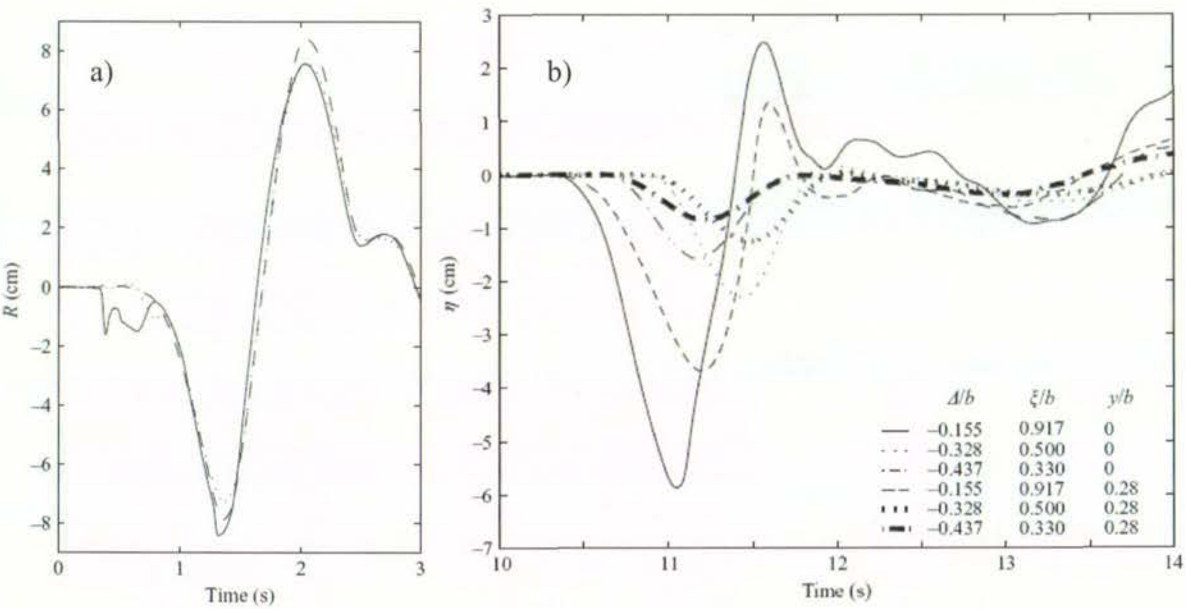

Figure 2.12. Some typical a) run-up time histories and b) water level time histories at different locations for three initial submergences, from Raichlen and Synolakis' (2003) 3-dimensional tests (Liu et al. 2005).

The three-dimensional simulated submarine landslide tests of Enet et al. (2003) were developed to produce experimental data suitable for comparison with their numerical model results. The flattened dome-like slider block had a thickness of 80 mm, a length of 400 mm, a width of 700 mm, and a bulk density of 2,700 kg/m^3. The initial submergence was varied and its motions as it slid down the 15° slope were recorded with a micro-accelerometer located at the block's centre-of-mass. The propagating wave field generated was measured with an array of four capacitance wave gauges. Photographs of the sliding block and wave gauge array are shown in Figure 2.13.

Figure 2.13. Photographs from the 3-dimensional tests of Enet et al (2003). The photo on the left shows the flattened dome-like model landslide mounted to a guiding rail. The photo on the right shows the array of capacitance wave gauges, used to measure wave heights, placed over the wave tank.

In an effort to produce comparable results from their numerical models, the international tsunami research community defined a benchmark configuration for studying the generation of tsunami by underwater landslides. This was deemed necessary due to the difficulties in interpreting the results from the various experimental and numerical models incorporating a wide range of constitutive behaviours (Grilli et al. 2003; Watts et al. 2001). It was also noted that the sharp edges of the triangular sliding blocks used in previous experimental studies were difficult to model computationally due to the strong flow separation at the vertices. Apart from reef platform failures, this shape was considered to be unrepresentative of the geometry of most underwater mass failures. The tsunami community's recommendation was for a smoother, more streamlined shape which, despite its idealisation, would represent the majority of real events (Grilli et al. 2003).

Two-dimensional tests were recommended as they presented fewer difficulties than three-dimensional tests for numerical modelling. The benchmark configuration consisted of a semi-elliptical block sliding down a planar slope at 15 degrees from the horizontal. The landslide had a thickness:length ratio of 1:20 and a specific gravity of 1.85. It was completely submerged, with the centre of the top surface initially submerged 0.259 times the length of the landslide. A basic set of experiments of this arrangement was performed, but the quality of the results were inadequate to validate numerical models due to electrical point wave gauge accuracy (Watts et al. 2001). A photograph of the landslide block is shown in Figure 2.14 and some water level data is included in Figure 2.15.

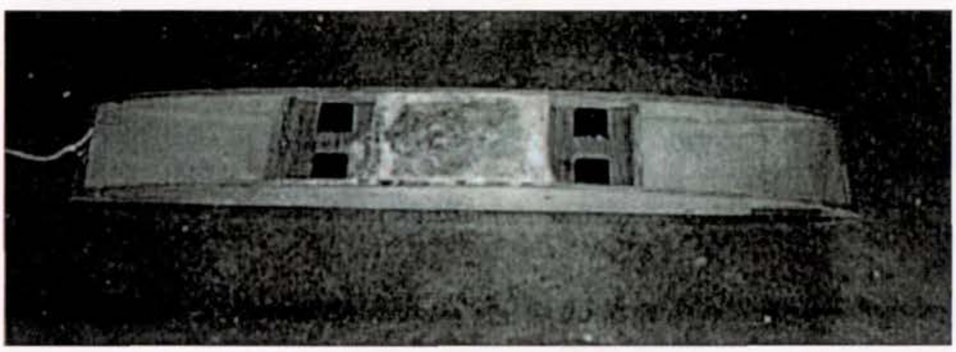

Figure 2.14. The plywood construction of the semi-elliptical model landslide used in the benchmark configuration experiments (Grilli and Watts 2005; Watts et al. 2001). It is 1.0 m long, 0.2 m wide, and has a thickness of 0.052 m.

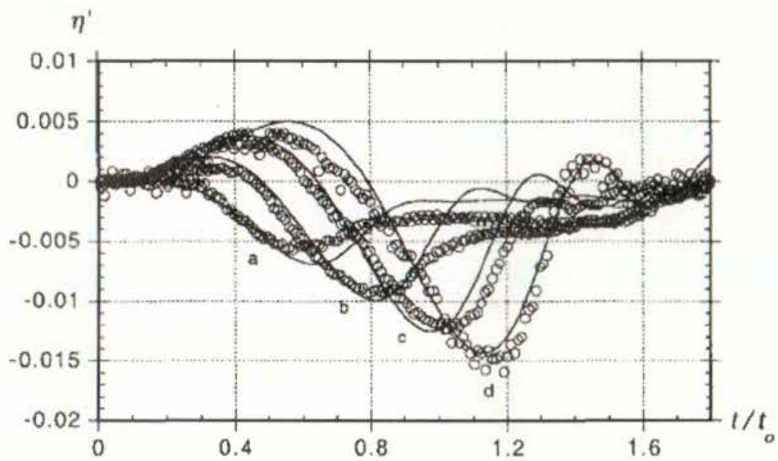

Figure 2.15. Non-dimensionalised water level time histories at four wave gauge locations for the semi-elliptical benchmark experiment (Grilli and Watts 2005). The measured values, represented by circles, are compared with numerical results, shown as solid lines.

The work of Fleming et al (2005) also experimented with this benchmark configuration. Sets of experiments were performed with a semi-elliptical block and water levels were recorded with three resistance wave gauges. The data generated was to be compared with the results of Watts et al (2001). Further experiments with triangular solid and granular slides were completed to examine the effects of initial landslide shape, initial submergence, volume, density, and deformability. Water levels in the near- and far-field were measured with an array of five wave gauges.

The experiments of Fleming et al (2005) were completed at the University of Canterbury, immediately prior to the beginning of this current research, and provided an opportunity to trial and assess the suitability of the techniques used herein. A new optical wave measurement technique utilising Laser Induced Fluorescence (LIF) was used to measure the wave shape in the near-field as well as wave run-up. The sub-surface water velocities and internal strain rates and velocities of the granular sediment were quantified using Particle Tracking Velocimetry (PTV). Further details of these techniques are given in Chapter 3.

2.6 Numerical Modelling

A variety of computational models have been developed by researchers to look at the many different phenomena associated with submarine landslides and tsunami. Each model makes certain assumptions in order to simplify the governing equations of fluid dynamics. These assumptions are associated with fluid viscosity and compressibility, landslide friction, and wave linearity. There are models for slope failure (Martel 2004), landslide and water interaction (Jiang and Leblond 1992), wave generation and propagation (Enet et al. 2003; Grilli et al. 2002), and wave run-up (Kanoglu 2003; Kennedy et al. 2000; Liu et al. 2005; Synolakis 1987; Tarman and Kanoglu 2003; Walters 2003). Most models use a finite or boundary element approach (Grilli et al. 2002; Mariotti and Heinrich 1999; Rzadkiewicz et al. 1997).

The more complex models are able to predict fluid parameters such as water level, wave run-up, and sub-surface velocities and pressures, varying in three spatial dimensions and over time.

There are also several simple methods for predicting gross wave properties, such as maximum expected wave heights. Murty (2003) used information available in the literature to find a simple empirical linear relationship between landslide volume and the maximum observed wave heights.

Another simplified model, used to couple the landslide mass to the generated waves, was to determine the amount of energy transferred from the block's initial gravitational potential energy to the potential energy of the waves. This is found to be of the order of 1% - 2% (Jiang and Leblond 1992; Ruff 2003; Tinti and Bortolucci 2000; Watts 1997).

Wave run-up at planar beaches has been studied in significant detail in the past (Kanoglu 2003; Kennedy et al. 2000; Liu et al. 2005; Synolakis 1987; Tarman and Kanoglu 2003; Walters 2003). These models studied run-up from waves generated from distant sources and looked at their transformation, breaking, and run-up as they approached the shore. In an underwater landslide, the failure mass motion will be away from shore, generating waves that also move offshore. However, little work has looked at the wave run-up at the beach behind the landslide, as it is this that is of immediate danger to the population and infrastructure in the slide proximity.

Numerical models are often used to 'back-predict' the tsunami waves from given geological evidence of a landslide, or to determine the extent of the submarine failure from the observed wave run-up height distributions (Day et al. 2005; Fine et al. 2005; Lynett et al. 2003; Tinti et al. 2006; Tinti et al. 2000; Ward 2001).

Individual models are tested using different geometries and motions, which make comparisons between models difficult (Grilli et al. 2002; Grilli and Watts 1999; Mariotti and Heinrich 1999; Rzadkiewicz et al. 1997). Also, many of these models have been developed in isolation from submarine landslide geomorphology, and are therefore difficult to apply to real situations. Even when there are large amounts of field data available to validate these models, such as from the 1998 Papua New Guinea event, there are difficulties and controversies plaguing their interpretation (Davies et al. 2003; Imamura and Hashi 2003; Lynett et al. 2003; Okal 2003; Satake and Tanioka 2003; Tappin et al. 2003; Tappin et al. 2001). Experimental tests are a means to validate these numerical models. To some extent validated models possess some predictive qualities.

Experimental laboratory test results are generated using grossly simplified geometries and are inherently difficult to scale up to full-size. To model each tsunami scenario in the laboratory at sufficient scale and complexity to account for landslide deformations and ocean bathymetry would prove to be extremely costly. As such, laboratory experiments are used to observe specific features of tsunami generated by sliding masses in a controlled manner, and numerical models take into account the various shoreline and deep-ocean geometries when used to predict full-sized events.

2.7 Literature Review Summary

In this chapter a review of the English language literature illustrated the chronological and global extent of tsunami events. In particular, the potential for future damage from underwater landslides was presented. Details of the characteristics of soils were given along with how these soils behave under external loading. Particular attention was given to the liquefaction of saturated sands and cohesionless silts, especially in marine environments where these soils are abundant. The sections on initiation and morphology of underwater landslides highlighted the variety of forms an underwater landslide can take. Details and some examples of results were presented for previous laboratory underwater landslide experiments. Numerical models with a range of complexities have been developed to model these events. Experimental results, such as those presented in this report, are a means to validate these computational models.

The research to be described here follows on from the experimental work of Fleming et al (2005) and Watts et al (2001). The work of these earlier experimentalists with the benchmark landslide configuration is extended to look at a range of combinations of landslide density and initial submergence. Also, the entire water surface profile time histories will be measured using the LIF technique, instead of quantifying the water levels at discrete locations. Similar to the work of Fleming et al (2005), PTV will be used to measure the landslide and sub-surface water velocities. However this research will use this data to determine the relationship between these parameters and the observed wave fields.

Chapter 3: Methods

The motivation behind this experimental program was to generate a comprehensive dataset using the benchmark configuration defined by the international tsunami research community (Grilli et al. 2003; Watts et al. 2001). The data from this study of tsunami generation by underwater landslides would be of sufficient quality for comparisons with numerical models.

The same two-dimensional configuration as Watts et al (2001) was used. This consisted of a model landslide with a thickness:length ratio of 1:20. However, unlike their experiments, a variety of landslide densities and initial submergences were investigated here.

The use of electrical point wave gauges at specific locations can only give limited insights into the wave generation process, as the spatial changes in water profile between the gauge positions are not measured. There are also questions as to the influence of surface tension and meniscus effects on the gauge wires at the small laboratory scales, as well as the effect of having objects physically in the flow. To remedy this, a non-intrusive water level measurement technique was developed that minimised the disturbance to the water, and also captured the spatial as well as the temporal variations. This technique utilised Laser Induced Fluorescence (LIF) to measure the necessary wave parameters. A dye was added to the flume water that fluoresced under the influence of laser light. Digital video imaging recorded the position of the interface between the fluorescing water and the black backdrop of the surrounding darkened room.

To understand the physics behind the wave generation processes, the waves measured using LIF needed to be related back to the generation mechanism, the landslide motions. Particle Tracking Velocimetry (PTV) was used to track the location time history of the landslide's centre-of-mass. Single and double differentiation of the centre of mass position with respect to time yielded the velocity and acceleration time histories.

PTV was also used to observe the sub-surface water motions. Fine near-neutrally buoyant particles were dispersed throughout the fluid and illuminated using a white light sheet. The position time histories of the illuminated particles were recorded using digital cameras. Post-processing of these particle positions matched their locations from one frame to the next to generate particle tracks and fluid body velocity fields.

The following sections describe the experimental flume set-up and give details of the model landslide block. The chapter continues with information on the PTV technique used to measure the landslide kinematics. The development of the LIF technique, to measure the water levels, is also presented, along with details of its capabilities compared with traditional electrical wave gauges. The chapter closes with a description of the sub-surface velocity measurements.

3.1 Experimental set-up

3.1.1 Flume

The wave tank used in these experiments was a 14.66 m long flume in the University of Canterbury's Fluid Mechanics Laboratory. The base and ends were made of 17 mm thick transparent acrylic sheeting and the sides were of 20mm thick sheets to form a 250 mm wide by 505 mm deep usable section. This flume was designed with minimal reinforcement between adjacent side panels to reduce the interference of the joints during optical data capture. Silicon-based sealant was used in these joints to prevent leakage. 3 mm diameter threaded steel rod ties across the top of the flume were spaced a 0.8 m intervals to prevent the tops of the flume sidewalls from bowing due to the considerable hydrostatic water pressures. One day before the test, the wave tank was filled with tap water to a depth of 435 mm, leaving 70 mm of freeboard. It was then allowed to degas, and any air bubbles that formed were removed before the tests.

This flume was housed in a 3.7 m wide, 18.9 m long, and 2.4 m high, room. All windows and other openings were blacked out to reduce outside light interference and to contain the laser light when it was operating in the darkened room. The base of the flume was 1.1 m above the floor on a steel square hollow section truss frame and was located 1.4 m out from one of the sidewalls. A workbench extended the full length of the opposite side, leaving a space of 1.3 m between it and the flume.

Gantry rails parallel with the flume supported an overhead trolley. The trolley could be moved to any position along the length of the flume room by a variable speed electric motor, and was used to support the various testing equipment.

3.1.2 Landslide Slope

An inclined ramp at an angle of 15 degrees to the horizontal made of 12 mm thick acrylic was placed at one end of the flume. It was held in place by normal forces applied by the sidewalls, and supported by five pairs of vertical struts under the slope placed at regular spacing along the ramp's length. This planar slope extended out above the flume for a height of 0.135 m. This provided space well out of the water to place the equipment for holding and releasing the landslide. The ramp sloped continuously into the flume until it was 0.089 m from the flume floor.

A 2 mm deep step, 50 mm wide, was milled into the two edges of the top surface. This was to hold in place 50 mm wide strips of 0.8 mm thick stainless steel and 1.2 mm thick PVC plastic. The stainless steel strips were used to provide a means for the surface of the slope to transition from the 15 degree slope to the horizontal floor of the flume, and allow the landslide to slide smoothly down the slope and then along the floor where it would eventually stop due to friction. The PVC strips were used to provide a more slippery surface upon which the landslide would slide compared to the acrylic base material, and could be easily replaced when worn. The strips were held in place by small stainless steel screws mounted below the slope surface in counter-sunk holes, spaced 0.100 m apart. For the lower 0.089 m of height from the end of the planar slope to the floor of the flume, the mildly flexible stainless steel strips formed a catenary curve under its own weight. The equation of this curve was determined and profiles of this were cut from sheets of acrylic and fixed underneath the stainless steel strips to provide rigid support beneath.

The strips were used, instead of solid sheets extending across the entire width of the flume, so that the centre portion of the ramp was still transparent to allow light through for the PTV measurement of sub-surface water velocities.

Lubricant was applied on the slope surface to minimise any tendency for the model landslide to stick. After testing various lubricants, such as light oils and PTFE-based coatings, silicone grease was found to be most resistant to wearing, moisture, and time degradation, and had the advantage of being able to be applied under water.

3.1.3 Model Underwater Landslide and Release Mechanism

The prismatic semi-elliptical model landslide was milled from a solid block of aluminium. The block was 0.5 m long (major axis length) and 0.026 m thick (minor axis = 0.052 m), and 0.25 m wide. The total volume of the block was 2.419 litres. Hollow cavities were incorporated into the base of the block that could be filled with polystyrene or lead shot ballast to vary the total specific gravity of the landslide. A plastic sheet was screwed into place to cover the cavities and secure the ballast. To minimise the reflectivity, the landslide block was painted matt black. Photographs of the aluminium slider block are included in Figure 3.1.

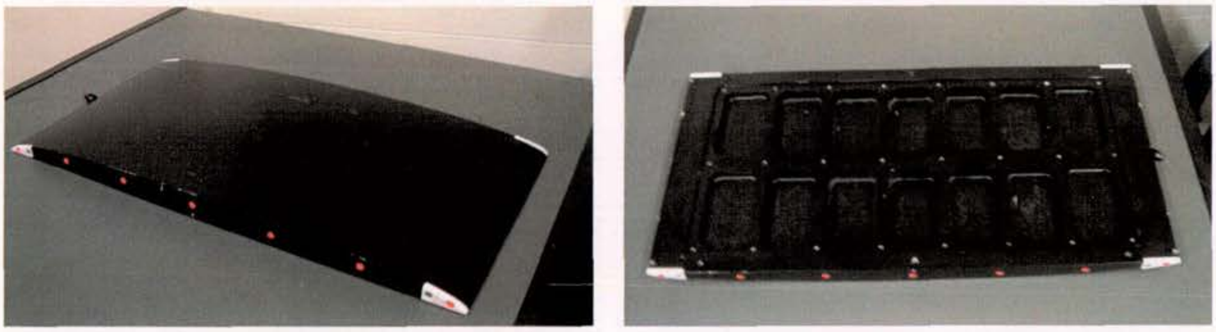

Figure 3.1. Photographs of the upper and lower faces of the aluminium sliding block.

Notches were milled into the four corners of the landslide, as shown by the white pieces in Figure 3.1. Screwed into these recesses were sections of polytetrafluoroethylene (PTFE), which had a very low friction coefficient. These were used to minimise the friction should the block touch the sidewalls, and also served to protect the soft acrylic sidewalls from the sharp leading edge of the block.

Small holes were drilled 1 mm into the surface of the base of the block, at the four corners along the leading and trailing edges. Into these were glued 3 mm diameter hardened steel balls. These spheres protruded 2 mm from the base of the slider block and formed the four small sliding surfaces upon which the block would slide along the PVC strips on the slope surface. To further reduce the sliding friction, silicon grease was applied to the slope surface to lubricate the steel balls.

Model landslide prototypes made from wood and aluminium sheeting were tested before the aluminium block was constructed. Some preliminary tests with these prototypes were performed to assess the repeatability of the experimental set-up and measurement and analysis techniques. Analysis of the wave fields and landslide motions indicated that the original wooden blocks were not sliding consistently. On a few occasions the blocks did not begin sliding immediately after they were released, staying stationary for a moment while it overcame the static friction. To address the issues of repeatability, modifications were made to the sliding blocks and slope surface.

As the original slider blocks were constructed primarily of wood, they were susceptible to shrinkage, swelling, and warping when subjected to repeated wetting and drying cycles. The distorted shape of the blocks prevented them from sliding smoothly and reliably when released, and as such, caused obvious inconsistencies in the wave fields. It was decided to construct the landslide block, the one used in the final experiments, from a rigid piece of aluminium. Aluminium was chosen, as it was dimensionally stable and would not corrode in water. It also had a low density to allow a range of lighter landslide densities to be tested. Heavier densities could be achieved by adding lead ballast.

Excessive wearing of the base of the prototype model landslides and the slope surface also contributed to the variations in the sliding characteristics between successive runs. As a consequence, the original PTFE hemispheres glued to the base of the blocks were replaced with hardened steel.

A small metal loop was attached to the trailing edge of the block to allow a length of fishing line to be tied to the block. The trailing end of the fishing line had a loop tied into it. This fishing line was used to anchor the block to the release mechanism and hold it at the correct initial submergence prior to each experimental run. Different submergences were achieved by using different lengths of fishing line.

The release mechanism consisted of a block fixed to the upper section of the slope, well clear of the water. A hole was drilled horizontally through this block and a long metal pin was slid completely through this hole such that the tip of the pin stood proud of the block's surface. The loop on the end of the fishing line was passed through this extended part of the pin. The landslide was released by pulling the pin so the portion that was protruding withdrew into the release mechanism. With nothing to hold the fishing line, the landslide was free to move.

A light emitting diode (LED) was placed in the field of view of the camera as a means of timing the release. The tip of the release pin pressed on a switch when inserted fully into the release block and was holding the fishing line. This closed reed switch caused the LED to illuminate. When the pin was pulled to release the block, the switch was opened and the LED turned off. The first frame in the recorded image sequences in which the LED was not illuminated was considered the start of the slide (time = zero).

Initial investigations showed that the wave field generated was highly dependent on the stopping mechanism, and previous experimentalists have failed to note what technique they used to stop their sliding blocks when they reached the bottom of the slope. It is assumed that the blocks just topple over and stop when they reach the end of the slope, and their wave records end before this time. For heavier blocks with high accelerations and velocities, these times can be quite short. This does not allow sufficient time to observe the waves as they develop and propagate.

To see the effect abruptly stopping the block at the toe of the slope had on the wave field, a tether was attached to the landslide that was just long enough for the block to slide normally from its initial position until the end of the slope. It was found that a block coming to a sudden stop created waves larger than the waves that were generated by the landslide if it were sliding and decelerating naturally. It was considered desirable that the landslide be allowed to progressively transition from sliding down the slope to run out on the flume floor of its own accord. This minimised the waves being generated by the sudden stopping of the block, and was considered to more closely represent the deposition of actual underwater landslide masses sliding along shallow slopes.

3.2 Measuring Landslide Kinematics with Particle Tracking Velocimetry

Particle Tracking Velocimetry is a technique that determines the motions of particles by tracking their positions from frame-to-frame in an image sequence. In this experimental program, PTV was used in two different settings. The first was to measure the motions of the landslide block as it slid down the slope. The second application was to measure the sub-surface water velocities in particular areas.

PTV, and the related Particle Image Velocimetry (PIV), are two relatively recent visualisation methods, coming about with the introduction of digital video cameras and high performance personal computers.

PTV requires specialised software to distinguish the particles within an image, and to track them from one frame to the next. The PTV software used in this experimental program was FluidStream, developed at the University of Canterbury for flow visualisation. A more in-depth introduction to PTV and the FluidStream software can be found in the program design manual (Nokes 2005a) and the user's guide (Nokes 2005b).

To measure the landslide kinematics using PTV, a series of red dots were applied to the side of the black coloured model landslide. A colour digital video camera recorded the block's motion against a white background. Image processing then identified the red dots within each frame. The FluidStream software was then used to determine the dots' position, velocity, and acceleration time-histories.

Before and after each set of wave field measurements, the landslide motions were recorded using this technique. These tests were done to test for any changes to the slider motions that could have arisen during the four hours of water level measurements. Several repeats were done for each PTV set to check the repeatability of the process.

The effect of residual sub-surface water velocities from previous tests could also affect the motion of the landslide down the slope. Therefore, the time between consecutive runs was also investigated. Tests were performed, in which the interval between runs was progressively increased, and slider motions were recorded and compared. A time between runs of greater than two minutes was found to be adequate to allow the sub-surface motions generated by the previous test to dissipate sufficiently so as to not affect the sliding of the block during the following run.

3.2.1 Equipment and Set-up

White plastic sheeting was placed behind the flume to provide a white background. Fluorescent tube lights in the room were used to illuminate the landslide. To supplement the fluorescent lights, a halogen spotlight was mounted to the overhead gantry trolley just below ceiling level and the direction of it was adjusted to prevent reflections off the flume sidewall from reaching the camera.

3.2.2 Image Capturing Equipment and Set-up

A Canon MV30i colour digital video camera was used to capture the image sequences. This camera had a resolution of 720 horizontal by 576 vertical pixels, and a frame rate of 25 Hz. To reduce blurring of the images, the camera was set to record sequences in progressive scan mode at a shutter speed of 1/500th second. The white balance and focus were manually adjusted.

The camera was connected to a PC via an IEEE 1394 'Firewire' cable and controlled directly from the computer using Adobe Premiere software. This software also captured the image sequences before saving them as an AVI video file.

Due to the limited field of view of the camera and the restricted space beside the flume, the camera had to be moved to several downstream positions to record the entire track of the landslide motion. To aid the movement of the camera to the various locations, it was mounted on the trolley, at a distance of 1.0 m from the flume sidewall and 0.23 m above the floor of the flume. With the camera in this orientation, the resolution at the face of the landslide closest to the camera was 1.32 mm per pixel in the horizontal direction and 0.90 mm per pixel in the vertical.

To signal the start of the landslide test, the release mechanism LED was placed in the field of view of the camera.

3.2.3 Image Analysis

To isolate the red dots from the black and white background of the white plastic sheeting and the black landslide, the image processing software, ImageStream (Nokes 2005c), was used. The images were passed through an excess red filter in which the average intensity of the blue and green components at each pixel was subtracted from the red intensity. The remaining red intensity became the red intensity of the filtered image and blue and green intensities were set to zero. An example of this process is shown in Figure 3.2 for a single frame in which everything apart from the red dots on the side of the sliding block have been removed. The filtered images were then input into FluidStream. The PTV software recognised the red dot at the landslide centre of mass and tracked it through the image sequences.

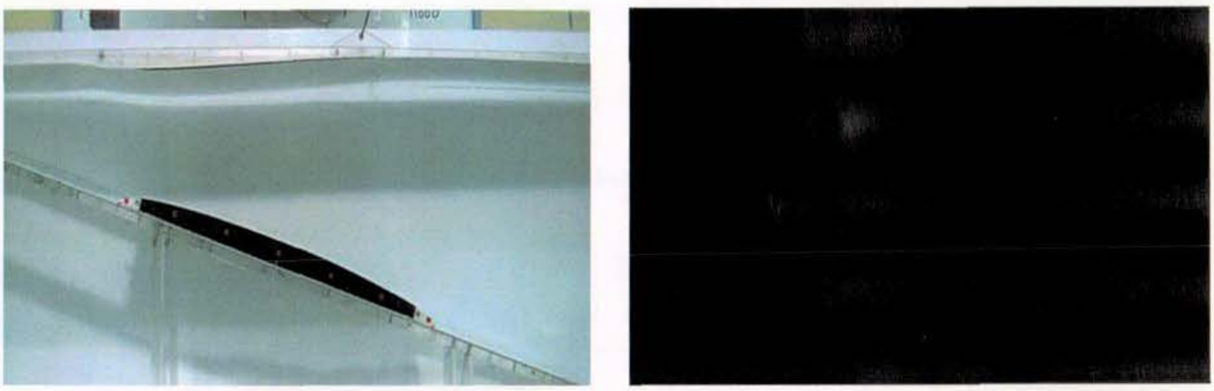

Figure 3.2. The original image (left) and its processed image (right) to remove all but the red dots on the side of the sliding block prior to the PTV analysis to find the landslide's kinematics.

The centre of mass position time-history was then corrected for camera lens-induced distortion. The use of the digital camera with a wide viewing angle allowed the greatest field of view to be recorded from a single camera location. However, it also introduced noticeable distortion to the recorded images. This distortion is called 'barrel distortion' and has the effect of bowing vertical and horizontal lines away from the centre of the image.

To correct this distortion, images of a rectangular grid were recorded using identical camera settings as the test sequences. An uncorrected (or distorted) image was adjusted using processing software that reduced the bowing of the grid lines, and this transformation was then applied to the actual test sequence. This distortion correction was used in all the optical measurement techniques that were found to have significant camera lens-induced distortion.

Applying the barrelling correction to the PTV technique to track the landslide provides more accurate results for the slide kinematics. Figure 3.3 illustrates how the distortion correction was utilized in this manner. The sliding block was moved horizontally and its motion was recorded with a digital video camera. Processing this image sequence with the PTV method outlined previously, without compensating for the lens-induced distortion, resulted in the blue line in Figure 3.3. This shows how the block appears to drop in elevation by approximately 8mm and then rise back to its original height, even though its true motion was practically straight. Employing the distortion correction significantly reduced the bowing, as shown by the red line.

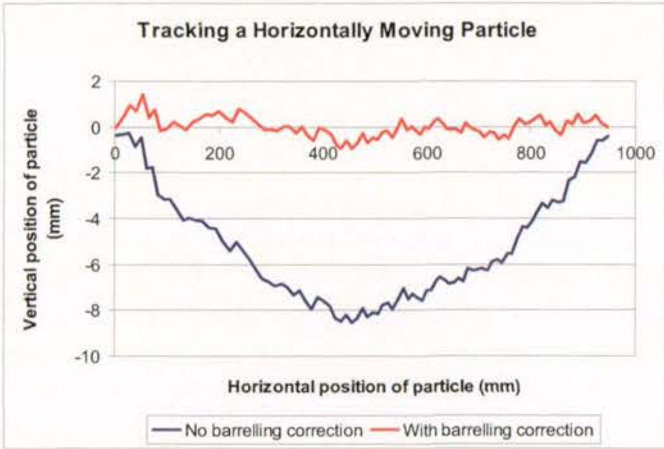

Figure 3.3. This graph shows how the track of a purely horizontally moving particle (tracked using the colour PTV technique described above) has been corrected for camera lens-induced barrelling distortion.

After the construction of the new aluminium model landslide and modifications to the slope surface, the slide repeatability was tested with this PTV technique. The results of this test are presented in Figure 3.4a where the landslide centre of mass location is plotted against time for ten of these runs. Although the repeatability was better then the original wooden block they still showed significant differences between runs.

After the introduction of lubricant and observing the minimum two minute timing between successive runs, the slide repeatability was assessed yet again. Figure 3.4b plots 25 runs after the PTFE surface spray was used as a lubricant. Experimental runs were completed at 2-minute intervals. Of note in this graph is the variation of the horizontal position time-histories during the 3 days of testing. The gradual decrease in velocity over time was determined to be due to the thin layer of spray-on lubricant wearing off.

Figure 3.4c plots the horizontal position time histories of 25 runs with the silicone grease lubricant. The sliding characteristics of this experimental configuration was rigorously tested to determine if there were any ill effects on the test repeatability through changes over time or through wearing. These tests consisted of over 180 separate runs over three days. The minimal variations shown between 25 of these separate trials indicate that the modifications made have increased the test repeatability, and that this regime is not significantly affected by time or wearing.

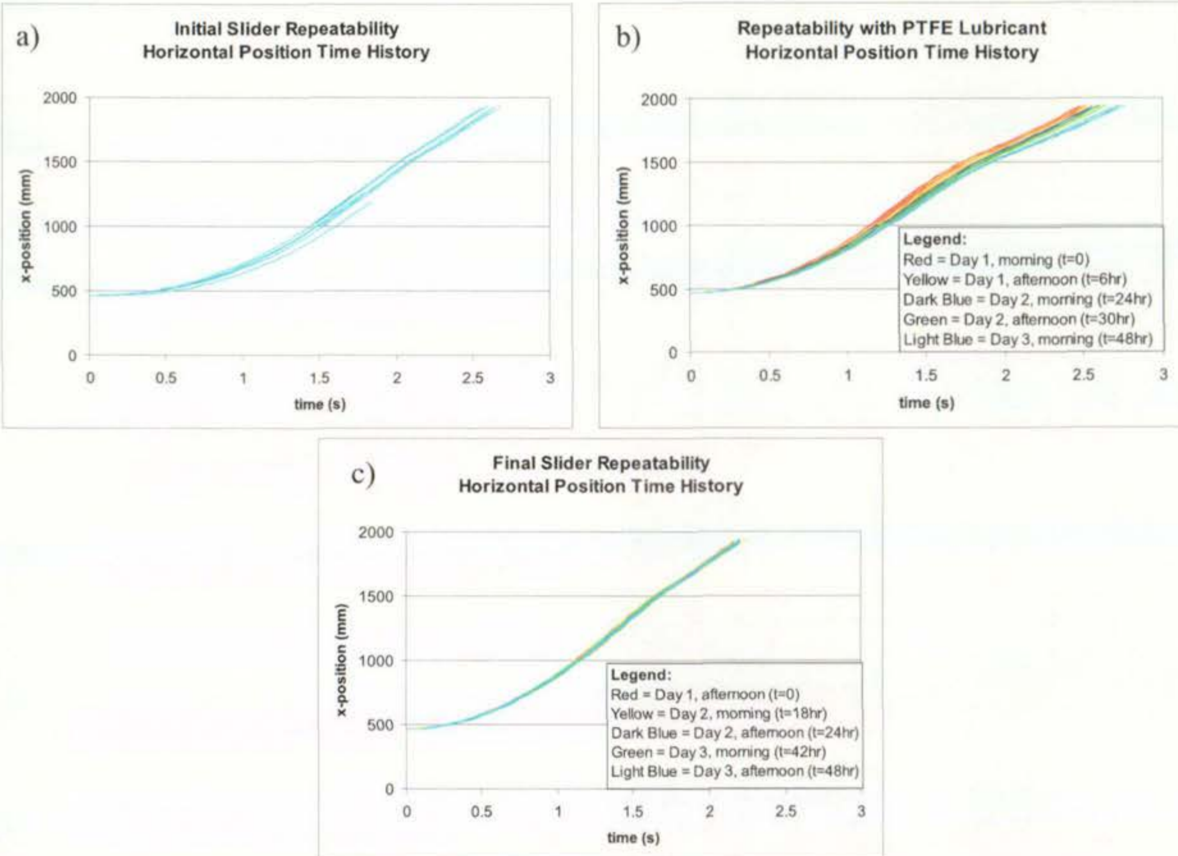

Figure 3.4. Repeatability of landslide centre-of-mass horizontal position time histories of: a) 10 runs immediately after the completion of the aluminium slider block, b) 25 runs using spray-on PTFE lubricant, and c) 25 runs after all modifications to the experimental configuration prior to the start of the main landslide tests. The light blue lines lay directly above the obscured red, yellow, dark blue, and green lines

The following figures illustrate the final repeatability achieved after all the modifications to the landslide block, slope surface, and lubrication. Figure 3.5 shows the horizontal and vertical position time histories of the landslide centre of mass for one of the landslide tsunami tests. Figure 3.6 plots the corresponding horizontal and vertical velocity time histories. The increased noise in these plots is due to the noise present in the position time histories being amplified by the differentiation process. Even amplified, this noise is low compared to the magnitude of the velocities.

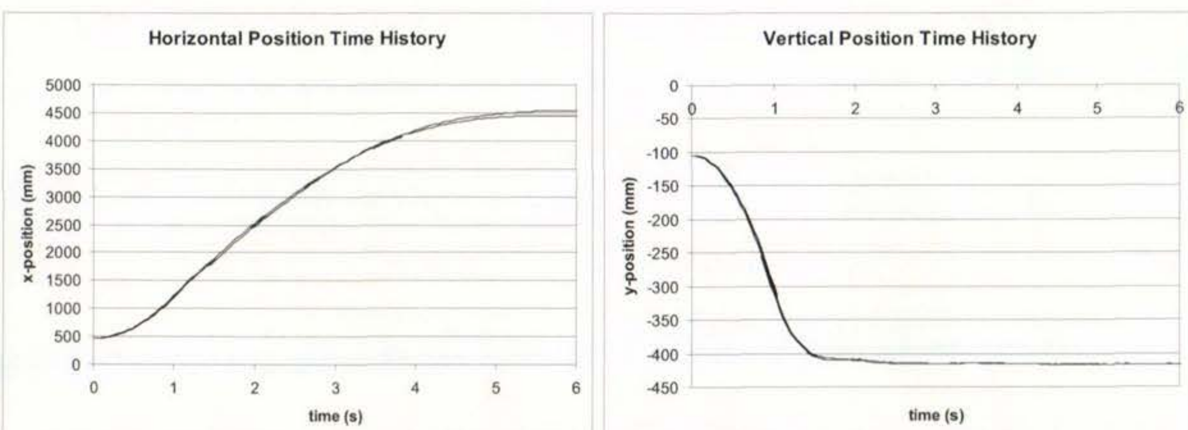

Figure 3.5. Example of repeatability of landslide centre-of-mass a) horizontal and b) vertical position time histories.

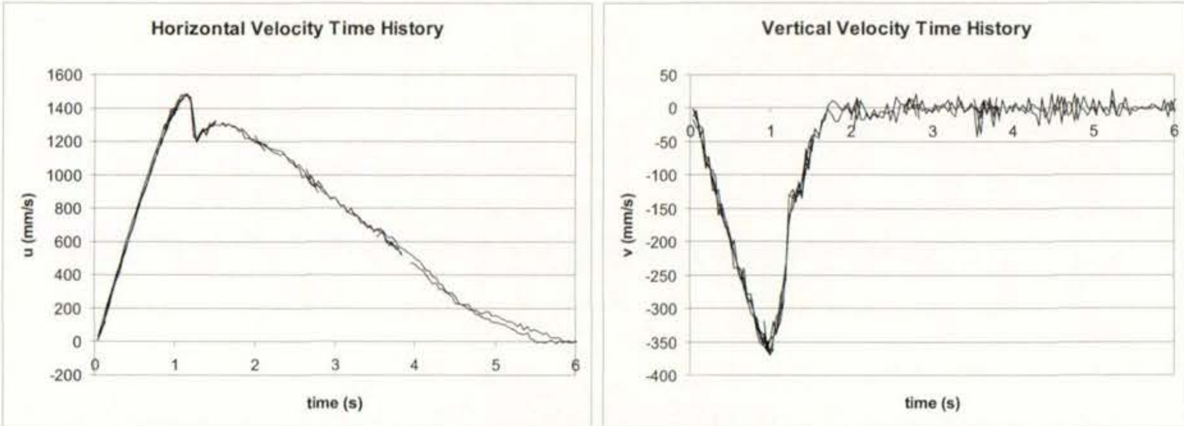

Figure 3.6. Example of repeatability of landslide centre-of-mass horizontal and vertical velocity time histories.

3.3 Measuring Water Levels With Laser Induced Fluorescence

For the past half-century experimentalists investigating laboratory water waves have relied predominantly on stationary point gauges to record water level time-histories. These gauges rely on sensing variations in electrical properties between two probes immersed in the water, and a calibration is performed to determine the relationship between the depth of immersion and either resistance or capacitance.

Point gauges are adequate for steady-state waves since wave amplitudes which don't change significantly as they propagate will result in the same water level time history as the wave profiles, as shown in Figure 3.7. However, if the waves are changing considerably as they propagate, then point wave gauges can only record the instantaneous water level as the wave passes the gauge, and information regarding spatial variation is lost.

These electrical point gauges, such as Resistance Wave Gauges (RWG) and Capacitance Wave Gauges (CWG), measure changes of water level over time at specific points in the flow. Many experimentalists have used these for recording both steady and unsteady wave phenomena. Lee et al (1993) used RWGs to measure water waves to compare with numerical results in a study into the interaction of transient non-linear waves with a submerged breakwater. The small-scale wave spectrum of ocean waves were recorded with RWGs by Gogineni et al (1990) to determine the radar backscattering from ocean surfaces.

Wiegel (1955), Rzadkiewics et al (1997), and Watts (Watts 2000) used RWGs to measure waves generated by the motions of submerged objects in studies of simulated underwater landslides. One gauge was located in the wave generation region to observe the non-steady wave characteristics, and additional gauges were placed downstream from the source mechanism to record the far-field wave amplitudes. Fritz et al (2003a) and (2003b) used CWGs to measure the wave heights of waves propagating from the impact of simulated sub-aerial landslides. Gauges were placed along their wave channel axis at 1m intervals, starting from the generation region. Raichlen and Synolakis (2003) used a two-dimensional array of gauges to measure the three-dimensional wave field generated by a submerged triangular wedge-shaped sliding block.

Numerical water wave models are able to predict entire wave fields, which include both spatial and temporal variations. Current practice is to compare the point gauge readings from experimental work with their equivalent time series in the model. If these agree relatively well, then they infer that the accuracy of their models extends past their point gauge locations to cover their entire wave domain (Enet et al. 2003). This may not be the case, and a technique needs to be developed to capture wave fields (spatial and temporal variation) experimentally, and to compare these results with wave fields generated computationally. In this way, the accuracy of these models can be more rigorously assessed.

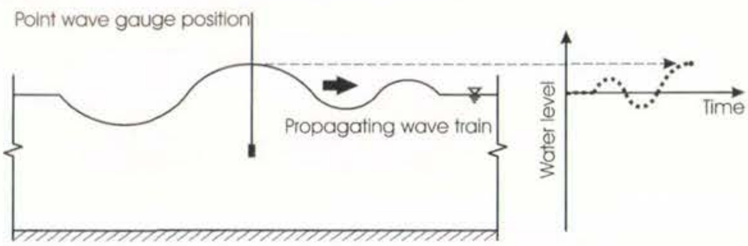

Figure 3.7. Typical wave tank with electrical point wave gauge.

The use of electrical wave gauges to measure wave amplitude time histories has many limitations. The first and most obvious is that they are point gauges, that is, they record water levels at discrete points in space. They are not able to discern the spatial variation of water level such as wave shape, or the evolution of water waves.

These resistance and capacitance wave gauges rely on sensing changes in the electrical properties of the water and the probes, and as such are influenced significantly by temperature and the chemical composition of the water. Therefore, these gauges require frequent and cumbersome calibration throughout the course of an experiment, and necessitate close monitoring of the surrounding environment to ensure variations in the aforementioned parameters do not greatly affect the readings. Also, a significant water depth is required as the gauges are immersed a specific distance, and as such are not suitable for measuring wave run-up due to the reduced water depth up a sloping beach. As the probes are physically in the water, they may affect the passage of waves, as water must flow around the wires. Surface tension on the gauges causes menisci to form and these are observed to reverse direction as the water depth increases and decreases, leading to possible errors in water level readings, especially at smaller laboratory scales.

Recording water levels optically has many advantages over wave gauges, the main one being its ability to capture the spatial variation of the waves as well as the temporal variations. However, recording under ambient light conditions has the problem of interference of the reversing menisci at the near and far sidewalls. In order to capture the wave profiles and run-up heights away from any sidewalls, where the effects of surface tension are significant, a means of distinguishing this internal vertical plane from the water levels at the sidewalls was developed. This was achieved by the use of Laser Induced Fluorescence (LIF). By projecting a thin vertical laser light sheet through the wave tank containing a low concentration of fluorescing dye, the surface wave profile in the illuminated plane was captured by a digital camera and stored on a PC. Analysis of the resulting image sequence and a transformation from image coordinates to physical coordinates allowed wave profile time histories to be plotted.

What follows is a description of the technique and the experimental set-up required to capture water levels at points in the flow, wave profiles over a length of water surface, and wave run-up heights. The laser and fluorescent dye combination used here in the development of this technique are described, as are the image capturing and data processing methods. To evaluate the performance of the LIF technique, the water level time histories from the LIF method are compared with results from simultaneous measurements with traditional RWGs.

There have been many applications of LIF in experimental fluid dynamical experiments in the past, but the use of it in quantitative water level measurements is apparently new. Previous uses have included visualisation of turbulent structures (Hsu et al. 2001; Lommer and Levinsen 2002; Shiono and Feng 2003), the determination of the presence and concentration of chemical and biological substances (Arnold et al. 1997; Houcine et al. 1996; Kozlova et al. 1991; Zhou et al. 1994), and in the visualisation of the spread and dilution of jets and plumes (Shy et al. 1997; Tian and Roberts 2003; VanLerberghe et al. 2000). Studies by Wang and Davidson (2001) into a profile tracking system for discharges into a co-flowing environment used the fluorescence of the dyed jet fluid as a means of measuring its extent of spread. The light intensity provided a measure of the variation of concentration of the dye in the jet and thus the extent of mixing with the ambient fluid was determined.

The optical technique used in this current experimental study relies on a similar principle in that the fluorescing dye highlights the interface between the water and air. In this case, however, variations in concentration, and hence light intensities, are not important. Only the interface between the two contrasting fluids is of interest.

Similar experiments looking at free surface profiles have been done in the past. The experiments of Mori and Chang (2003), looking into turbulent jet discharges into a wavy environment, used LIF to observe the jet centreline movement and free surface elevations simultaneously. Yeh and Ghazali (1987) used LIF in their study on the transition of a bore as it ran up a beach. Unlike the LIF experiments performed in this current experimental study, their LIF observations were qualitative only.

In this application of LIF a small concentration of fluorescent dye is stirred into the flume water, and illuminated with a vertical laser light sheet orientated parallel with the longitudinal axis of the wave tank. The dye in the water column fluoresces due to excitation by the laser light, and this contrasts with the surrounding darkness of a blackened room. A high-resolution digital video camera is used to record a series of images of the illuminated water. In each frame the interface between the regions of high and low light intensity marks the location of the free surface.

This LIF technique is well suited to water wave experiments as it has few of the drawbacks of electrical wave gauges, and is able to capture the spatial variations of waves as well as their temporal variations. This allows wave fields to be generated through the observation of the surface profile over time. This technique also has the capability to record the run-up heights of these waves along a sloping beach without interfering with the fluid motions.

Temperature dependence of recording wave time histories is eliminated with LIF, and the system only needs one calibration for each camera location and set-up. It should not change significantly due to changes in temperature, water composition and contamination. The LIF technique does not require any minimum water depth or probe submergence to work, and so can be used to measure wave run-up where wave gauges will not fit due to their size. Another advantage of non-intrusive measurement is the elimination of flow disturbance and surface tension and menisci reversal effects. Other advantages over electrical wave gauge methods include the ease of adaptability to the experimental set-up with regards to location and resolution. Resolution of the LIF wave records is dependent on the resolution of the digital video camera and available frame rate, and can be increased or decreased as necessary by adjusting the proximity of the camera to the subject. Higher resolutions come at the expense of smaller spatial coverage.

3.3.1 Equipment and Set-up

To provide luminescence, Lambda Physik's Lambdachrome Rhodamine 6G laser fluorescent dye was added to the wave tank water, to an overall concentration of approximately 0.1 mg/L. Rhodamine 6G has a typical excitation wavelength of approximately 525 nm and a higher emission wavelength of 555 nm.

A 1 mm thick neodymium yttrium vanadate (Nd:YVO_4) laser light sheet, with a wavelength of 532 nm, excited the dye solution. In this case, a Spectra-Physics Millennia IIs continuous-wave visible laser was used at a power output of 2.0 W. The light from the laser head was passed through a fibre-optic cable to a divergent laser sheet generator, so that the power level of the final light sheet was reduced to approximately 1.0 W due to losses in the fibre-optic connections. This combination of laser power output and dye concentration provided a distinct contrast at the water-to-air interface. The effects of minor variations in laser and dye properties were not significant, as the camera aperture was used to adjust the light levels reaching the camera CCD.

The laser was mounted directly above the water to project a vertical light sheet parallel to the long axis of the tank and the direction of wave propagation. The light sheet generator projected a divergent sheet with an approximate 45° spread. The height of the sheet generator above the water surface was 0.500 m. The equipment set-up used to capture wave profiles is shown in Figure 8. To maintain the 0.140 m distance of the light sheet relative to the outside face of the flume sidewall and the 1.155 m from the camera, the laser was mounted on the gantry trolley.

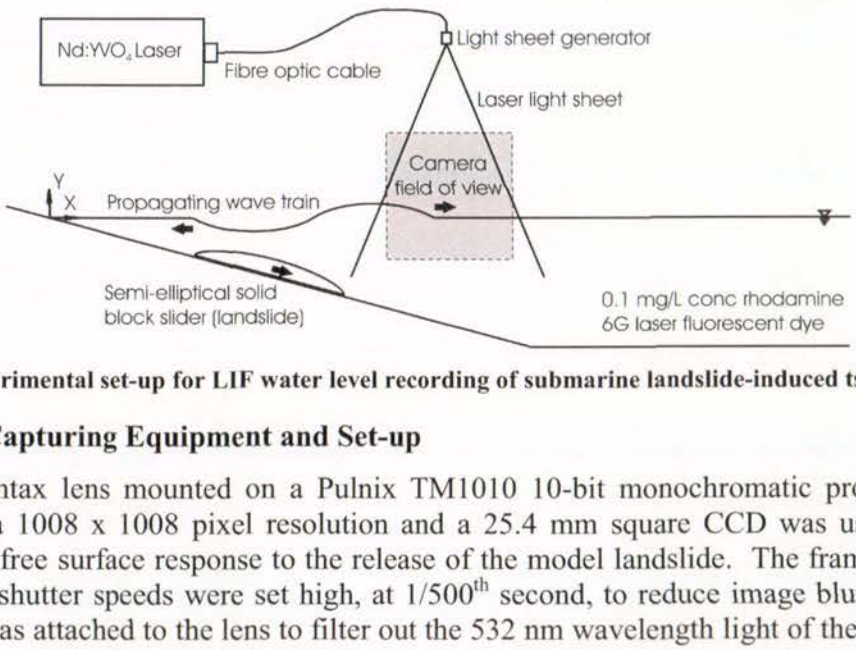

Figure 3.8. Experimental set-up for LIF water level recording of submarine landslide-induced tsunami.

3.3.2 Image Capturing Equipment and Set-up

A 25 mm Pentax lens mounted on a Pulnix TM1010 10-bit monochromatic progressive scan camera with a 1008 x 1008 pixel resolution and a 25.4 mm square CCD was used to capture images of the free surface response to the release of the model landslide. The frame rate was set to 15 Hz and shutter speeds were set high, at 1/500th second, to reduce image blur. An orange-colour filter was attached to the lens to filter out the 532 nm wavelength light of the laser light but allow the 555 nm wavelength light of the fluorescing water to pass through to the camera CCD.

LabVIEW was used to capture frames from the camera and store them in a 2 GB RAM buffer on a PC-based computer via a Bitflow frame-grabber card. The stored images were archived to hard disc as a sequence of JPEG images, where only the highest 8 bits of the intensity signal were stored in the JPEG files.

To eliminate the interference of the water line at the sidewall nearest the camera, the camera was mounted slightly higher than the water level to capture the water surface in the illuminated plane. As a result, this technique would be equally applicable for wave tanks with transparent sidewalls as for opaque-sided wave tanks or flumes provided there is adequate distance between the illuminated plane and the wall, as shown in Figure 3.9, or if the sidewall is low enough.

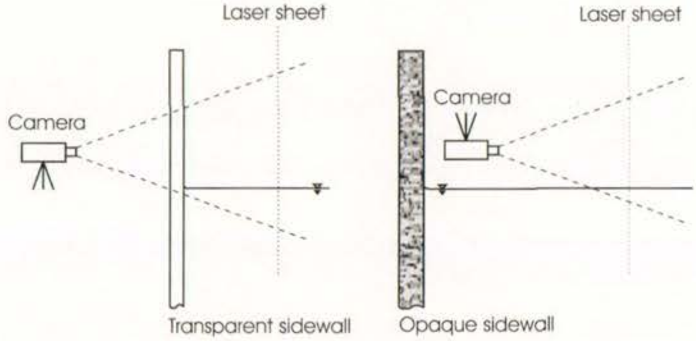

Figure 3.9. Camera mounting options for transparent and concrete sided wave tanks.

To allow different sections of water level to be observed without changing the camera location relative to the laser sheet, they were both mounted on the gantry trolley.

The block was pulled up the ramp until it was submerged at the correct depth and held in place until water motions ceased. The video capture was manually started a few seconds before the block was released. Upon release of the block, the LED connected to the release mechanism and visible in the camera frame turned off, indicating the block was in motion and signalled the start of a test. Recording stopped automatically after a pre-determined number of frames were captured, a time frame greater than the time for the waves to propagate to the end of the tank and return to the generation region.

The camera was mounted 1.155 m from the light sheet, giving a field of view of approximately 400 mm x 400 mm. This provided a resolution of approximately 3 pixels per millimetre in the illuminated plane. The camera was mounted 0.146 m above the still water level.

Although two minutes was sufficient time to allow the residual sub-surface water velocities, generated from preceding runs, to dissipate sufficiently so as to have negligible effects on the slider motions, it was insufficient time for the surface waves to completely dissipate. It was found that a small amplitude seiche was set up in the tank after each run, which was barely detectable by the naked eye due to their long period and wavelength.

Seiching is a phenomenon in which external forcing creates a free standing wave within an enclosed body of water that then oscillates at its natural frequency. The blue line in Figure 3.10 is a time-history plot of water level for an underwater landslide experiment at a point approximately 800 millimetres from the shoreline. Inspecting the water level after 1.7 minutes, the typical time required to record a run and retrieve the slider block, a 1-2 millimetre amplitude oscillation was seen to slowly dissipate over the remaining thirteen minutes. Even ten minutes after the block was released, the seiche had an amplitude of ±0.25 millimetres, a magnitude still able to be resolved with the LIF method. Woven paper mats were placed at the far end of the tank to try to dissipate the seiche, but were found to be effective at absorbing the higher frequency wave components, but ineffective with the low frequency seiche. The period of the seiche was of the order of 15 seconds.

As it was desirable to dissipate this seiche as quickly as possible to minimise the time required between successive runs, a number of wave absorption methods were investigated. Due to the cost and complexity of active methods, only passive wave absorption was considered. A technique used often and with success has been to put a very gentle (less than 1:10) slope at the far end of the tank (Ouellet and Datta 1986). The principle behind this technique is to promote the breaking of the waves and dissipation of the wave energy through turbulence and viscous effects. One of the advantages of this is its simple construction and implementation, and its effectiveness over a wide range of wavelengths and amplitudes. The main disadvantage of this method is the significant sizes of these slopes, which are often prohibitive in laboratory environments where space is at a premium.

A more compact wave dissipation structure with potentially similar effectiveness is based on the caisson. These have different arrangements of chambers and apertures that promote energy dissipation through viscous effects and resonance. The advantage of this form of wave absorption is its reduced size compared to sloped beaches, but they have the disadvantage of only being effective for specific ranges of wave properties and the requirement for tuning of the system to minimise the reflected waves (Lebey and Rivoalen 2002).

To dissipate the seiche observed in this tank, it was decided to implement the use of temporary baffle walls to compartmentalise the length of the flume. After a run, four gates were lowered into the tank at regular intervals along its length and left for approximately one minute, essentially dividing the 15-metre tank into five 3-metre long compartments. These walls limited the permissible wavelengths to less than 6-metres, and made it impossible to sustain a length-of-the-tank seiche. The gates were gently removed and the water allowed to settle further for three minutes. These gates covered the full height and width of the tank cross-section, and were made of 2 millimetre thick acrylic sheeting. 17 millimetre thick plywood gates were initially tested but were found to regenerate a substantial seiche when the gates were removed, due to the large volume of water that they displaced.

The black line in Figure 3.10 illustrates the effectiveness of the wave dissipation method utilising removable baffle walls. The baffles were lowered into the tank 80 seconds after the sliding block was released, left for 1 minute, and then removed. The seiche amplitude after a further 2 minutes, 6 minutes after the block was released, is approximately ± 0.13 millimetres. Without the baffles, it would take over 15 minutes for the seiche to dissipate naturally to this magnitude. After examining the results from the seiche tests, an interval of 6 minutes after slider release was settled upon as sufficient time for the seiche to dissipate and the next run to commence.

For the recording of wave run-up, the camera was rotated 75° so that the slope was vertical in the camera frame. This allowed the run-up position to be determined by inspecting the transition from high to low light intensity along a single pixel column of an image instead of diagonally across several pixel columns. The camera was positioned 0.100 m above the still water level and 0.462 m from the outer face of the sidewall. The laser was 0.120 m from the sidewall. The closer proximity of the camera to the laser sheet allowed a higher resolution of 0.233 mm per pixel to be recorded compared to the 0.399 mm per pixel resolution of the water level measurements. Figure 3.14 shows two examples of raw images of wave run-up with the rotated camera orientation.

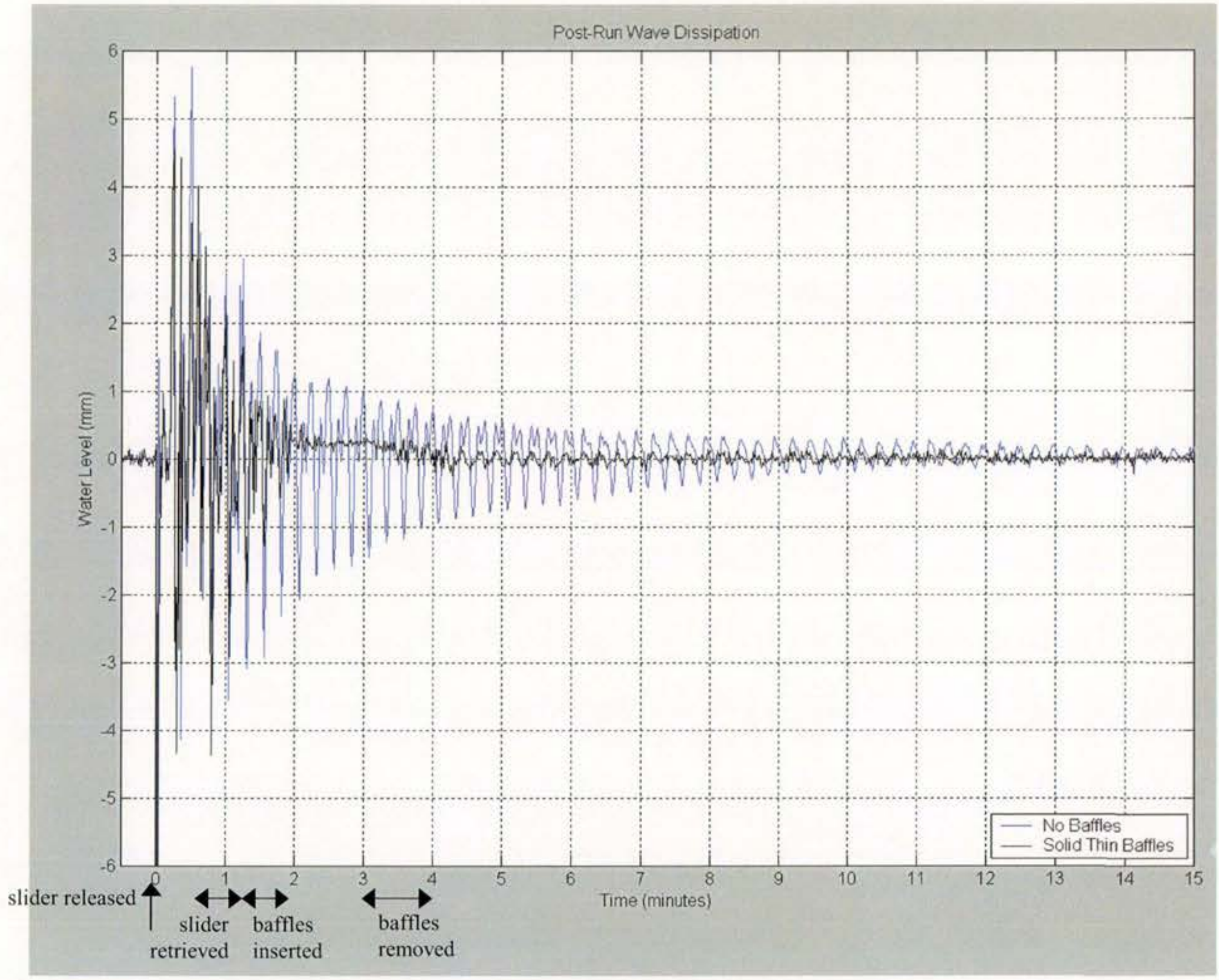

Figure 3.10. Comparison of water level time-histories, with and without the baffle-type seiche dissipation, after a typical test at a point approximately 800 millimetres from the shoreline.

3.3.3 Image Analysis

ImageStream (Nokes 2005c), an image processing software package developed by the University of Canterbury's Civil Engineering Fluids group, was used to determine the light intensity of each pixel in each of the saved JPEG images, on a scale between 0 and 255, to determine where in each image the interface between dark and light pixels occurred. This transition from the high intensity light of the fluorescing water to the low light intensity of the air signalled the location of the water surface. A simple scaling procedure then transformed the water level from pixel space to physical space.

An illustration of the image analysis process is illustrated in Figure 3.11. The top image is from a raw JPEG image of a 58 mm (crest-to-trough) wave passing from left-to-right. The middle image shows the intensity field of the same image where a range of shades indicates the relative intensities of each pixel. The lower image is a contour plot of the pixel intensity field. Due to the steep intensity gradient at the water surface, the contours appear as a single curve.

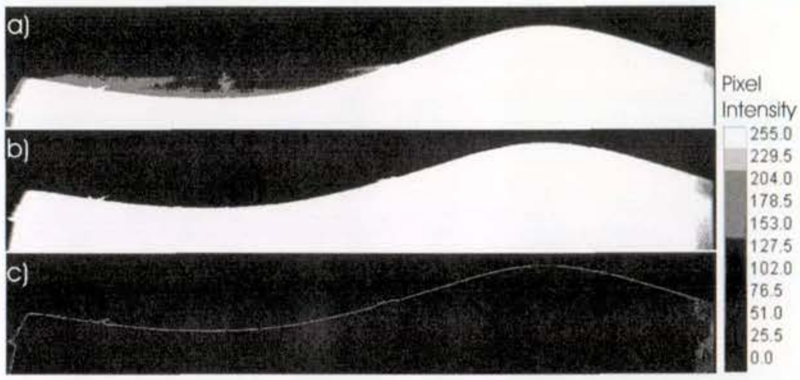

Figure 3.11. Illustration of image analysis process; a) raw JPEG image, b) pixel intensity field, c) pixel intensity contours.

It was important to adjust the camera properties such as focus, intensity thresholds, and gains such that the interface between water and air (dark and light) was as sharp and smooth across the water surface as possible. If these were adjusted correctly, as can be seen in Figure 3.12, then the transition from high to low intensity occurred very rapidly, typically across one pixel. The noise at the low intensities is due to flaring of the light fluorescing from the water. The threshold pixel intensity, the intensity above which a pixel was deemed to represent the fluorescent water and below which was air, was chosen such that it was above the noise level of the low light intensity of the dark background, yet below the noise level of the high light intensity of the fluorescing water. This threshold was held constant for all image sequences from a particular camera set-up and lighting condition, and was typically chosen to have a value of 230.

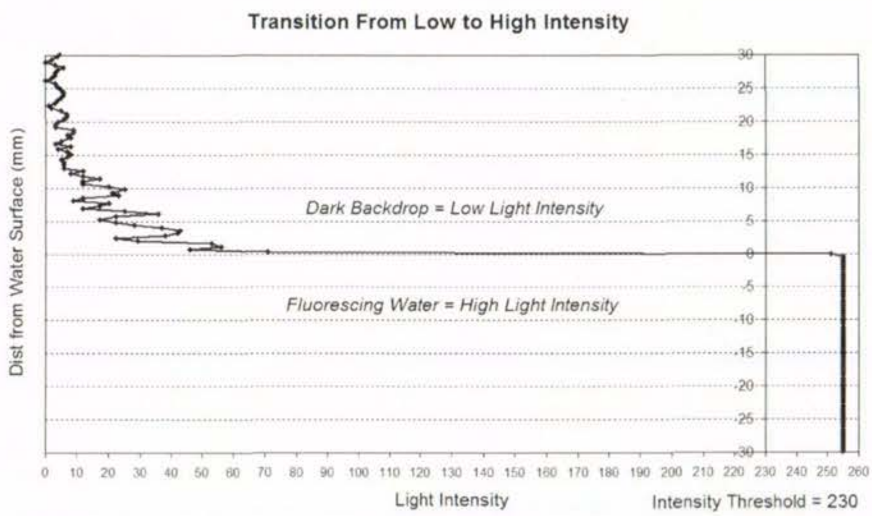

Figure 3.12. A typical transition from low to high intensity at the interface between air and water for a column of pixels.

Crossing the interface from water to air resulted in a rapid drop in light intensity. Selecting a higher intensity threshold defined the water surface as a point closer to the water's side of the interface, creating a downward bias. Lower intensity thresholds defined the water surface to be nearer the air's side of the interface, creating an upwards bias. However, the wave heights were not significantly affected by the value of the threshold intensity chosen. Several seconds of still water were recorded before each test to set the location of the still water surface for the chosen intensity threshold and the wave heights were measured relative to this. Any biasing of the wave heights due to the chosen value of the intensity threshold would have the same effect on the location of the measured still water level.

Instead of detecting changes in intensity at the pixel margins, linear interpolation between adjacent pixel values to the threshold intensity at the high-to-low intensity interface resulted in sub-pixel resolution. For instance, consider two adjacent pixels at the water-to-air interface with intensities of 30 and 250. For a threshold intensity of 230, the water surface is 10 times closer to the intensity=250 pixel than the intensity=30 pixel

On its path to the camera the fluorescent light from the illuminated water surface had to pass through the transparent acrylic sidewall. The acrylic sheeting had a refractive index of 1.51, compared to 1.0003 for air, and as such, the water level position was corrected for refraction errors. Also, as the camera was mounted slightly above the water level, to reduce interference of the water level at the sidewall, the data also required correcting for scaling errors due to parallax, as shown in Figure 3.13.

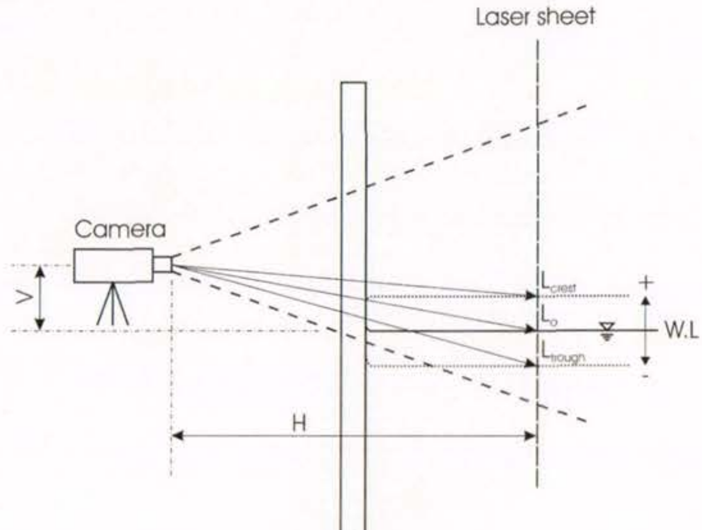

Figure 3.13. Water level errors due to camera angle (parallax).

The equation used to correct the water level for parallax errors is:

$$WL_{corrected} = \left[1 - \left(\frac{\frac{V}{H} * WL}{L_o} \right) \right] * WL \qquad \textbf{(3.1)}$$

where: WL = refraction-corrected water level (positive and negative)
V = vertical distance of camera above still water level
H = horizontal distance of camera from laser light sheet
$WL_{corrected}$ = water level corrected for camera angle-induced scaling errors
L_{crest} = distance from camera to positive water level
L_o = distance from camera to still water level
L_{trough} = distance from camera to negative water level

Due to surface tension and friction effects, the meniscus was convex as the wave ran up the beach, forming a rounded nose, but the water profile inverted to become concave as the water ran down the ramp, as seen in Figure 3.14. Note that the camera used to record these images was rotated 75° from the horizontal so as to make the 15° slope appear vertical. The left image illustrates the concave nature of the drawn-down water surface, and the right image shows the convex nose structure of the wave running up the beach. The surface tension effects at the small laboratory scale meant some consideration was required to define the location of the shore.

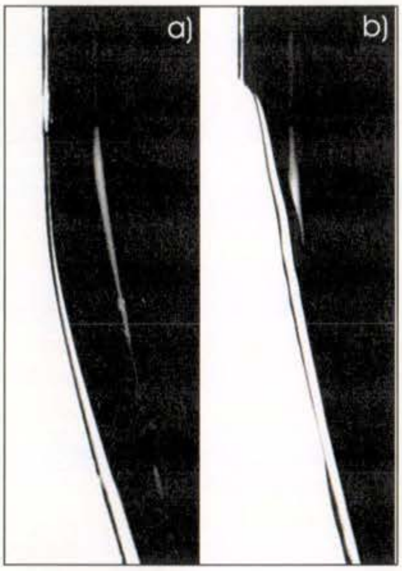

Figure 3.14. Raw images of a) wave run-down, and b) wave run-up, illustrating the issue of meniscus reversal. Image a) shows the draw-down of the shoreline as the landslide initially accelerates down the slope. Image b) shows the wave run-up that occurs moments later. Note that the 15° sloping beach is shown as vertical in these images.

There were several options available in defining the wave run-up/down, including the wetted length and linear and polynomial interpolation/extrapolation of the intersection of the water level and beach, but it was decided to use the water level at a specified distance from the ramp surface. This was used to try to negate some of the viscous effects present in the laboratory-scale experiments. This distance from the ramp was normally of the order of a few pixels, which scaled to between 1.0 to 1.5 mm, still significantly closer to the beach slope than is possible with electrical gauges. Evaluating water levels nearer to the slope surface would produce run-up time series severely affected by menisci changes, and further away from the beach surface could increase the distance to the true run-up length. The wave run-up height was determined by inspecting the interface between low and high light intensity from this single pixel column offset from the slope surface.

3.3.4 Evaluation of Performance of Laser Induced Fluorescence

One of the disadvantages of this LIF method is its inefficiency in covering large areas. Many wave tanks have dimensions in the order of tens-of-metres, and electrical point gauges can be placed at any location and spacing as each gauge is relatively independent of the others. Using the LIF method over long lengths in these tanks could require significantly reduced resolution, as each unit length would be resolved by fewer pixels. To overcome this, the water level time histories can be measured using this LIF technique at multiple locations. Although it would be desirable to record these images sequentially, using multiple cameras, it is not necessary so long as the experiment is sufficiently repeatable. A single camera was used to observe the flow in different locations for repeated runs of the same experiment. The camera and laser sheet were placed at the shoreline to record the propagation of the landslide-generated waves up the slope. The trolley-mounted camera and light sheet were then moved further downstream to observe the downstream propagation and continued evolution of the waves. The water profiles could then be combined to create a wide field of view of the surface response.

The main water surface profile experiments used 31 consecutive camera positions to record water levels from approximately 0.3 m upstream of the original shoreline to 10.1 m downstream. This allowed a large length of the water surface to be observed, over which the waves propagated and evolved.

Figure 3.15 illustrates the repeatability of the water level measurements. In this figure, three repeats were performed with the same experimental configuration (block specific gravity of 4.02, and initial submergence of 0.2 times the slider length). The water surface profiles 4.667 seconds after the block was released are plotted. These three repeats are actually made up of 93 individual runs, and the small misalignments of some of the peaks are due to the 15Hz camera frame rate only being able to resolve the timing to within ±0.0667 seconds. With typical wave speeds of approximately 1.5 metres per second, this corresponds to peak positioning of ±0.1 metres.

To compare the performance of the LIF technique with traditional wave gauge methods, several tests were performed with both the LIF and RWG wave recorders operating simultaneously. Three electrical gauges were placed parallel to the laser sheet in the region above the base of the slope, approximately 0.145 m apart. The gauges were placed behind the light sheet so that they did not obscure the fluorescing water surface from the camera.

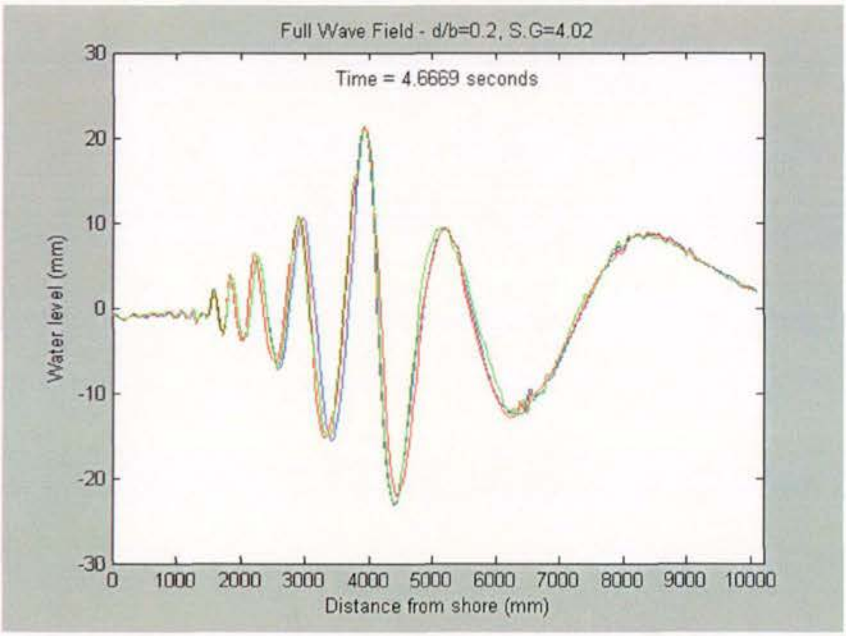

Figure 3.15. Example of repeatability of water level profiles. A wave field test repeated 3 times, measured 4.667 seconds after the slider was released.

Point LIF water level readings were determined at the same positions as the resistance wave gauges, and the two records compared. As the slider block was prismatic, the tank was a uniform width, and the light sheet and RWGs were in the central portion of the channel away from the boundary effects of the sidewalls, the waves generated were considered 2-dimensional.

Churchill Controls Limited manufactured the resistance wave gauges used in this comparison. They consisted of a pair of 275mm long 1.5mm diameter stainless steel wires spaced 12.5mm apart. The wires were immersed in the water and the electrical current that flowed between them was linearly proportional to the depth of immersion. A Wave Monitor Module carried the energising and sensing circuits and means for compensating for the resistance of the probe connecting cables. The current was sensed by the wave monitor, which provided an analogue output voltage proportional to the instantaneous depth of immersion. An A/D converter provided this data as a digital output at 16 Hz for storage on a Campbell Scientific CR10X datalogger before being uploaded to a PC, separate to that used for the LIF data. Output files were in a comma separated value (CSV) text format with each probe reading stored as raw millivolts tagged with date and time data. The RWGs were not affected by lighting conditions or the dye necessary for the LIF technique (Churchill Controls Ltd 1977).

Calibration was needed to convert the raw probe data from millivolts to a length scale. Each probe was firstly set up with a standardised immersion depth of 70.0mm. The wave monitor was then adjusted to compensate for the resistance of each probe connecting cable to ensure the 70.0mm immersion equated to a zero voltage output.

The raw voltage output can be correlated to wave height by varying the depth of immersion of each probe in still water by a known amount and noting the corresponding change in output voltage. Raising and lowering the probes in 5 mm increments and noting the corresponding change in the output voltage, the immersion depth of the probes were plotted against output voltage to find the relating constant, as shown by

$$dv = C \times V \tag{3.2}$$

where dv = vertical displacement relative to initial 70 mm depth (mm)
C = constant
V = output voltage (V)

Tests in which large, moderate and very small waves were created were used to compare the two techniques across a range of wave sizes. Comparisons for the largest and smallest waves are presented in Figure 3.16. Note that each horizontal gridline represents two pixels in the plot of the largest waves, and one pixel in the small wave height plot.

The RWGs were calibrated to an accuracy of 0.2 mm. The LIF method was calibrated completely independently by converting pixel lengths into actual lengths, as described previously. The 1008 by 1008 pixel resolution of the camera captured a field of view of approximately 450 mm by 450 mm, resulting in a resolution of 0.466 mm/pixel. With the LIF technique able to resolve wave heights down to sub-pixel level, the water levels were captured at an absolute resolution and accuracy of better than 0.1mm. As illustrated in Figure 3.16, the LIF method produced point measurements of water level comparable to those of the RWGs.

Repeatability was also important because it allowed different testing methods to be used sequentially, instead of simultaneously, resulting in reduced experimental complexity. One of the other testing methods used in this study was Particle Tracking Velocimetry (PTV). This method was used to track the motion of the slider and to create internal velocity fields. Due to the repeatability of the experiments, a coupled PTV-LIF technique, like the one by Cowen et al (2001), to record PTV and LIF information simultaneously was not necessary. These different techniques were used to observe different aspects of the water response to underwater landslide motion.

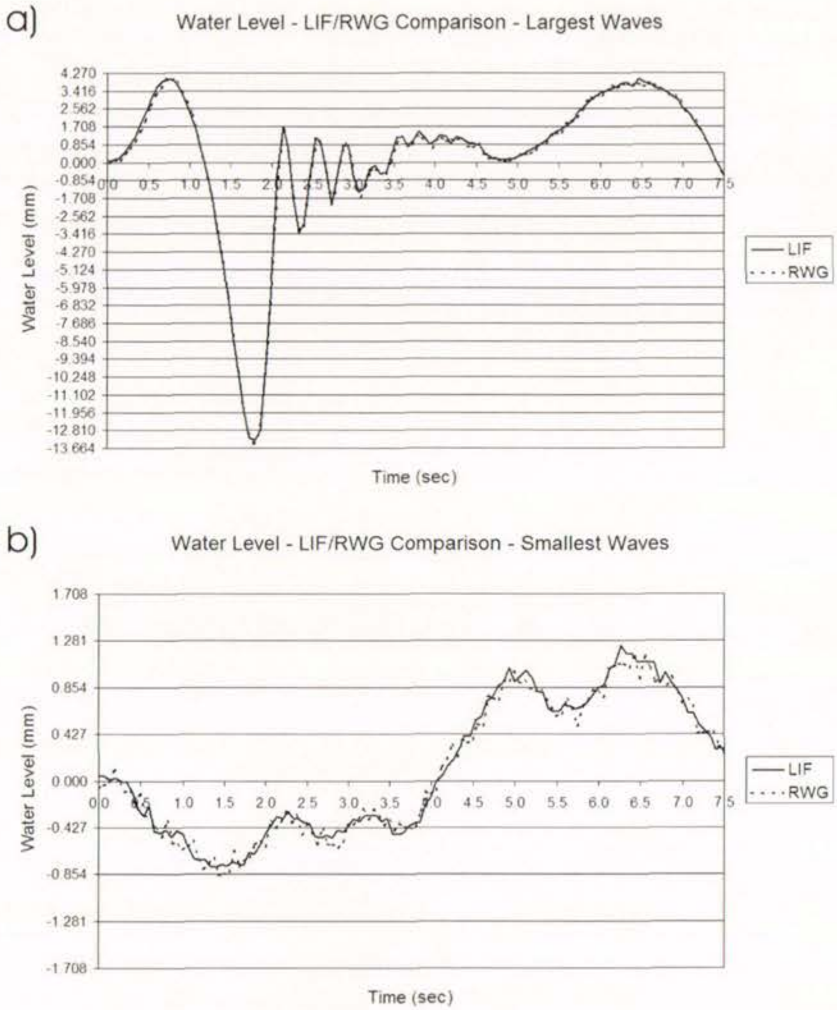

Figure 3.16. Plots of LIF and RWG for comparison of performance for large and small wave heights. Note the different gridline intervals, as one pixel = 0.427 mm.

3.4 Measuring Sub-surface Velocities with Particle Tracking Velocimetry

PTV was used to measure the sub-surface water velocities in two areas of interest. The first was at the base of the slope, the position at which the landslide was travelling with maximum velocity. The flow structure over the landslide and in the wake region was observed. The second position of interest was far downstream, beyond the final resting place of the slider. In this region, the water velocities were unaffected by the landslide motions and so the sub-surface velocities under the propagating wave train could be distinguished.

To view the water velocities, the water was seeded with fine near-neutrally buoyant particles. These suspended particles were illuminated with a white light sheet. The contrast between these illuminated particles and the black background was recorded with a digital video camera. PTV software then matched these particles from frame-to-frame to determine the velocities present in the water.

3.4.1 Equipment and Set-up

The flume, landslide, and slope configuration was identical to that used for the LIF and landslide tracking measurements. All the lights in the room were turned off and a black sheet was placed behind the flume to provide a dark background.

The water was seeded with fine pliolite resin particles with diameters in the range of 180-250 μm. Pliolite resin has a specific gravity slightly greater than that of water, and as such, settles out over time. However, the fall velocities of these particles are negligible compared to the velocities of the landslide experiments. Therefore, for these experiments, the particles were considered to be neurally buoyant.

Before being added to the flume, the pliolite particles were mixed with approximately 150 ml of water. A small quantity of surfactant was also added to allow the hydrophobic particles to mix with the water. Enough of this pliolite particle slurry was added to the flume to have approximately 2000 particles illuminated in the camera frame. The particles were then mixed throughout the flume fluid and allowed to rest for a period of time such that the residual stirring motions had decayed but not so long as to allow the particles to settle out.

To illuminate the particles, two light boxes were placed above and below the flume to project a white light sheet into the pliolite-seeded water. The light boxes consisted of an encased 2 kW halogen tube, from which light was allowed to escape only from a 400 mm by 5 mm slit. The horizontal coverage of the light was sufficient to ensure particles at the edges of the filming area were also illuminated. A light sheet thicker than the laser sheet was desirable as fewer particles moved in and out of the light sheet between frames, enhancing the matching process. The light sheets were placed 0.150 m from the outer surface of the sidewall. These light boxes were moved to the different places of interest in the flume.

3.4.2 Image Capturing Equipment and Set-up

The camera and computer system used in the LIF measurements was also used to capture the sub-surface velocities. The shutter speed was set high, at 1/500th second, to reduce blurring of the particles.

The camera was mounted on a tripod, at a distance of approximately 1.02 m from the flume sidewall. The field of view was approximately 400 mm x 400 mm when mounted in this configuration, approximately 1.17 m from the light sheet. This provided a resolution of approximately 2.5 pixels per millimetre in the illuminated plane. At the upstream position, the camera was centred 0.190 mm below the still water level. At the downstream location, the field of view of the camera was not large enough to capture the entire water depth. As such, image sequences were recorded of the upper half and lower half of the water column separately. The camera was 0.100 m below the water surface when observing the upper section and 0.330 m below the surface when recording the lower section.

To signal the start of the landslide test, the release mechanism LED was placed in the field of view of the camera.

3.4.3 Image Analysis

The JPEG image sequences were input into FluidStream. The PTV software identified the pliolite particles and tracked them through the image sequence. The tracks of the particles were corrected for barrelling distortion before being used to generate interpolated velocity fields of the two observed areas.

Figure 3.17 shows the particle tracks for one of the tests. These tracks span the time from 0.3533-6.133 s after landslide release. This observation region, spanning the entire water depth from 6.828-7.228 m downstream, was beyond the final resting place of the block. Clearly visible are the elliptical fluid particle motions in the upper regions of the water column, and the motions parallel with the flume floor at the bottom of the image. Particle orbits are in a clockwise direction. The discontinuity in the particle tracks at approximately y = -202 mm is the join between the two camera positions used to capture the entire water depth. The velocity field results from these tests are presented in Chapter 4.

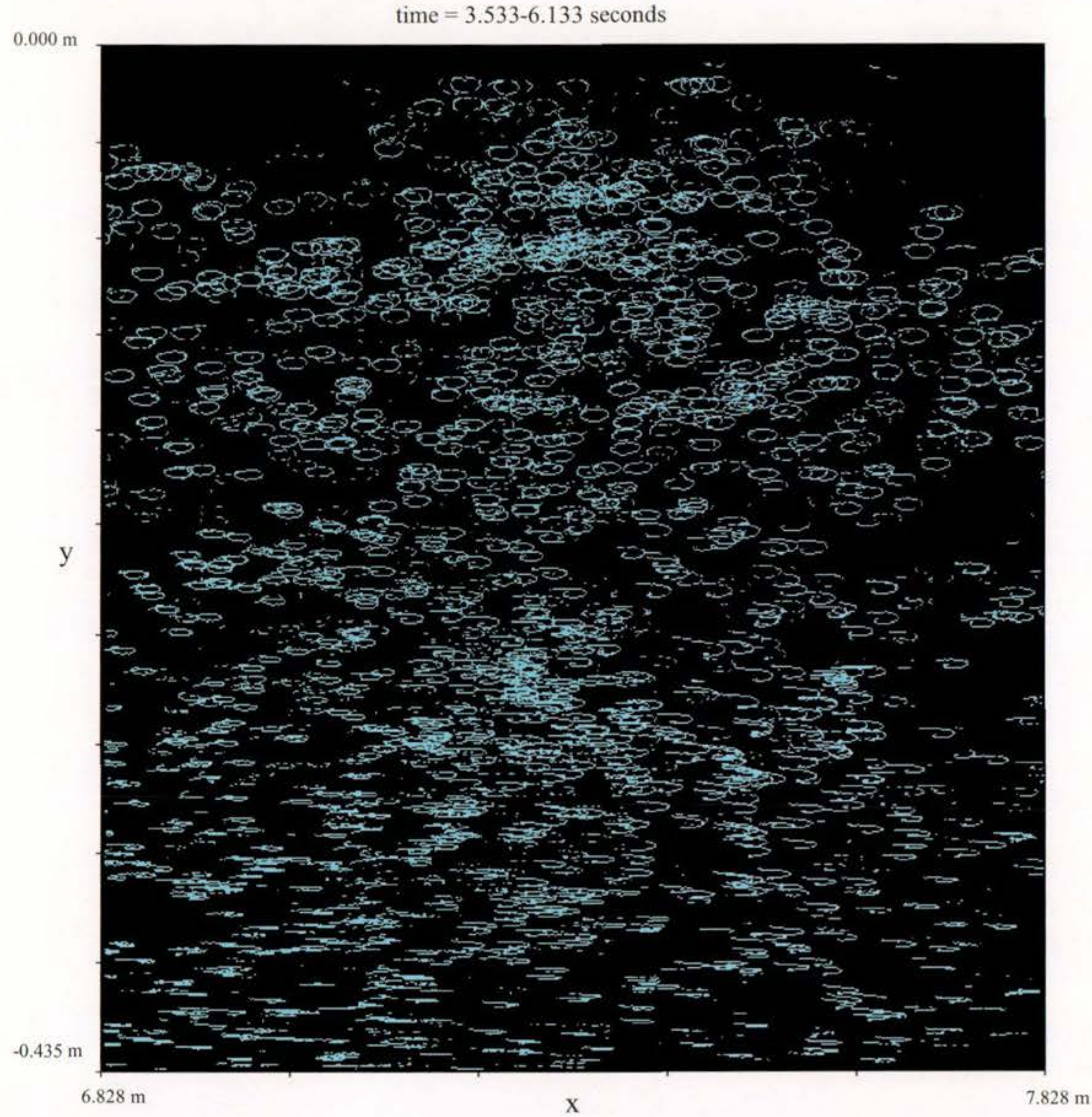

Figure 3.17. Particle tracks from the PTV experiments for times between 3.533 and 6.133 seconds. The entire water depth is shown for a region between 6.828 and 7.228 m downstream. Particle orbits are in a clockwise direction.

Chapter 4: Experimental Results and Discussion

Using the techniques presented in Chapter 3, an experimental programme was completed to measure the wave fields generated by laboratory underwater landslides with fifteen combinations of specific gravity and initial submergence. Landslide motions and sub-surface water velocities were also measured. Specific gravity is defined as the ratio of the total unsubmerged mass of the block, m_b, and the mass of water displaced by the landslide, m_o, as shown in Equation 4.1. A combination of polystyrene blocks, water, and lead shot were placed into the cavities within the block to increase the total block mass, m_b, to achieve the desired specific gravity. The mass of displaced water, m_o, was measured as 2.417 kg. Given a density of water, ρ_o, of 999 kg/m^3 at 16°C, the volume of the landslide, v_b, was calculated as 2.419 litres. In air, the empty block mass was 3.930 kg.

$$\text{specific gravity} = \frac{m_b}{m_o} \tag{4.1}$$

Equation 4.2 defines the non-dimensional initial submergence as the ratio of the depth of water directly above the landslide centre of mass at its initial starting position, d, and the length of the landslide block along the slope, b.

$$\text{initial submergence} = \frac{d}{b} \tag{4.2}$$

This chapter begins with an overview of the experiments performed, including the combinations of specific gravity and initial submergence. Following this are details of the landslide kinematics, such as maximum landslide velocity and initial acceleration. Results from the water level measurements of wave amplitudes and run-up/down are then discussed. A qualitative presentation of sub-surface velocities concludes the chapter.

4.1 Experimental Programme

The testing programme consisted of a model landslide block with a combination of five different specific gravities and five initial submergences, as presented in Table 4.1. Test SG5-IS5 combined the highest specific gravity with the shallowest initial submergence, and produced the largest water level response. SG5-IS1 combined the heaviest specific gravity with the deepest submergence, while SG1-IS5 combined the lightest specific gravity with the shallowest submergence, and both of these produced some of the smallest responses. A range of combinations were not tested as they were expected to create small waves and suffer from resolution issues.

For each combination of specific gravity and initial submergence, PTV was used to measure landslide position time histories and LIF was used to record water surface profile time histories. The landslide motions were recorded before and after the water level measurements to check the sliding characteristics had not changed during that time. The sliding characteristics were found to be consistent throughout the testing process.

To check the repeatability of the LIF processes, the SG5_IS4 combination had water levels recorded three times. As this test was found to be repeatable, as shown in Figure 3.15, it was decided that only one set of measurements was necessary for subsequent combinations, providing significant time savings.

Sub-surface water velocities were measured for one combination, SG1_IS5. This combination was chosen because the lightest density produced water motions that the PTV software could satisfactorily resolve, and the longest runout length allowed the block to slide for a considerable length and produce a well-defined turbulent wake.

Table 4.1. Experimental test combinations of Specific Gravity (SG) and Initial Submergence (IS).

Specific Gravity:							
	5 variations		Lightest	**SG1**	1.63		
				SG2	2.23		
				SG3	2.83		
				SG4	3.42		
			Heaviest	**SG5**	4.02		
				SG = Specific Gravity			
Initial Submergence:							
	5 variations		Deepest	**IS1**	0.5	d/b	
				IS2	0.4	d/b	
				IS3	0.3	d/b	
				IS4	0.2	d/b	
			Shallowest	**IS5**	0.1	d/b	
				IS = Initial Submergence			
				d = depth of water above landslide CoM			
				b = block length (500mm)			
Combinations tested:							
		IS5	**IS4**	**IS3**	**IS2**	**IS1**	
	SG5	*	*	*	*	*	
	SG4	*	*	*	*		
	SG3	*	*	*			
	SG2	*	*				
	SG1	*					

4.2 Landslide Kinematics

The landslide kinematics were determined by measuring the position time history of the block's centre of mass using PTV. The instantaneous position of the landslide is important because it can be related to the characteristics of the wave field. Velocity and acceleration magnitudes were calculated by differentiating and double-differentiating the position data with respect to time respectively.

Much of the data presented in this chapter has been non-dimensionalised. Lengths such as water levels, run-up heights, and downstream positions have been non-dimensionalised by the landslide length,b.

$$\text{non-dimensional length} = \text{length} / b \tag{4.3}$$

Accelerations have been non-dimensionalised by the gravitational acceleration,g.

$$\text{non-dimensional acceleration} = \text{acceleration} / g \tag{4.4}$$

Velocities have been non-dimensionalised in the following way.

$$\text{non-dimensional velocity} = \text{velocity}\Big/\sqrt{gb} \quad \textbf{(4.5)}$$

Times have been non-dimensionalised in the following way.

$$\text{non-dimensional time} = \text{time}\sqrt{g/b} \quad \textbf{(4.6)}$$

4.2.1 Maximum Landslide Centre-Of Mass Velocity

An example of the landslide centre of mass velocity time history is shown in Figure 4.1 for the SG3_IS5 combination. The landslide velocity increases almost linearly from rest and reaches a maximum at the bottom of the slope, at which point the block slows and comes to rest along the flume floor. As indicated by the increasing velocity of the landslide at the toe of the slope, terminal velocity is not reached. Velocity time histories for other combinations exhibited similar behaviour. This can be contrasted with the slider motions of Watts (1997), in which his landslides rapidly reached terminal velocity.

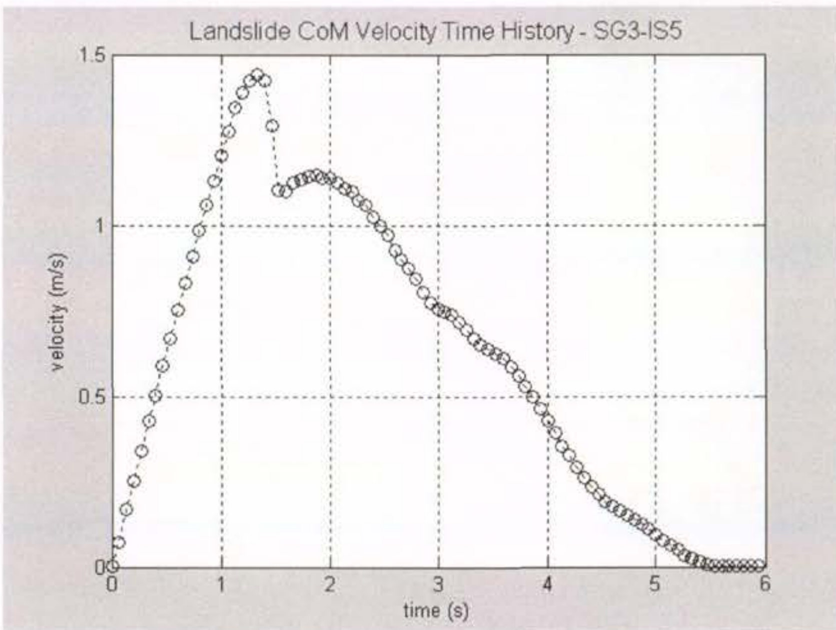

Figure 4.1. Landslide centre of mass velocity time history for SG3_IS5 test.

Inspecting Figure 4.2, the non-dimensional maximum landslide velocity increases non-linearly with increasing specific gravity and decreasing initial submergence. Higher specific gravities induce higher accelerations, enabling the landslide to reach higher velocities for the same slide distance. Decreasing initial submergences increases the slide length available, hence the longer duration of acceleration and higher velocities attained.

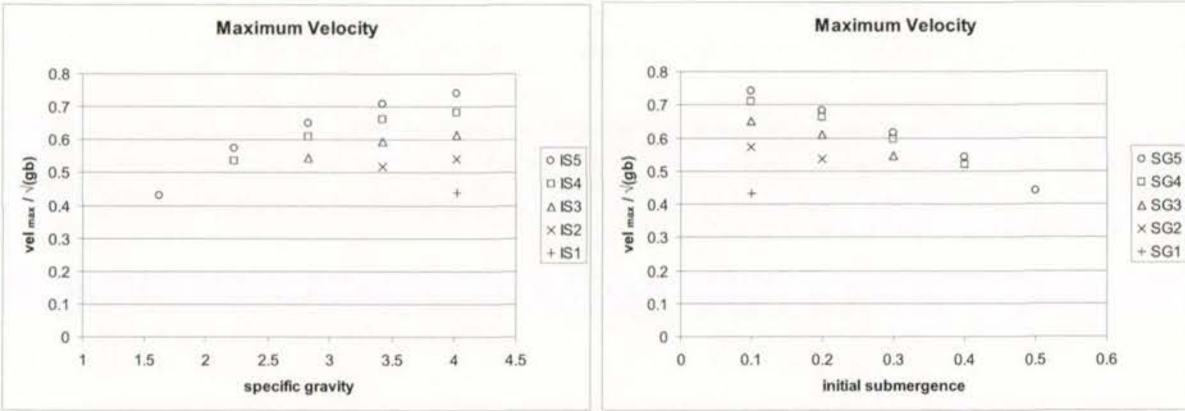

Figure 4.2. Maximum landslide centre of mass velocity as functions of specific gravity and initial submergence.

4.2.2 Initial Landslide Centre-Of Mass Acceleration

Landslide accelerations are a key parameter in characterising the generated wave field. Landslide specific gravity indicates the difference in density between itself and the surrounding water. The measured acceleration is proportional to the specific gravity, but it also takes into account factors such as friction that specific gravity alone cannot characterise.

Figure 4.3 is a time history plot of the landslide centre of mass acceleration for the SG3_IS5 test. The form of the acceleration plot is similar for all the specific gravity and initial submergence combinations, with only the magnitude and timing of the accelerations differing. The rapid increase to the peak acceleration typically occurs within two camera frames, or 0.133 seconds. Initial acceleration is taken as this peak value. The acceleration decreases slightly as the landslide progresses down the slope, before a rapid deceleration as the block reaches the base of the slope and transitions to sliding along the flume floor. A phase of roughly constant deceleration occurs as the landslide slows and finally stops. During the landslide experiments of Watts (1997), the accelerations peaked almost instantaneously before rapidly decreasing as the block approached terminal velocity. His acceleration time histories were typically measured for durations of 0.6 seconds.

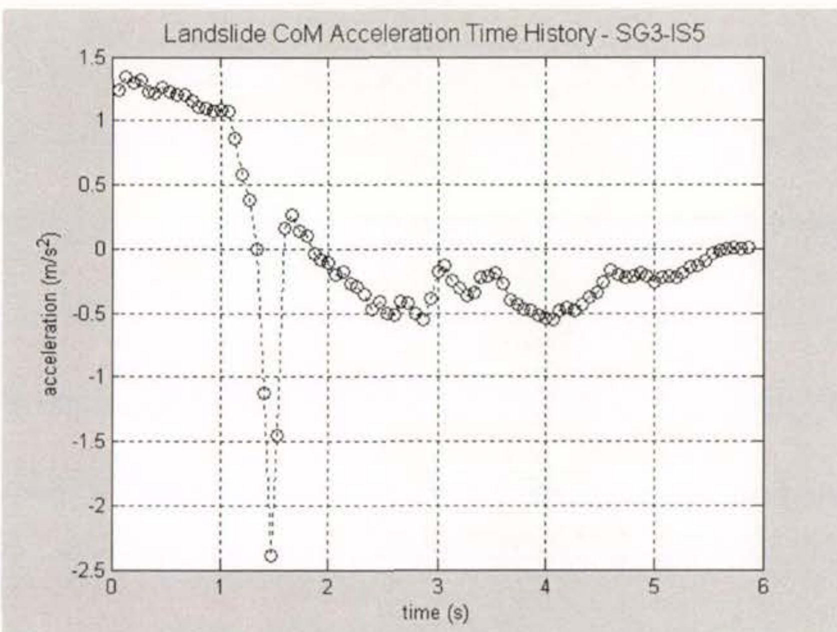

Figure 4.3. Landslide centre of mass acceleration time history for SG3_IS5 test.

Figure 4.4 illustrates the independence of non-dimensional initial acceleration on initial submergence, and its dependence on specific gravity. The proximity of the landslide to the free surface does not have a significant effect on the acceleration, only the duration over which it operates. As a landslide with a specific gravity of 1.0 should theoretically produce zero acceleration, it is clear, from the plot of non-dimensional initial acceleration versus specific gravity in Figure 4.4, that the landslide initial acceleration is non-linearly dependent on specific gravity.

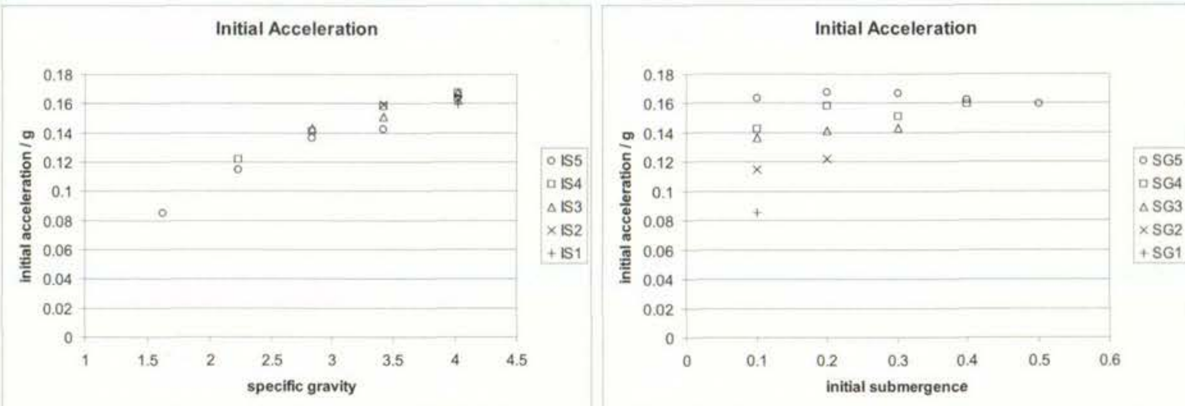

Figure 4.4. Initial landslide centre of mass acceleration as functions of specific gravity and initial submergence.

4.2.3 Maximum Landslide Centre-Of Mass Deceleration

The non-dimensional maximum centre of mass deceleration values plotted in Figure 4.5 are indicators of the magnitude of the sudden deceleration experienced by the landslide as it reaches the toe of the slope. This is seen in the acceleration time history of the SG3_IS5 test as the large spike at approximately 1.4 s with a magnitude of -2.393 m/s^2. It should be noted that these deceleration values are less reliable due to the short duration of rapid deceleration and the possibility the 15 Hz camera frame rate was not able to fully resolve the peak deceleration.

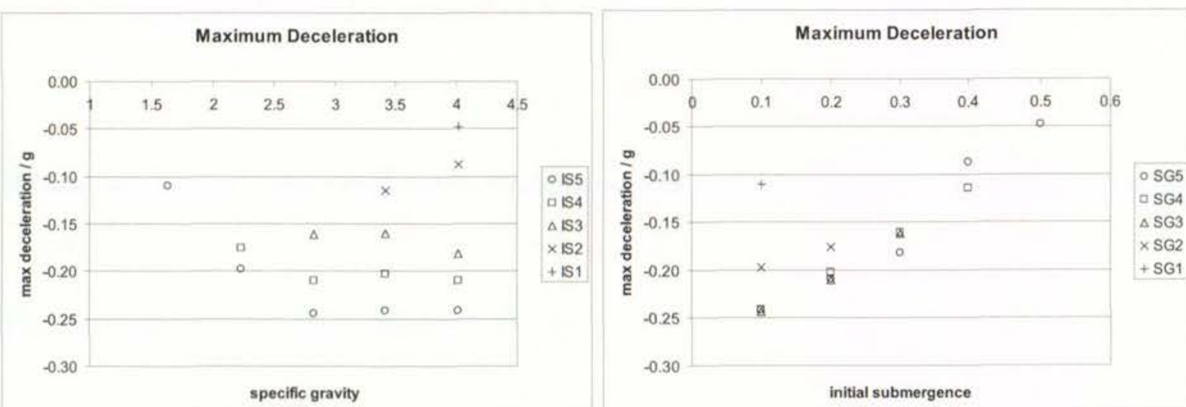

Figure 4.5. Maximum landslide centre of mass deceleration, measured at the toe of the slope, as functions of specific gravity and initial submergence.

4.3 Wave Fields

The evolution of the waves through space and time can be observed by looking at the water surface time histories and profiles respectively. The changes in the periods, lengths and total number of waves can be inspected. Observations of the 1st crest, 1st trough, and 2nd crest indicate that the waves generated by underwater landslides continually evolve as they propagate. The maximum and minimum water levels give insights into the dependence of the generated wave field on the initial landslide characteristics. Analysis of the water surface profile within the frequency domain yields further insights into the wavelength components of the wave fields.

The extent of wave run-up and run-down at the shore are also important parameters, as it is the wave magnitudes at the shore that are of immediate concern in practical situations. Indications of the likely draw-down and wave inundation, as well as the times at which these occur, are useful for communities with assets situated in the coastal area.

Seismologists use the energy released during an earthquake to quantify the magnitude of the event. Similarly, wave potential energy, landslide potential energy, and landslide kinetic energy are possible measures as to an underwater landslide's potential for destruction. The time histories of the various energy forms also provide insights into the mechanisms in which the energy is transferred from the landslide potential energy into other forms of energy, such as the wave field. This research appears to be the first experimental tsunami study in which full water surface profile time histories have been generated. The wave potential energy can be determined from this spatial and temporal water level information. Unfortunately it is not practicable to measure the internal kinetic energy of the water motions.

4.3.1 General Wave Field Description

Figure 4.6 shows the water surface profiles of the SG3_IS5 test at successive times between 0.600 s and 5.600 s. Present in the first frame at time = 0.600 s is the 1st crest, 1st trough, and the beginnings of the 2nd crest propagating downstream. The solid black bars indicate the approximate position of the landslide. The wave trough causing the run-down observed at the beach is also present as a trough propagating upstream. The following frames illustrate the evolution of these waves as they propagate. The 1st crest amplitude continues to increase initially, peaks, and then gradually decreases as the wave enters deeper water and its wavelength increases. The 1st trough and 2nd crest also exhibit this behaviour, although at later times. The continual generation of small amplitude waves with short wavelengths at the upstream end creates a propagating wave packet. Similar plots of water surface profiles are included in Figures A.1-A.15 in the Appendix for all fifteen specific gravity and initial submergence combinations.

Figure 4.7 shows the water surface time histories of the SG3_IS5 test at successive positions down the flume between 0.500 m and 5.500 m. Presenting water level time histories in this way simulates the information available from point gauges, such as electrical resistance and capacitance gauges. Present in the first frame at a position of 0.500 m downstream of the original shoreline are the first four wave crests and troughs. The water surface is essentially flat after time = 2.500 s because the waves at the trailing end of the wave train are being generated downstream of this location and hence do not propagate past this position. This implies that the waves generated beyond this location do not have an upstream propagating component. The time history at 1.500 m clearly illustrates the decrease in amplitude of successive waves. The waves at successive downstream positions have increasing periods, as the waves have a greater distance and time to disperse.

The water level profiles and time histories in Figures 4.6 and 4.7 are presented in a continuous manner in Figure 4.8. The plots in this figure display water level, on the vertical axis, against time and downstream position on the horizontal axes. The red colours indicate positive water levels, or wave crests, and blue represents the negative water levels of troughs. The partially obscured black line indicates the downstream position of the landslide centre of mass. The evolution of the waves and the generation of the wave train are clearly illustrated.

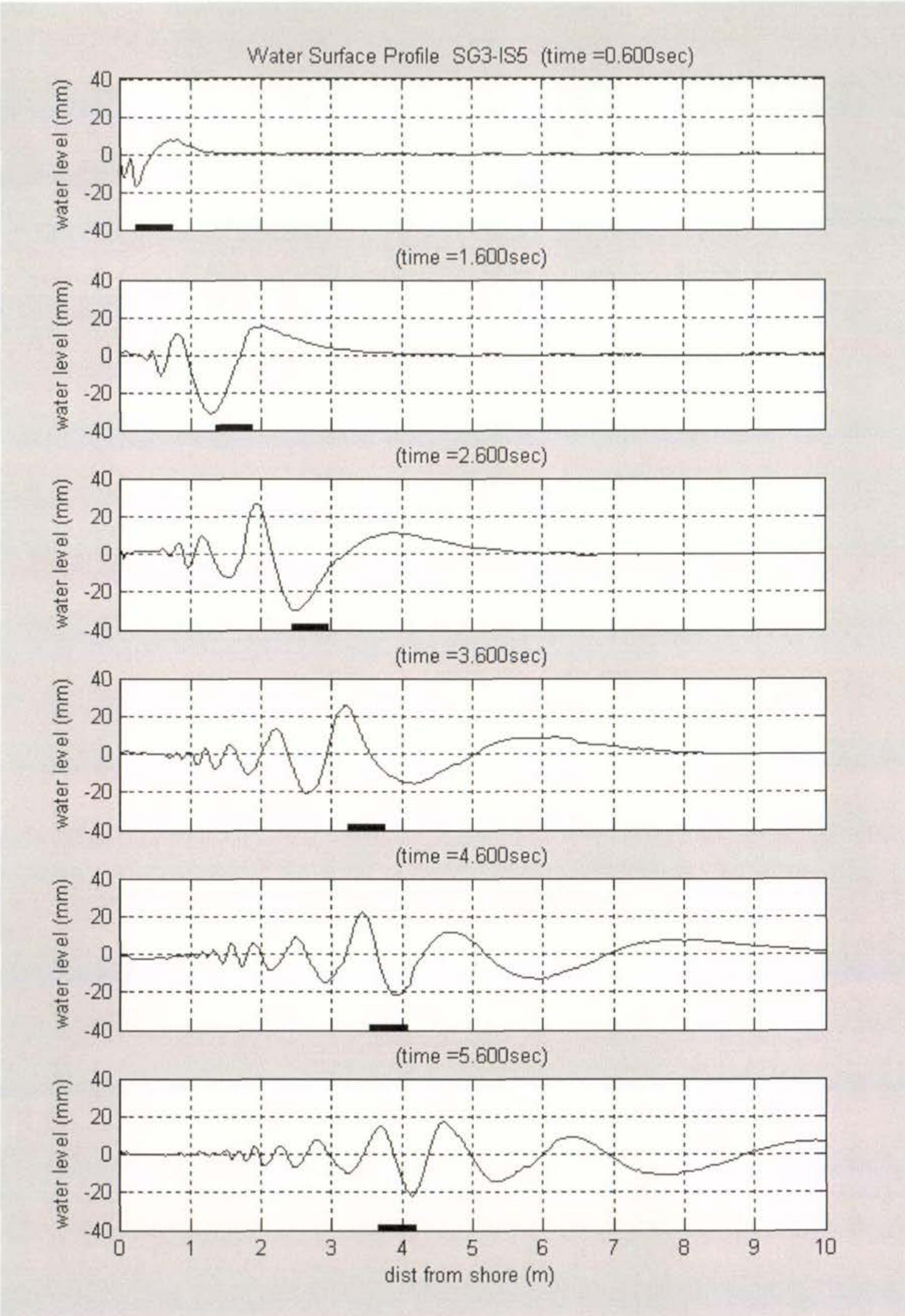

Figure 4.6. Water surface profiles at time = 0.600, 1.600, 2.600, 3.600, 4.600, and 5.600 seconds for SG3_IS5 test. The solid black bars indicate the approximate position of the landslide.

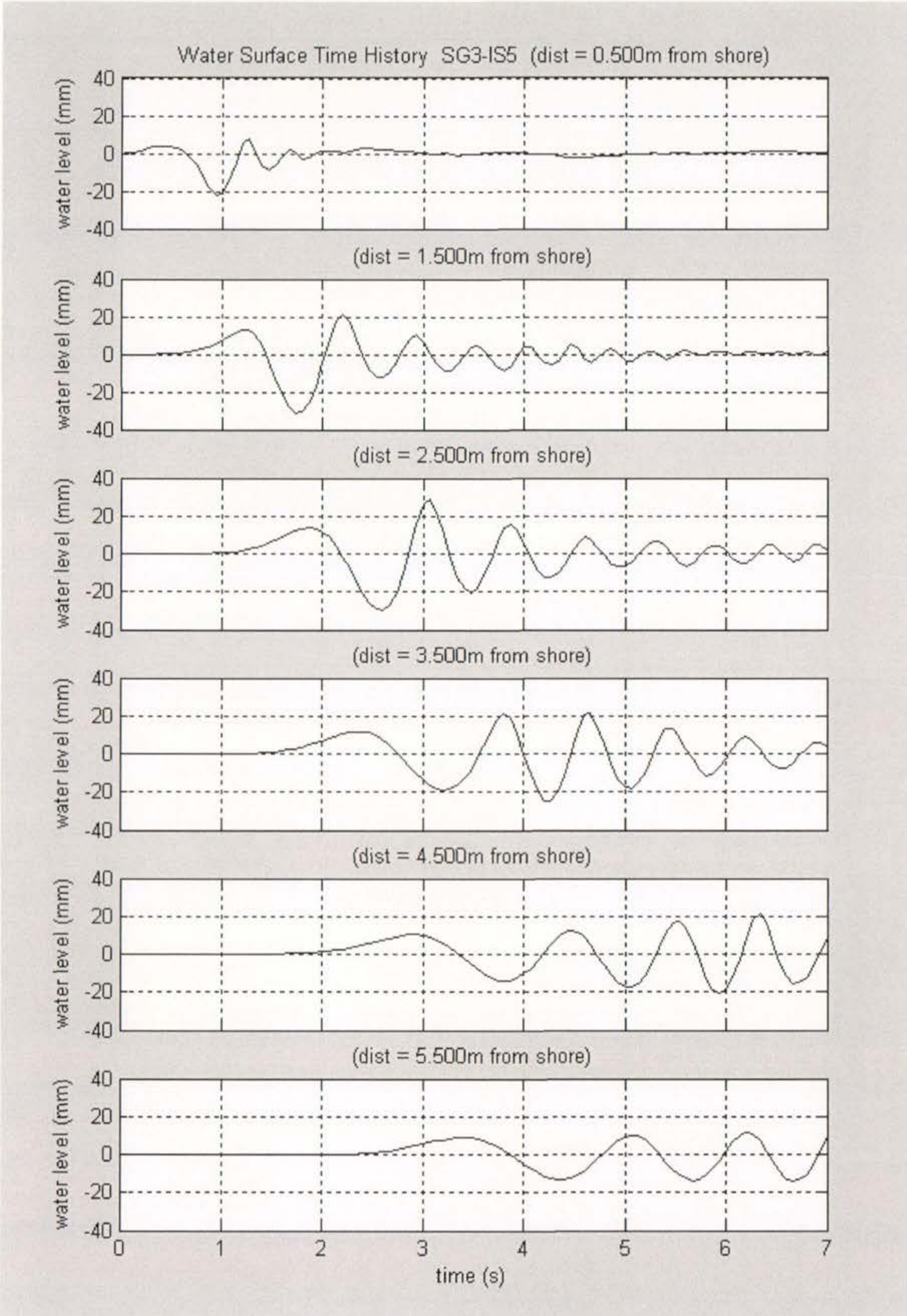

Figure 4.7. Water level time histories at positions 0.500, 1.500, 2.500, 3.500, 4.500, and 5.500 metres from the original shoreline for SG3_IS5 test.

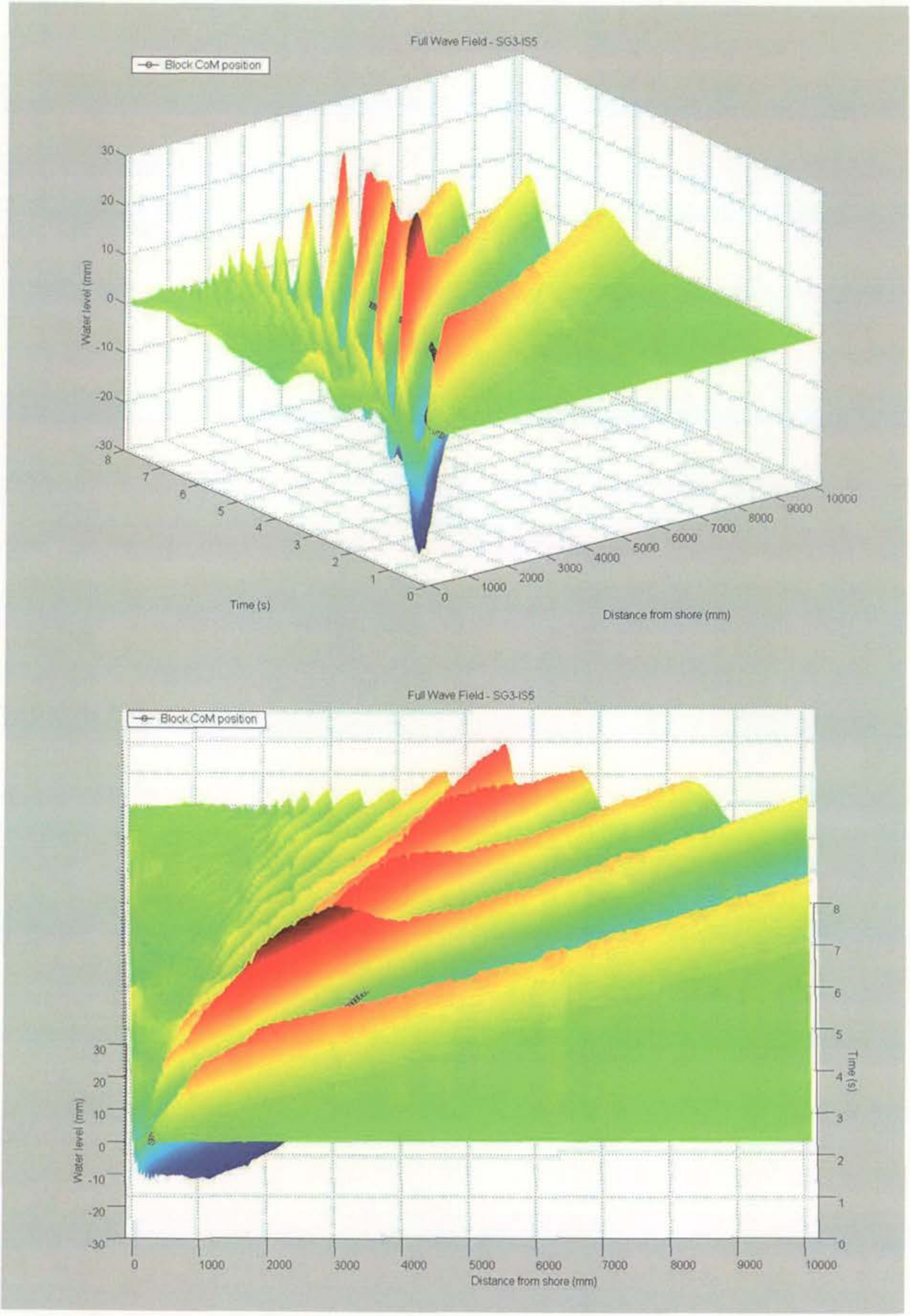

Figure 4.8. Oblique 3-dimensional views of water surface profile time history for the SG3-IS5 test.

Figure 4.9 plots the three-dimensional water level data on a two-dimensional contour plot. In this form the wave propagation speeds are more clearly seen. The wave speeds relative to the landslide are also illustrated. From this plot it can be seen that the 1st crest forms ahead of the landslide centre of mass and the 1st trough forms behind it. The point at which these two waveforms meet follows the landslide centre of mass as it slides down the slope. This phenomenon is observed for all fifteen tests, as shown by Figures A.16-A.30 in the Appendix.

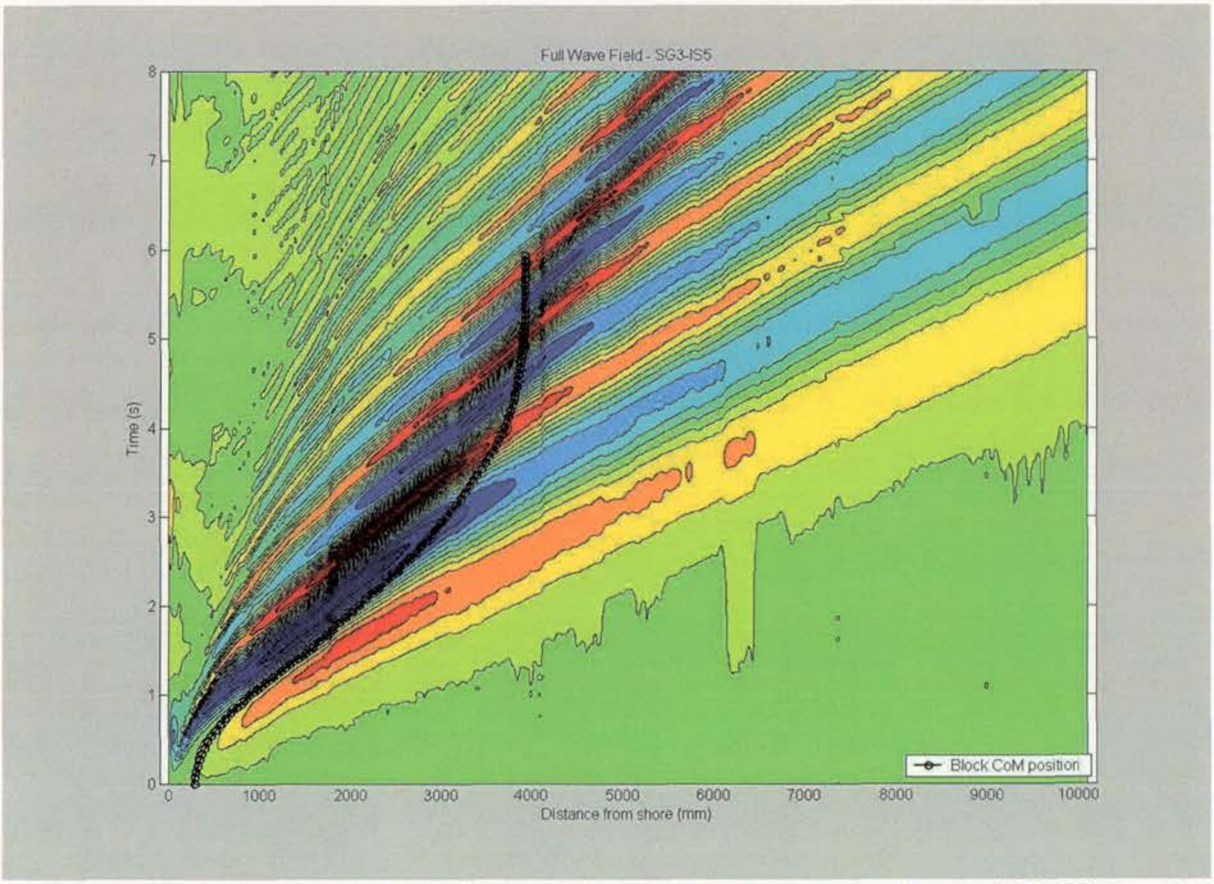

Figure 4.9. 2-dimensional contour plot of water surface profile time history for the SG3-IS5 test. Red colours indicate wave crests and blue colours indicate wave troughs. Note the various wave speeds present within the wave train.

At this point, a qualitative description of the wave generation processes illustrated in two-dimensional contour plots of all fifteen combinations is given. The horizontal motion of the landslide generates the 1st crest as it pushes up the water ahead of it. The acceleration of the surrounding fluid creates a water pressure distribution over the moving landslide. The high pressure ahead of the landslide forces the water surface directly above it up to form the 1st wave crest. This crest is not attached to the landslide and propagates freely once generated.

The accelerating fluid and the turbulent wake above and behind the sliding block creates a region of low pressure. This low pressure pulls the water surface down to form a depression. This wave trough is forced to propagate at the same speed as the accelerating landslide due to the low pressure region being directly connected to the sliding block. The 1st trough is free to propagate once the landslide reached the bottom of the slope and begins to slow. The decrease in velocity of the block disrupts the low pressure region, and its connection with the trough can not be maintained.

Dispersion effects are also present, noticeable as the progressively slower speeds of waves further back in the wave train. The continual generation of waves at the trailing end of the train is also visible. The region of generation of these waves moves downstream over time. As individual waves are generated, their speeds increase as they move into deeper water.

Also noticeable is the weak signal of disturbances propagating upstream of the slider, especially early in the wave generation process. These waves ultimately form the run-up and run-down observed at the shore.

4.3.2 Maximum Wave Crest and Trough Water Levels

Figure 4.10 plots the water level time histories of the 1st crest, 1st trough, and 2nd crest wave peaks for the SG3_IS5 test. The overall maximum/minimum non-dimensional water levels of the individual waves for each specific gravity and initial submergence combination are presented in Figures 4.11, 4.12, and 4.13.

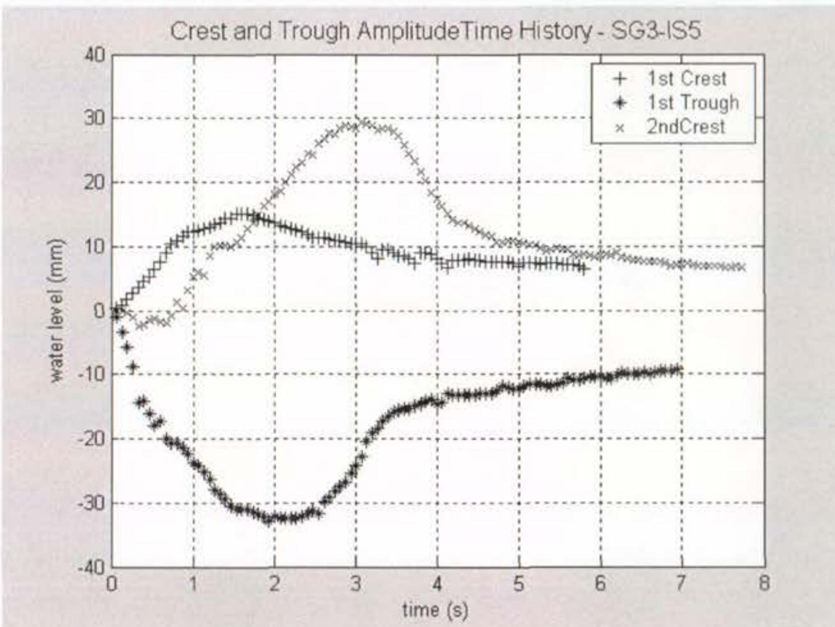

Figure 4.10. Water level time histories for the 1st crest, 1st trough, and 2nd crest for SG3_IS5 test.

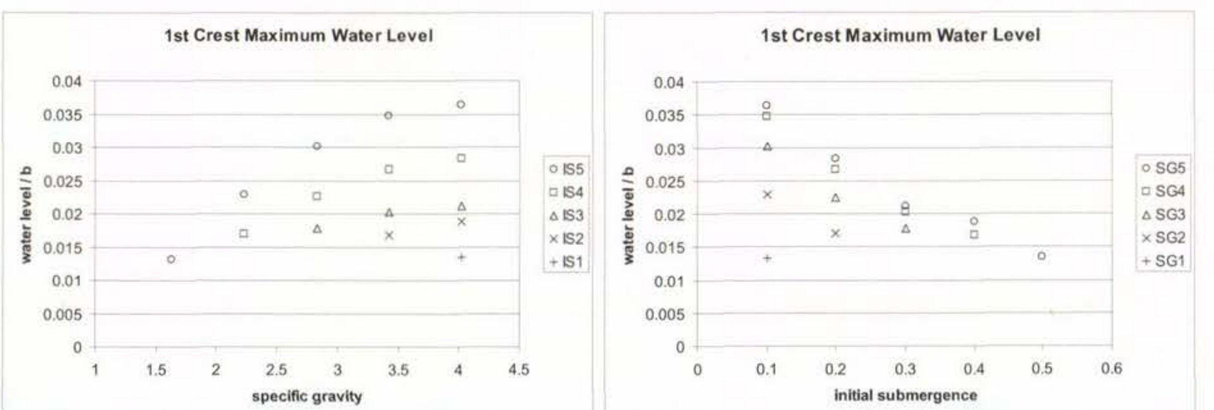

Figure 4.11. Water level of maximum 1st wave crest as functions of specific gravity and initial submergence.

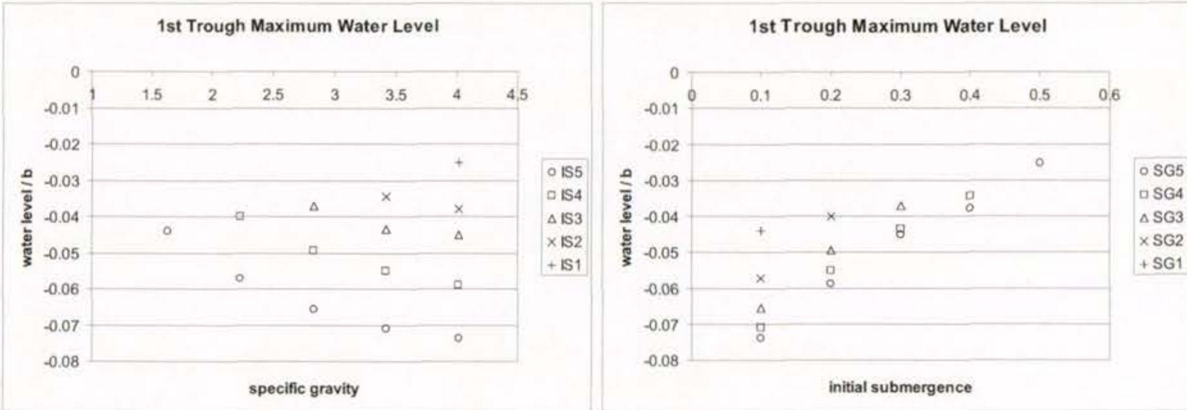

Figure 4.12. Water level of maximum 1st wave trough as functions of specific gravity and initial submergence.

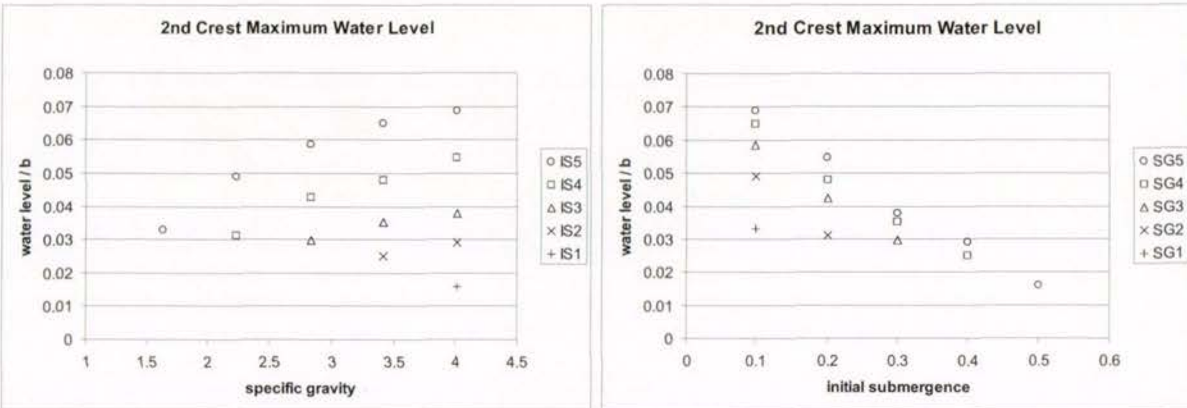

Figure 4.13. Water level of maximum 2nd wave crest as functions of specific gravity and initial submergence.

The overall maximum non-dimensional water levels, of all wave crests, for the fifteen test combinations are presented in Figure 4.14. These plots illustrate the increase in maximum water level with heavier specific gravities and shallower initial submergences.

Figure 4.15 presents data to indicate the non-dimensional downstream position at which the maximum water level occurred. The overall maximum water level occurs further downstream for landslides with heavier specific gravities and shallower initial submergences.

The non-dimensional time at which the overall maximum water level occurs for the fifteen combinations are presented in Figure 4.16. The overall maximum water level occurs later for landslides with heavier specific gravities and shallower initial submergences.

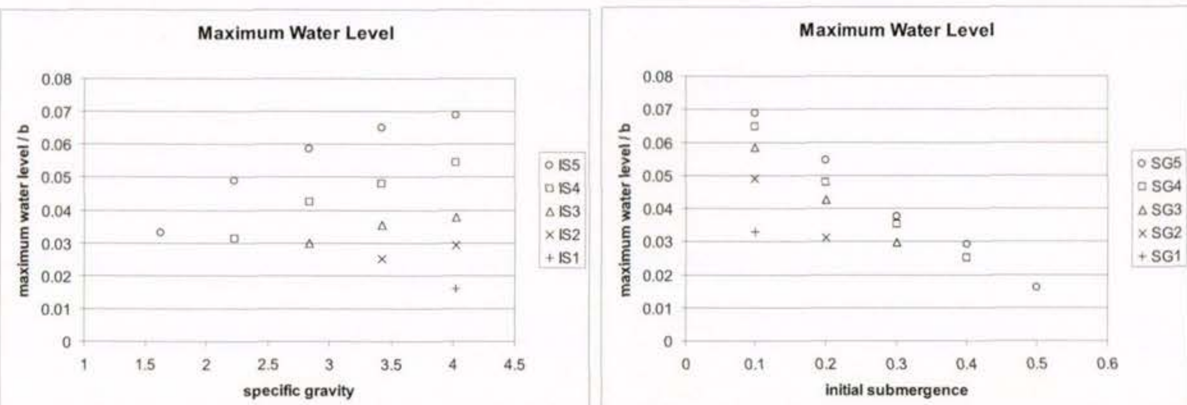

Figure 4.14. Maximum overall water level as functions of specific gravity and initial submergence.

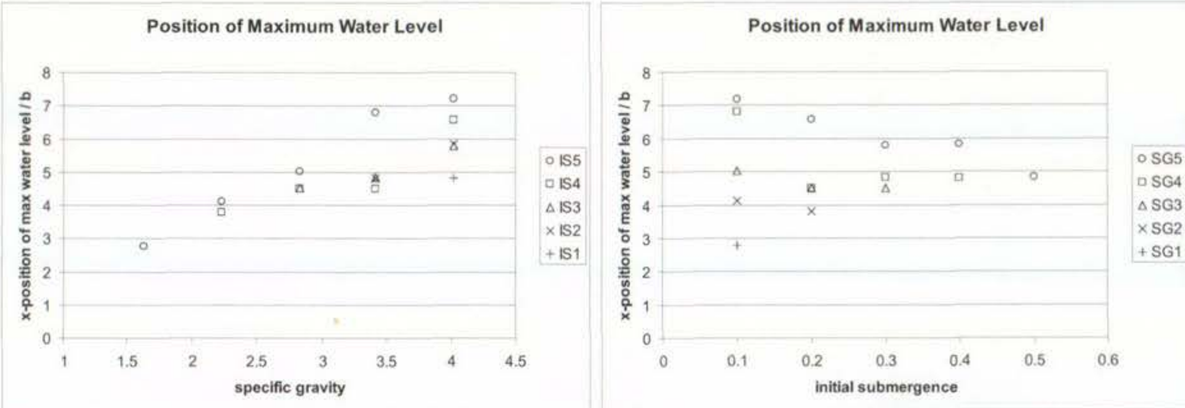

Figure 4.15. Horizontal position of maximum overall water level as functions of specific gravity and initial submergence.

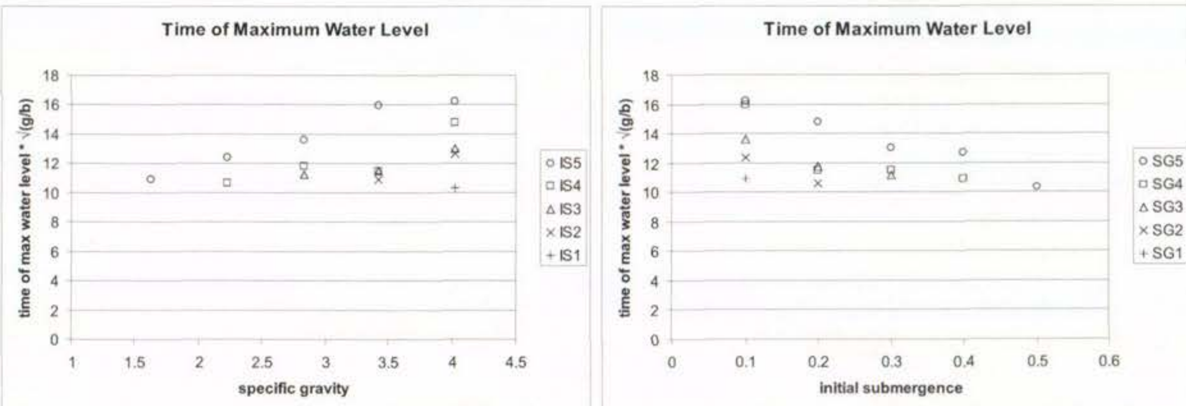

Figure 4.16. Time of occurrence of maximum overall water level as functions of specific gravity and initial submergence.

The overall minimum water levels, of all wave troughs, for the fifteen test combinations are presented in Figure 4.17. This plot illustrates the increase in minimum water level with heavier specific gravities and shallower initial submergences.

The data presented in Figure 4.18 indicates that the position at which the minimum water level occurs tends to be further downstream for landslides with heavier specific gravities.

The time at which the overall minimum water level occurs for the fifteen combinations of specific gravity and initial submergence are presented in Figure 4.19. The overall minimum water level tends to occur slightly later for landslides with heavier specific gravities and shallower initial submergences.

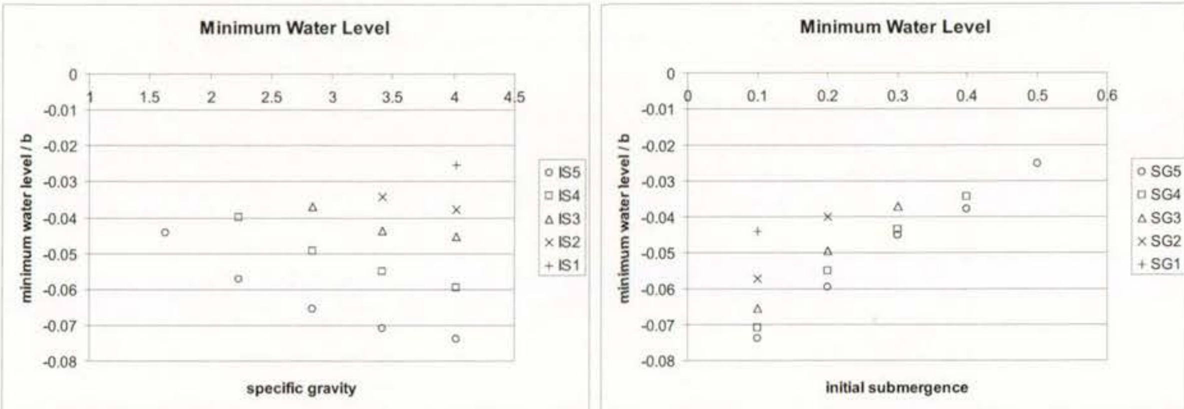

Figure 4.17. Minimum overall water level as functions of specific gravity and initial submergence.

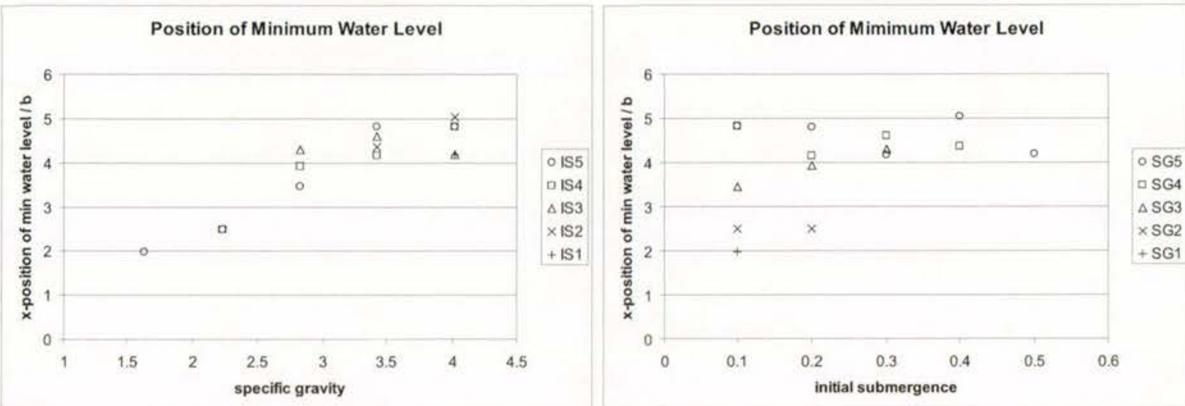

Figure 4.18. Horizontal position of minimum overall positive water level as functions of specific gravity and initial submergence.

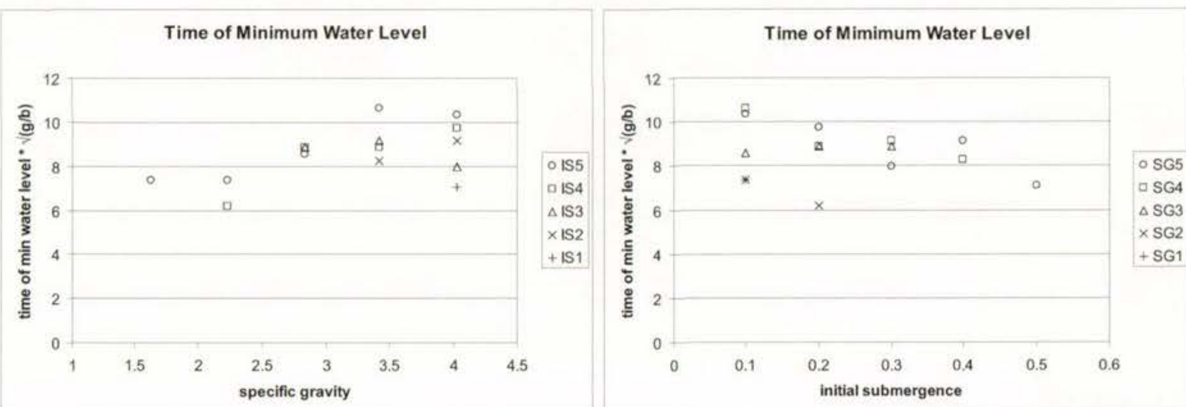

Figure 4.19. Time of occurrence of minimum overall positive water level as functions of specific gravity and initial submergence.

4.3.3 Frequency Domain Analysis

Figure 4.20 plots the fast Fourier transform (FFT) of the water surface profile at seven consecutive times, ranging from zero to 4 seconds, for the SG3_IS5 combination. The 1st wave crest begins to propagate out of the observed domain after approximately 4 seconds for all fifteen tests. The FFT of a water surface profile provides an indication of the dominant wavelengths in the water surface record. Wavelengths in this figure have been normalised by the landslide length. The features of the FFT from this test are also present in the other specific gravity and initial submergence combinations. The results of this FFT quantify the trends observed in Figure 4.6.

Inspecting Figure 4.20, it can be seen that as time progresses energy is gradually transferred from the shorter wavelengths into the longer wavelengths. However, some energy remains invested in the short wavelengths of the trailing wave packet. Note the absence of waves with lengths shorter than 1 non-dimensional wavelength. The increase in total energy as time progresses is evident.

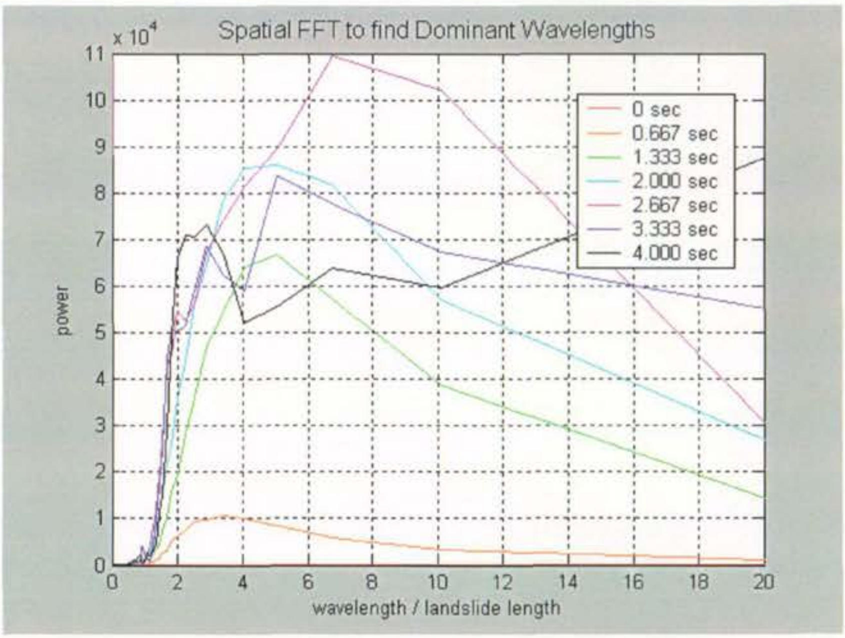

Figure 4.20. Fast Fourier transform of the water surface profiles at 0, 0.667, 1.333, 2.000, 2.667, 3.333, and 4.000 seconds to find the dominant wavelengths for the SG3_IS5 test. Wavelengths have been non-dimensionalised by the landslide length. Note the increasing dominance of the longer non-dimensional wavelengths at later times.

4.3.4 Maximum Wave Run-up and Run-down

Wave run-up and run-down heights along the slope were measured vertically from the original still water level. The run-up and run-down lengths, the horizontal distance from the original intersection of the water and the slope surfaces, can be calculated from the geometry.

A typical wave run-up/down height time history is presented in Figure 4.21 for test SG3_IS5. The key features of this time history, and of those for other specific gravity and initial submergence combinations, is the large initial draw-down followed by a rebound to a level close to the original water level. This is followed by a positive run-up and relaxation back to something close to the original mean water level.

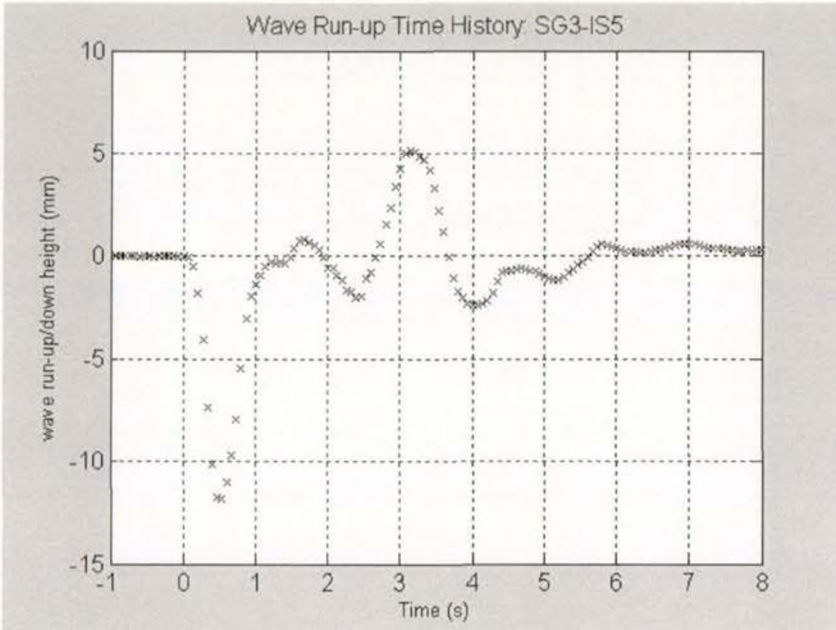

Figure 4.21. Wave run-up/down height time history for the SG3_IS5 test.

The trends observed in maximum non-dimensional wave run-up data presented in Figure 4.22 indicate that the maximum wave run-up heights increase for heavier specific gravities and shallower initial submergences. It is theorised that the positive run-up peak occurs as a result of a wave generated by the short duration, but high magnitude, deceleration of the landslide upon reaching the base of the slope. The wave generated at this point and time propagates upstream and runs up the slope.

Preliminary tests with the landslide block tethered so that it abruptly stopped at the base of the slope, resulted in the generation of waves with amplitudes larger than those initially generated by the accelerating landslide. The removal of the tether and allowing the landslide to slow naturally along the flume floor resulted in a significant reduction in the magnitude of the wave generated by the slowing block. However, the maximum positive run-up height was still dominated by the run-up of this landslide deceleration-induced wave. This indicates that landslide deceleration can have a significant affect on the magnitudes of the observed wave run-up

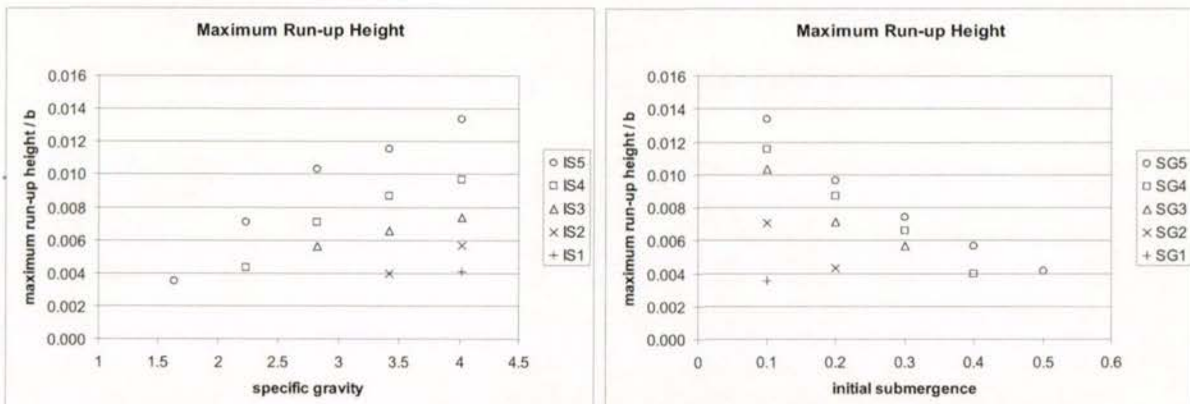

Figure 4.22. Maximum wave run-up height as functions of specific gravity and initial submergence.

As illustrated in Figure 4.5, the magnitude of the maximum deceleration increases with increasing specific gravity and shallower initial submergences. The higher specific gravities induce higher accelerations and the shallow submergences increases the duration of acceleration, allowing higher landslide velocities to be reached at the base of the slope. To provide further evidence of the landslide deceleration origins of the run-up height observed, Figure 4.23 plots maximum non-dimensional wave run-up heights against maximum non-dimensional landslide velocities and decelerations at the base of the slope. The data from all fifteen combinations collapses onto one curve when the maximum velocity is used as the independent variable. The same occurs when the maximum deceleration is used as the independent variable. However, the reduced accuracy of the deceleration values induces greater spread in the data.

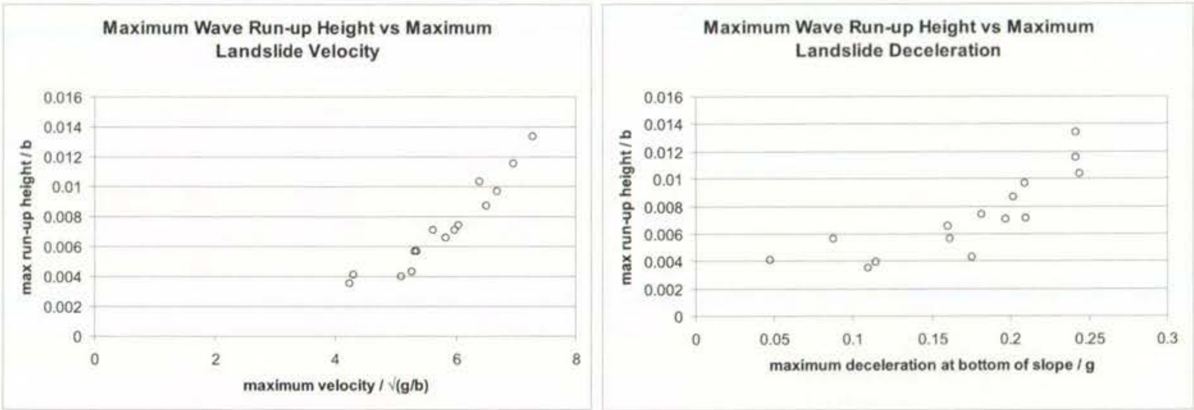

Figure 4.23. Maximum wave run-up height versus maximum landslide velocity and maximum landslide deceleration at the base of the slope.

Figure 4.24 indicates that the non-dimensional time of maximum run-up occurs earlier for higher specific gravities and deeper initial submergences. The added mass and shorter slope distances cause the landslide to reach the base of the slope earlier. As the run-up peak is created by the deceleration of the block at toe of the slope, the maximum run-up occurs earlier.

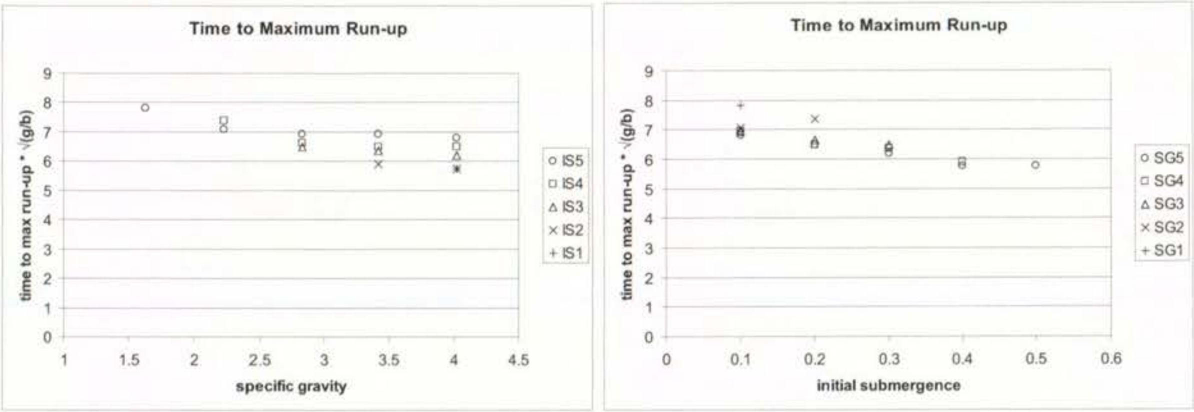

Figure 4.24. Time of occurrence of maximum wave run-up height as functions of specific gravity and initial submergence.

Based on the theory that the large wave run-up was caused by the landslide deceleration at the base of the slope, the travel time for a wave generated above the toe of the slope to travel back to the beach was calculated. A wavelength of 0.5 m, equal to the length of the landslide, was assumed and the time for this wave to propagate upstream to the shore was added to the time for the landslide to reach the base of the slope. These times were calculated for all fifteen test combinations are plotted in Figure 4.25. They are similar to the measured times of maximum wave run-up.

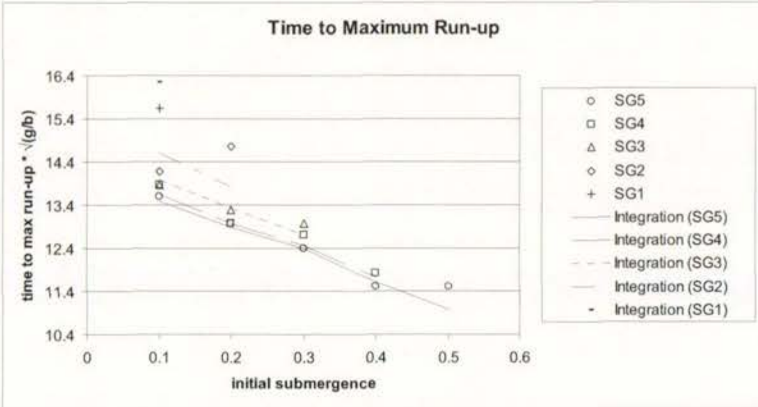

Figure 4.25. Comparison of measured time of occurrence of maximum wave run-up with calculated values assuming a 0.5m wavelength crest was generated above the toe of the slope and propagated upstream.

The non-dimensional wave run-down observed at the shore decreases with lighter specific gravities and deeper initial submergences, as shown in Figure 4.26. The wave run-down and the 1st wave trough are formed by the same mechanism, namely the initial draw-down of the water surface above the landslide. The depression that forms over the rear end of the block propagates in both the upstream direction, to cause the large initial draw-down at the shoreline, and downstream as the 1st wave trough. The magnitudes of these two parameters are governed by the strength of this initial water surface depression. The correlation between the maximum run-down height and the maximum 1st wave trough amplitude, as shown in Figure 4.27, tends to confirm the common origin of these two phenomena.

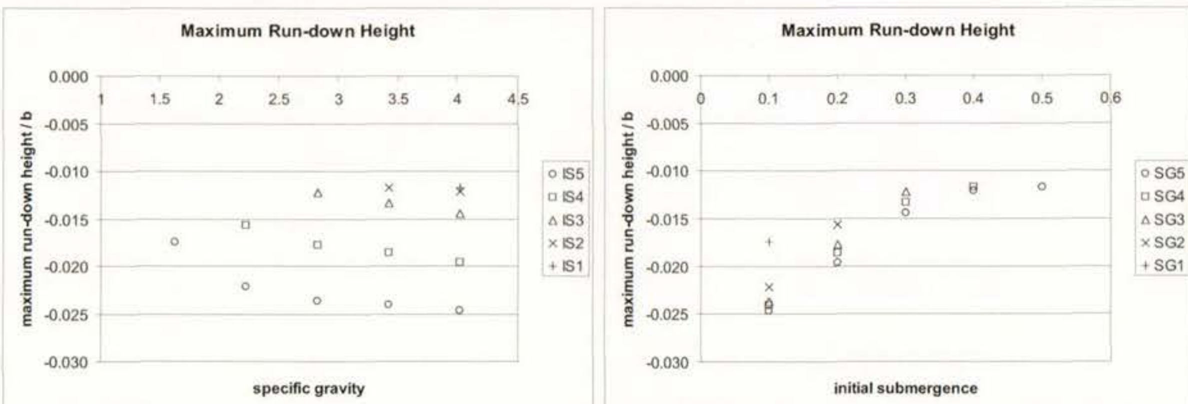

Figure 4.26. Maximum wave run-down height as functions of specific gravity and initial submergence.

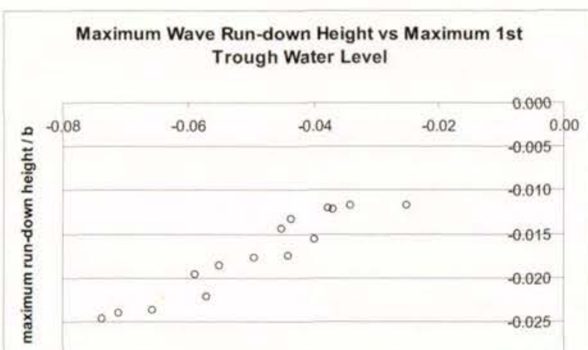

Figure 4.27. Maximum 1st trough wave amplitude versus maximum wave run-down height.

As shown in Figure 4.28, the non-dimensional time the maximum wave run-down occurs is independent of specific gravity, dependent solely on the initial submergence of the landslide. The maximum run-down occurs later for deeper submergences because the landslide is initially further downstream, and the initial water surface depression that forms over the landslide has further to travel upstream.

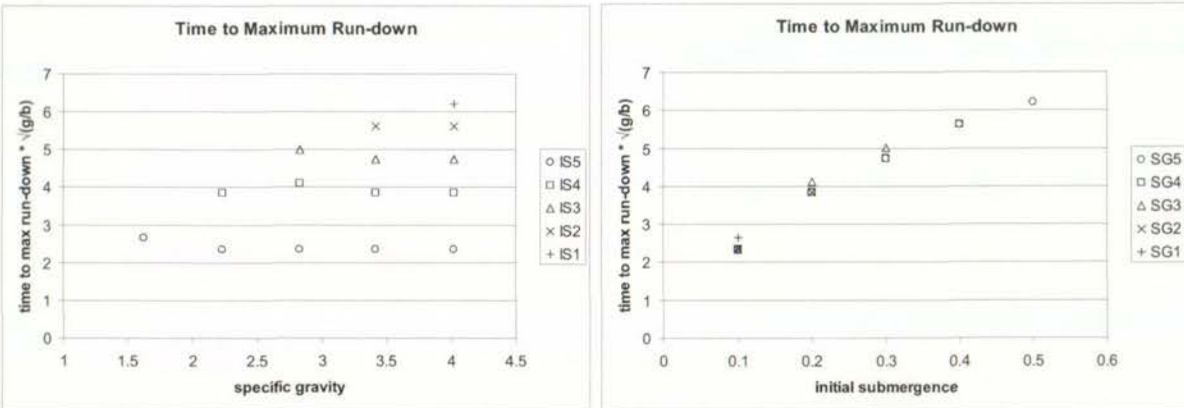

Figure 4.28. Time of occurrence of maximum wave run-down height as functions of specific gravity and initial submergence.

An approximate time of occurrence of maximum wave run-down was calculated and compared with the measured values, as shown in Figure 4.29. Wave troughs with lengths of 0.4m, 0.5m and 0.6m, approximately the length of the landslide, were hypothetically generated at various downstream positions and propagated upstream towards the shore. These propagation times for the three different wavelengths are plotted in Figure 4.29 as a function of initial submergence.

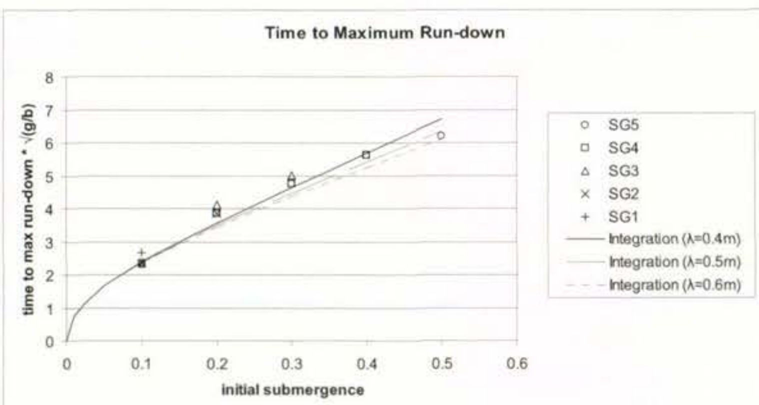

Figure 4.29. Comparison of measured time of occurrence of maximum wave run-down with calculated values assuming a specific wavelength trough was generated above the initial landslide position and propagated upstream.

4.3.5 Energy

The instantaneous potential energy contained in the waves was calculated as

$$\text{wave } \mathrm{E_p(t)} = \frac{1}{2}\rho_o g w \int_0^\infty \eta(t)^2 \, dx \qquad \textbf{(4.7)}$$

where ρ_o = water density

g = acceleration of gravity

w = flume/landslide width

η = water level

x = downstream position

t = time

The wave potential energy integration limits were actually between zero and 10.1 m downstream. However, provided waves had not propagated out of our observed domain and the water surface beyond 10.1 m was still, the integration of η^2 between zero and infinity was still valid.

The instantaneous landslide kinetic energy was calculated as

$$\text{block } \mathrm{E_k(t)} = \frac{1}{2} m_b vel(t)^2 \qquad \textbf{(4.8)}$$

where m_b = unsubmerged landslide mass

vel = landslide velocity

The instantaneous landslide potential energy is calculated by multiplying the submerged mass of the landslide by the vertical fall distance relative to its initial position, and was calculated as

$$\text{block } \mathrm{E_p(t)} = (m_b - m_0)(y(t_0) - y(t)) \qquad \textbf{(4.9)}$$

where m_0 = mass of water displaced by landslide

$y(t_0)$ = initial landslide vertical position

$y(t)$ = instantaneous landslide vertical position

Figure 4.30 plots the time histories of wave potential energy, landslide kinetic energy, and the change in landslide potential energy, for the SG3_IS5 test. The key features of this plot are similar for the other combinations of specific gravity and initial submergence. Some of the block potential energy is converted into kinetic energy of the block as it slides down the slope. The remaining potential energy is dissipated as friction on the sliding surface. The motion of the landslide sets in motion some of the surrounding fluid, converting some of the block kinetic energy into kinetic energy of the water. Some of the energy in the water motions is then passed into the wave potential energy, the remainder being dissipated through friction.

It is noticed that the maximum wave potential energy occurs after the block kinetic energy peak. It is speculated that this is due to the finite time required for the energy to pass from the landslide into the fluid motions and then into the waves. Note that wave potential energy decreases after approximately 4 seconds due to the propagation of energy out of the observed region. The maximum landslide kinetic energy occurs before the time of maximum landslide potential energy conversion because the block has started to slow before reaching the floor of the flume, at the slope-to-flume floor transition.

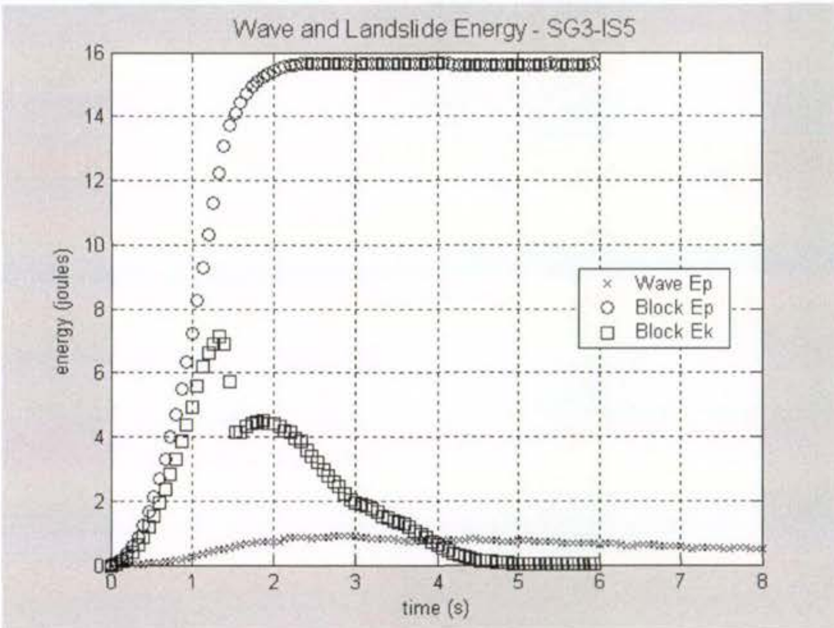

Figure 4.30. Time histories of wave potential energy (wave Ep), landslide kinetic energy (block Ek), and landslide potential energy converted (block Ep), for the SG3_IS5 test.

Figure 4.31 illustrates the non-linear reduction in maximum wave potential energy with decreasing specific gravity and deepening initial submergence.

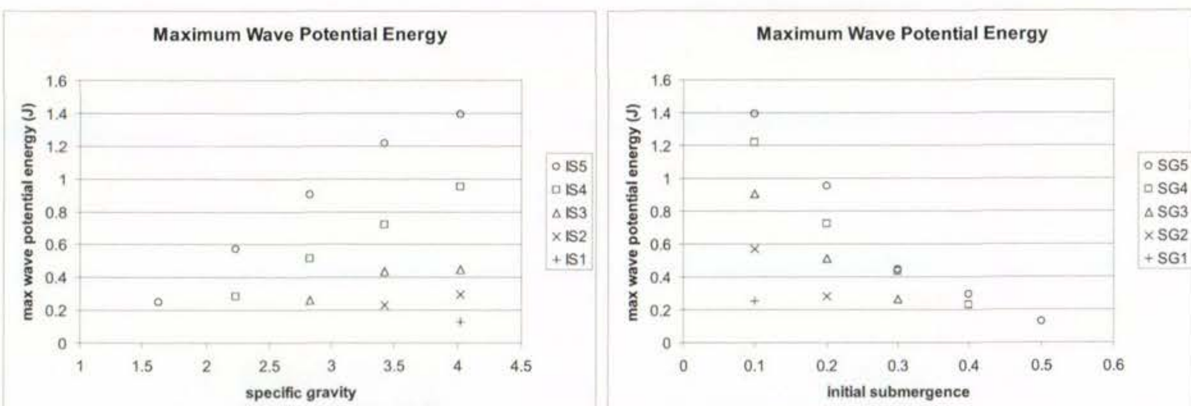

Figure 4.31. Maximum wave potential energy as functions of specific gravity and initial submergence.

The expression for landslide kinetic energy shown in Equation 4.8 defines a linear dependence on mass and a quadratic dependence on velocity of the landslide. The plot in Figure 4.2 indicates a non-linear relationship between velocity and mass. Figure 4.32 highlights the reduction in maximum landslide kinetic energy with decreasing specific gravity and deepening initial submergence.

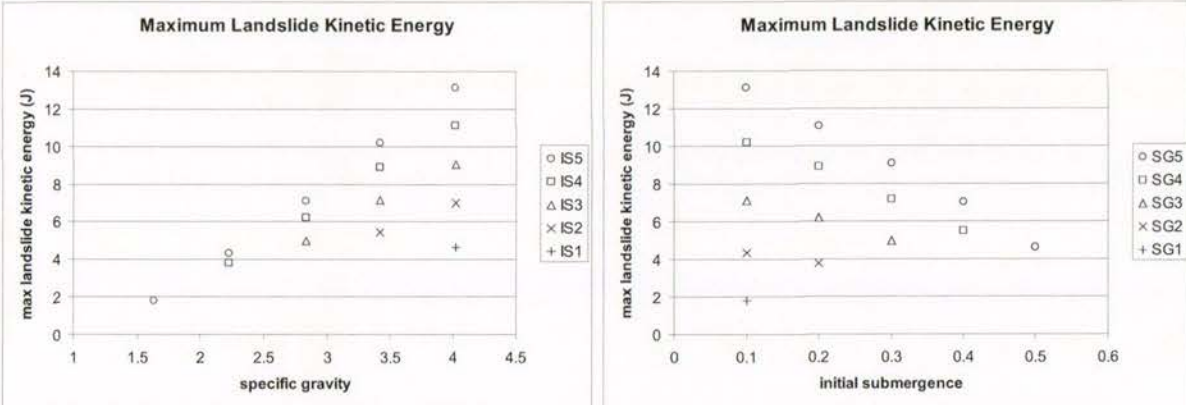

Figure 4.32. Maximum landslide kinetic energy as functions of specific gravity and initial submergence.

The expression for landslide potential energy conversion shown in Equation 4.9 defines a linear dependence on mass and change in height of landslide. Figure 4.33 illustrates the linear reduction in maximum landslide potential energy conversion with decreasing specific gravity and deepening initial submergence.

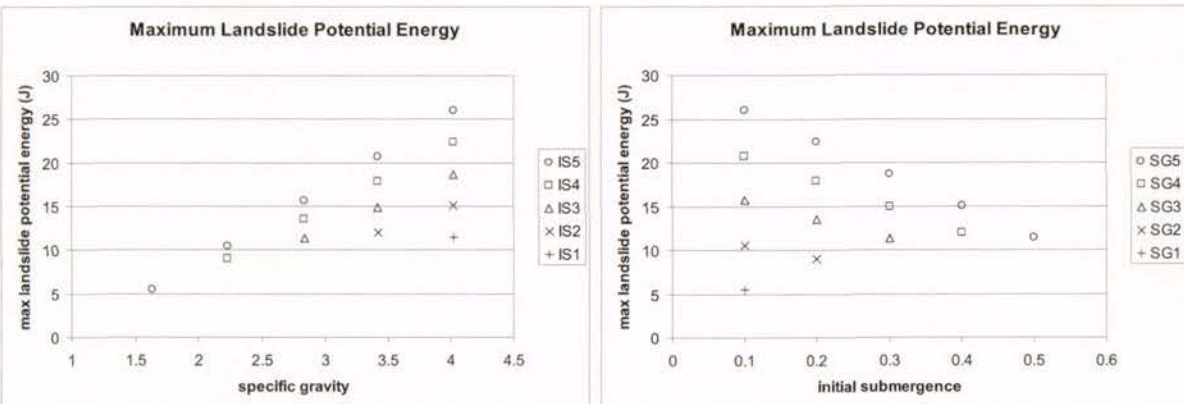

Figure 4.33. Maximum landslide potential energy as functions of specific gravity and initial submergence.

The values presented in Figure 4.34 indicate the maximum conversion of landslide kinetic energy into wave potential energy is between 2.8% and 13.8%. Shallow initial submergences and lighter specific gravities increase the efficiency with which landslide kinetic energy is converted into wave potential energy. Watts (1997) found conversion rates of solid block kinetic energy into wave potential energy of between 3% and 7%. However, his expression for energy conversion was calculated as a function of the landslide terminal velocity and the square of the maximum wave amplitude.

The maximum conversion of landslide potential energy into wave potential energy is presented in Figure 4.35. Conversion rates range between 1.1% and 5.9%, and are greater for shallower initial submergences. The effect of increasing specific gravity is relatively weaker. Weigel (1955) found typical rates of 1-2% for conversion of landslide potential energy into wave potential energy. His wave potential energies were calculated as a function of the sum of the 1^{st} wave trough and 2^{nd} wave crest amplitudes, squared.

The percentage conversion of potential energy into kinetic energy of the landslide ranges between 32.9% and 50.4%, as shown in Figure 4.36. The efficiency of conversion is strongly influenced by changes in specific gravity, with efficiency increasing for heavier landslides. The increase in energy conversion with shallower initial submergences is relatively weak.

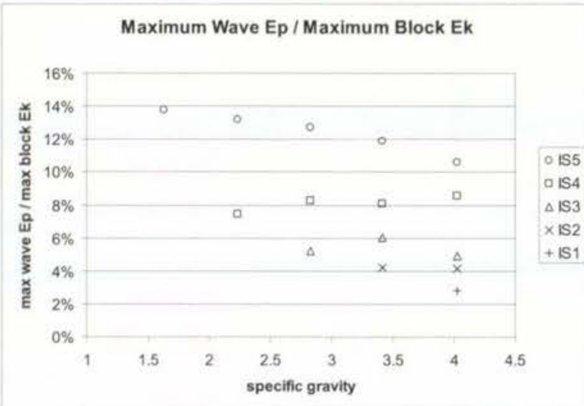

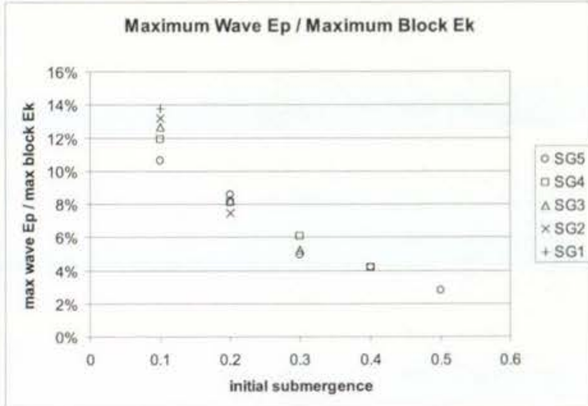

Figure 4.34. Percentage conversion of maximum landslide kinetic energy into wave potential energy

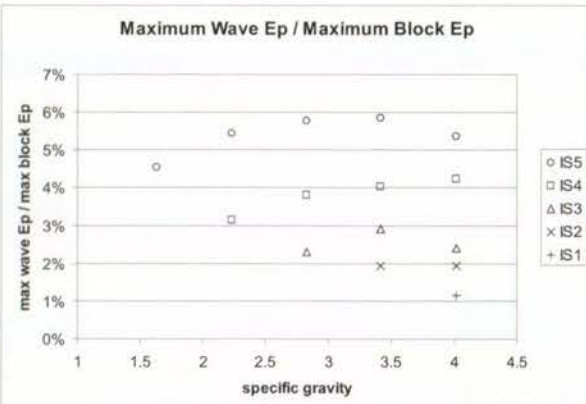

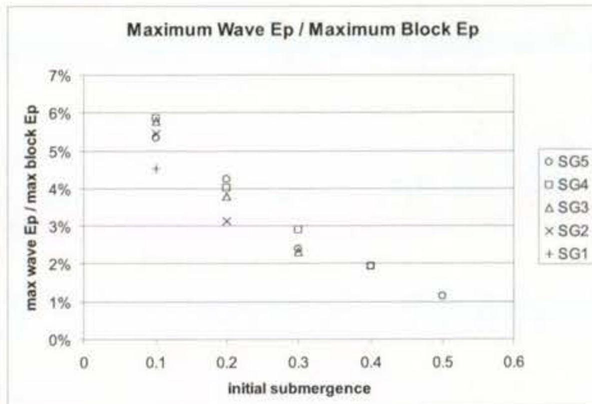

Figure 4.35. Percentage conversion of maximum landslide potential energy into wave potential energy

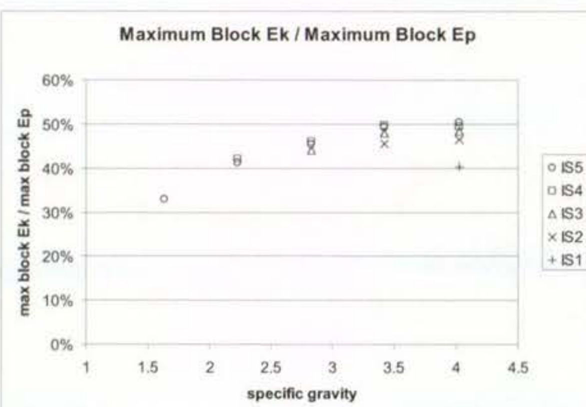

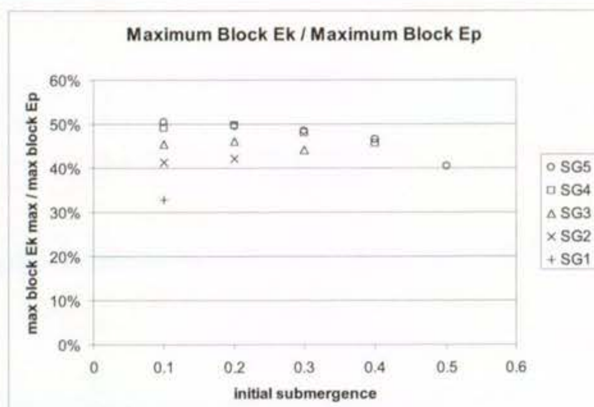

Figure 4.36. Percentage conversion of maximum landslide potential energy into landslide potential energy

4.4 Sub-surface Velocities

Figures 4.37, 4.38, and 4.39 present sub-surface velocity fields, generated from the PTV experiment for the SG1_IS5 test, at a region at the base of the slope. These images cover the water column from 0.030 m above the still water level to 0.370 m below, and span from 0.793 m to 1.193 m downstream. Due to the unreliable PTV matches at the water surface, the velocities within the waves are not shown. The fine white lines in these figures are instantaneous streamlines and the bold line is the slope surface.

At time = 0.733 seconds in Figure 4.37, the landslide is approaching the image diagonally downwards from the left, as indicated by the arrow. This velocity field illustrates the motion of the water outwards and upwards ahead of the landslide. The high water pressures in front of the landslide pushes the water up towards the surface to form the 1st crest.

Figure 4.38 illustrates the acceleration of the fluid as the block slides past at time = 1.533 seconds. Fluid in front is forced up and over the landslide. The high velocities above the landslide create low pressures that draw down the water surface to form the 1st trough.

With the landslide having moved out to the right of frame, a series of rotating eddies are left behind, as shown in Figure 4.39 at time = 5.600 seconds. The flow immediately above the slope surface tends to follow the landslide down-slope. For continuity of mass, the water in the upper region of the water column gently flows upstream.

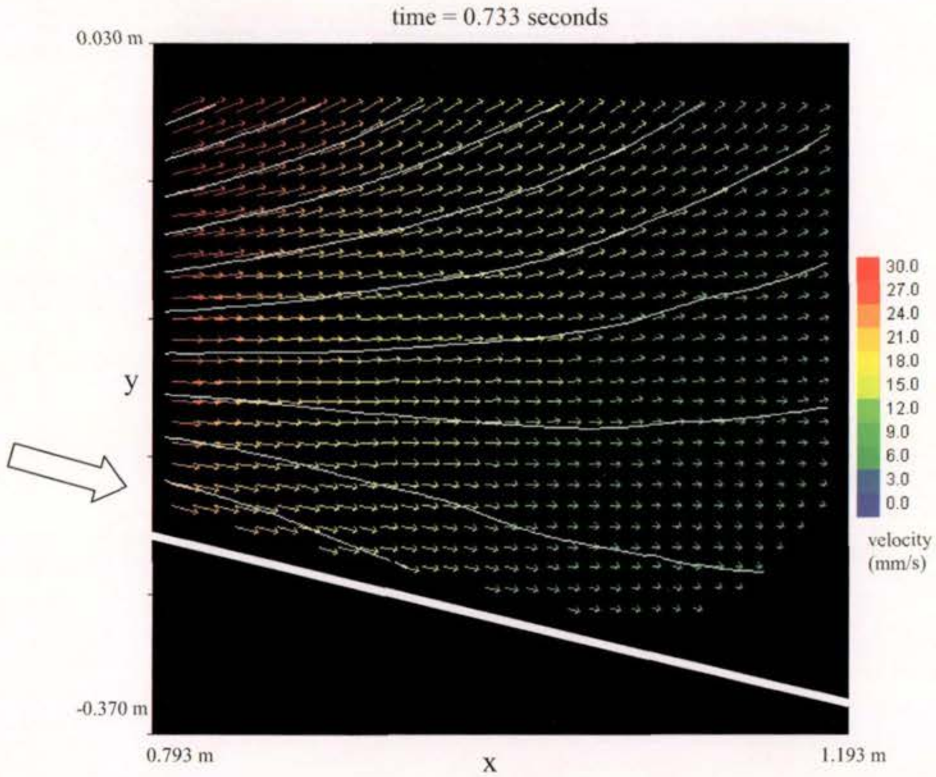

Figure 4.37. Sub-surface velocity field, for the SG1_IS5 test, of a region at the base of the slope from .0793-1.193 m downstream. Instantaneous streamlines are indicated by the white lines. The image is taken at time = 0.733 s with the landslide approaching the frame diagonally from the left of frame, as indicated by the arrow.

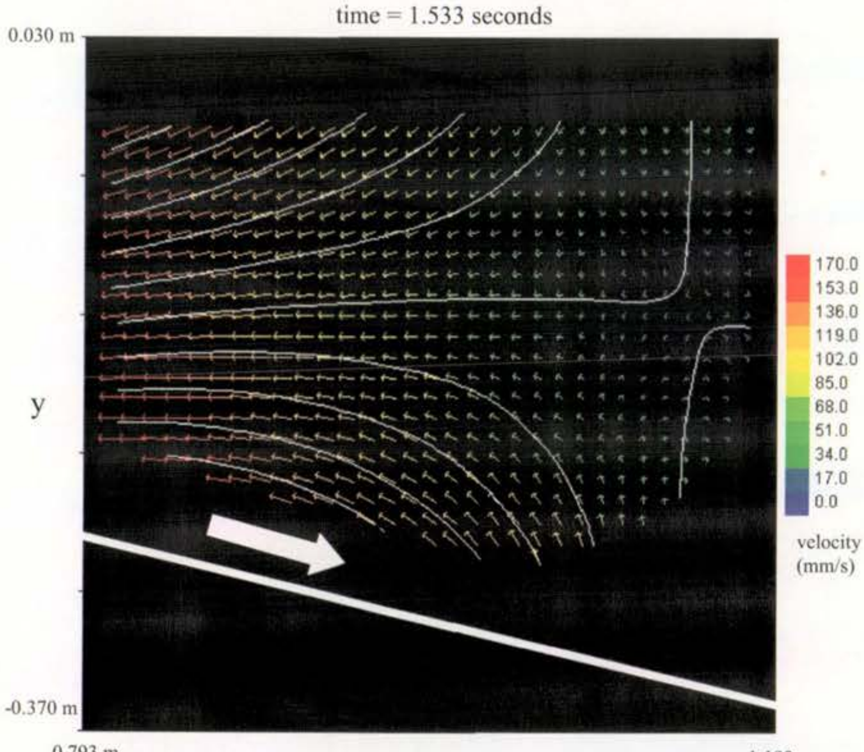

Figure 4.38. Sub-surface velocity field, for the SG1_IS5 test, of a region at the base of the slope from .0793-1.193 m downstream. Instantaneous streamlines are indicated by the white lines. The image is taken at time = 1.533 s with the landslide moving across the frame diagonally from the left of frame, as indicated by the arrow.

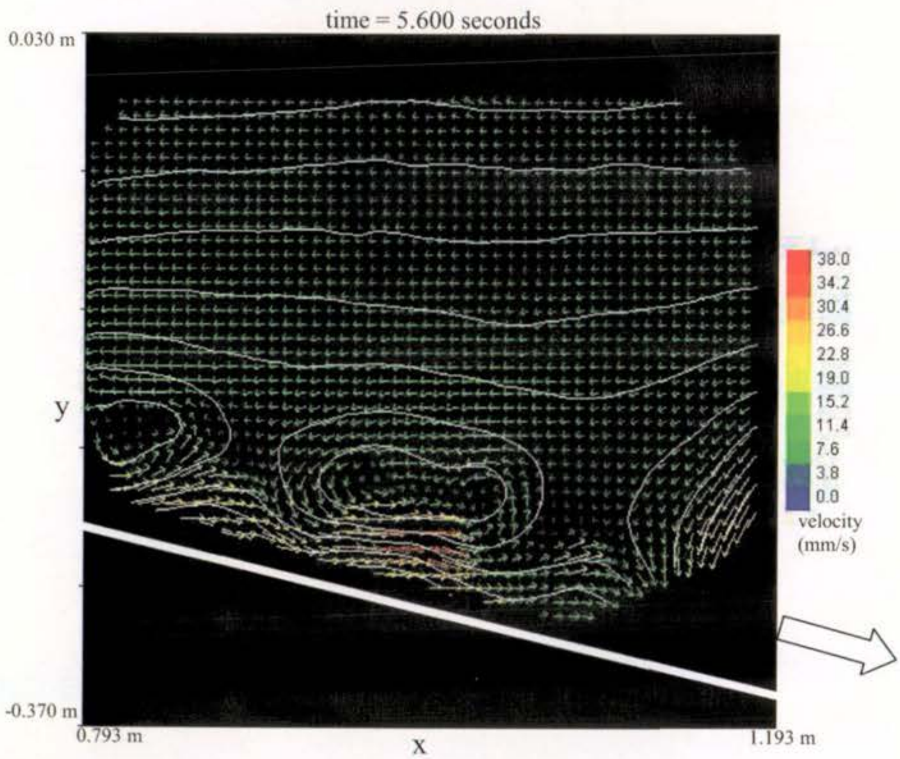

Figure 4.39. Sub-surface velocity field, for the SG1_IS5 test, of a region at the base of the slope from .0793-1.193 m downstream. Instantaneous streamlines are indicated by the white lines. The image is taken at time = 5.600 s with the landslide having moved out of frame towards the right, as indicated by the arrow.

Figure 4.40 is a sub-surface velocity field generated from the PTV experiment for the SG1_IS5 test, at a region downstream of the final resting place of the landslide. This image is actually made up from the combination of velocity fields from the upper and lower camera positions. This velocity field is taken at a time 6.534 seconds after landslide release and covers the entire water column from the still water level to the flume floor, and spans from 6.828 m to 7.228 m downstream. In this image, a wave crest has moved across the water surface towards the right. A wave trough is approaching from the left that is causing the downward water motions.

Figure 4.41 shows the horizontal and vertical velocity time history for the SG1_IS5 test at a point 7.000 m downstream and 0.219 m below the free surface. The horizontal velocities precede the vertical velocities by $\pi/2$ radians, as also shown by the clockwise particle orbits in Figure 3.17.

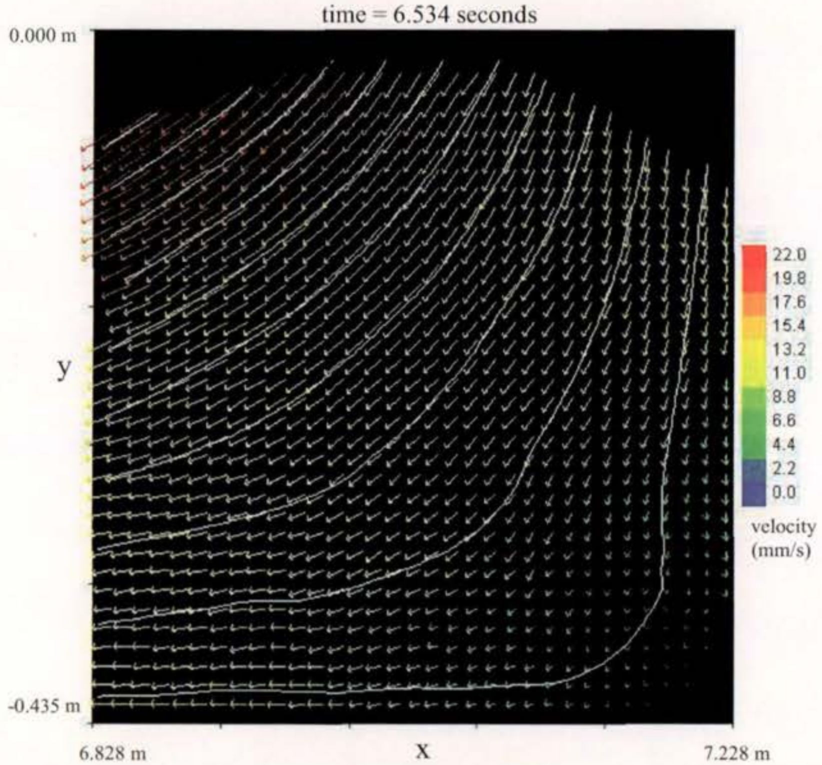

Figure 4.40. Sub-surface velocity field, for the SG1_IS5 test, of the entire water column for a region from 6.828-7.228 m downstream Instantaneous streamlines are indicated by the white lines.

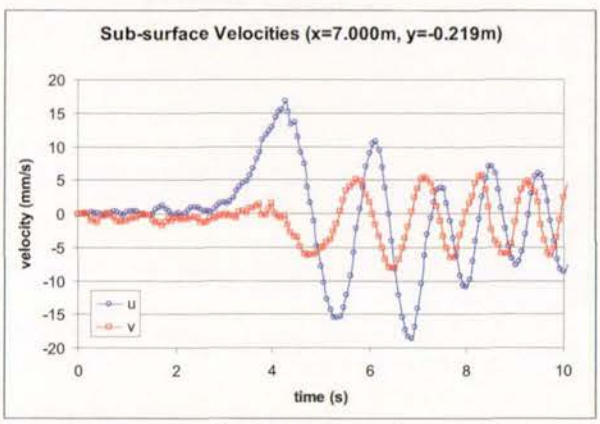

Figure 4.41. Horizontal and vertical velocity time history for the SG1_IS5 test at a point 7.000 m downstream and 0.219 m below the free surface.

Chapter 5: Conclusions

The focus of this research was to generate underwater landslide-induced tsunami water level data of sufficient quality for comprehensive verification of numerical model results. The use of electrical point gauges, such as resistance and capacitance wave gauges, in earlier research could only provide limited data about the generation and evolution of waves due to their very limited spatial coverage.

Depending on the complexity of the numerical model used, many parameters pertaining to underwater landslides can be calculated. These include such things as water surface levels, wave and run-up heights, and sub-surface velocity and pressure fields. The landslide characteristics input into these models include position time history, volume, density/mass, shape, deformability, and slope geometry.

The experiments carried out here were for a prismatic semi-elliptical block sliding in water 0.435 m deep, along a 15° slope. Techniques utilising LIF and PTV were used to measure the landslide kinematics, water surface profile time histories, and sub-surface velocity profiles for fifteen combinations of landslide specific gravity and initial submergence. Rigorous controls were implemented to ensure the repeatability of these tests. The LIF technique developed to measure the spatial and temporal evolution of the water surface was found to produce results with resolution and accuracy comparable to those of traditional electrical point wave gauges.

The measurement of full water surface profile time histories proved advantageous for closely observing and quantifying the initial generation and propagation of laboratory tsunami waves. By comparing the instantaneous position and speed of the landslide relative to the wave field, it was found that the 1st crest formed over the front half of the landslide and a trough formed over the rear. The point at which these two waves met was centred above the landslide centre of mass and remained there as the block slid down the slope.

By observing the water surface profile time histories and the FFT results, the wavelength components of the wave field could be assessed at various times. It was noticed that the wavelengths of individual waves would increase as they propagated. This was due to the waves entering deeper water. The FFT results also indicated the absence of waves with lengths less than the landslide length.

The dispersion of the waves was evident, as waves further behind in the wave train propagated more slowly than those in front. New waves were continually generated at the trailing end of the wave train.

The ability to resolve water levels spatially and temporally allowed wave potential energy time histories to be calculated. It was observed that the time of occurrence of maximum wave potential energy was later than that for the maximum landslide kinetic energy. It was speculated that this was because a finite time was required for the landslide kinetic energy to transfer into water kinetic energy and eventually into wave potential energy. Conversion efficiencies ranged from 32.9%-50.4% for landslide potential energy into landslide kinetic energy. Rates for conversion between landslide kinetic energy and wave potential energy ranged between 2.8% and 13.8%.

The wave trough initially generated above the rear end of the landslide propagated in both upstream and downstream directions. The upstream-travelling trough was found to cause the large initial draw-down at the shore. The magnitude of the maximum run-down was directly related to the maximum downstream-propagating 1st wave trough amplitude. The maximum wave run-up height observed at the shore was found to be caused by a wave crest generated by the landslide as it decelerated at the bottom of the slope.

The visualisation of sub-surface velocities using PTV allowed the generation mechanism of the wave field to be examined. The upward flow over the front of the sliding block created a region of high pressure that forced the water directly above into a wave crest. The accelerating flow over the top and rear of the landslide created a region of low pressure that drew down the water surface into a wave trough. Once generated the crest was free to propagate, whereas the trough remained with the landslide until the block began to slow at the base of the slope and the associated low pressure region dissipated.

The PTV analysis also allowed the sub-surface motions to be seen. At the upstream position near the base of the slope, several large rotating eddies were left behind in the wake as the landslide moved past. The results from the position downstream of the final resting place of the landslide confirmed that fluid particles moved in elliptical orbits. These orbits tended to flatten towards the bottom of the water column, with purely horizontal motions at the flume floor.

References

Abe, K. (1981). "A New Scale of Tsunami Magnitude, Mt." Tsunamis: Their Science and Engineering. Proceedings of the International Tsunami Symposium, May 1981, Sendai-Ofunato-Kamaishi, Japan, l. Iida and T. Iwasaki, eds., Terra Scientific Publishing Company, 91-101.

Arnold, A., Bombach, R., Kappeli, B., and Schlegel, A. (1997). "Quantitative measurements of OH concentration fields by two-dimensional laser-induced fluorescence." *Applied Physics B: Lasers and Optics*, 64(5), 579-583.

Bardet, J. P., Synolakis, C. E., Davies, H. L., Imamura, F., and Okal, E. A. (2003). "Landslide tsunamis: Recent findings and research directions." *Pure and Applied Geophysics*, 160(10-11), 1793-1809.

Barnes, G. E. (2000). *Soil mechanics : principles and practice*, Macmillan, Basingstoke [England].

Barnes, P. M., and Lewis, K. B. (1991). "Sheet Slides and Rotational Failures on a Convergent Margin - the Kidnappers Slide, New-Zealand." *Sedimentology*, 38(2), 205-221.

Bryant, E. (2001). *Tsunami : the underrated hazard*, Cambridge University Press, Cambridge ; New York.

Churchill Controls Ltd. (1977). *Wave Monitor: Technical Manual.*

Cowen, E. A., Chang, K. A., and Liao, Q. (2001). "A single-camera coupled PTV-LIF technique." *Experiments in Fluids*, 31(1), 63-73.

Davies, H. L., Davies, J. M., Perembo, R. C. B., and Lus, W. Y. (2003). "The Aitape 1998 tsunami: Reconstructing the event from interviews and field mapping." *Pure and Applied Geophysics*, 160(10-11), 1895-1922.

Day, S. J., Watts, P., Grilli, S. T., and Kirby, J. T. (2005). "Mechanical models of the 1975 Kalapana, Hawaii earthquake and tsunami." *Marine Geology*, 215(1-2 SPEC ISS), 59-92.

de Lange, W. P., and Moon, V. G. (2004). "Estimating Earthquake and Landslide Tsunami Hazard for the New Zealand Coast." *Bulletin of the New Zealand Society for Earthquake Engineering*, 37(2), 62-69.

Enet, F., Grilli, S. T., and Watts, P. "Laboratory Experiments for Tsunamis Generated by Underwater Landslides: Comparison with Numerical Modeling." *Proceedings of the Thirteenth (2003) International Offshore and Polar Engineering Conference, May 25 2003-May 30 2003*, Honolulu, HI, United States, 1717-1724.

Fine, I. V., Rabinovich, A. B., Bornhold, B. D., Thomson, R. E., and Kulikov, E. A. (2005). "The Grand Banks landslide-generated tsunami of November 18, 1929: Preliminary analysis and numerical modeling." *Marine Geology*, 215(1-2 SPEC ISS), 45-57.

Finn, W. D. L. (2003). "Landslide-generated tsunamis: Geotechnical considerations." *Pure and Applied Geophysics*, 160(10-11), 1879-1894.

Fleming, J. G., Walters, R. A., Sue, L. P., and Nokes, R. I. (2005). "Experimental Design For Solid Block and Granular Submarine Landslides: A Unified Approach." Tsunamis: Case Studies and Recent Developments, K. Satake, ed., Springer, 259-277.

Fritz, H. M., Hager, W. H., and Minor, H. E. (2003a). "Landslide generated impulse waves. 1. Instantaneous flow fields." *Experiments in Fluids*, 35(6), 505-519.

Fritz, H. M., Hager, W. H., and Minor, H. E. (2003b). "Landslide generated impulse waves. 2. Hydrodynamic impact craters." *Experiments in Fluids*, 35(6), 520-532.

Gogineni, S., Bush, D., and Katsaros, K. "Quasi-laboratory measurements on Lake Washington for investigating radar backscattering from ocean surfaces." *10th Annual International Geoscience and Remote Sensing Symposium - IGARSS '90, May 20 1990*, College Park, MD, USA, 1067-1069.

Grilli, S. T., Kirby, J. T., Liu, P. L. F., Brandes, H., and Fryer, G. J. (2003). "Workshop on Model Validation and Benchmarking For Tsunami Generation by Submarine Mass Failure - Proposal Submitted to NSF." Honolulu, Hawaii.

Grilli, S. T., Vogelmann, S., and Watts, P. (2002). "Development of a 3D numerical wave tank for modeling tsunami generation by underwater landslides." *Engineering Analysis with Boundary Elements*, 26(4), 301-313.

Grilli, S. T., and Watts, P. (1999). "Modeling of waves generated by a moving submerged body. Applications to underwater landslides." *Engineering Analysis with Boundary Elements*, 23(8), 645-656.

Grilli, S. T., and Watts, P. (2005). "Tsunami generation by submarine mass failure. I: Modeling, experimental validation and sensitivity analyses." *Journal of Waterway, Port, Coastal and Ocean Engineering*, 131(6), 283-297.

Hampton, M. A., Lee, H. J., and Locat, J. (1996). "Submarine landslides." *Reviews of Geophysics*, 34(1), 33-59.

Horikawa, K., and Shuto, N. (1981). "Tsunami Disasters and Protection Measures in Japan." Tsunamis: Their Science and Engineering. Proceedings of the International Tsunami Symposium, May 1981, Sendai-Ofunato-Kamaishi, Japan, I. Iida and T. Iwasaki, eds., Terra Scientific Publishing Company, 9-22.

Houcine, I., Vivier, H., Plasari, E., David, R., and Villermaux, J. (1996). "Planar laser induced fluorescence technique for measurements of concentration fields in continuous stirred tank reactors." *Experiments in Fluids*, 22(2), 95-102.

Hsu, C. T., Kuang, J., and Sun, J. H. (2001). "Flapping instability of vertically impinging turbulent plane jets in shallow water." *Journal of Engineering Mechanics*, 127(5), 411-420.

Imamura, F., and Hashi, K. (2003). "Re-examination of the source mechanism of the 1998 Papua New Guinea earthquake and tsunami." *Pure and Applied Geophysics*, 160(10-11), 2071-2086.

Ishihara, K. (2002). "Failure of Slopes and Soil Property Characterization - 2nd Lumb Lecture in Hong Kong." Hong Kong, 1-38.

Jiang, L., and Leblond, P. H. (1992). "The Coupling of a Submarine Slide and the Surface-Waves Which It Generates." *Journal of Geophysical Research-Oceans*, 97(C8), 12731-12744.

Kanoglu, U. "Nonlinear Evolution and Runup of a Solitary Wave Over a Sloping Beach." *Long Waves Symposium*, AUTh, Thessaloniki, Greece, 281-288.

Kennedy, A. B., Chen, Q., Kirby, J. T., and Dalrymple, R. A. (2000). "Boussinesq modeling of wave transformation, breaking, end runup. I: 1D." *Journal of Waterway Port Coastal and Ocean Engineering-Asce*, 126(1), 39-47.

Kozlova, T. G., Lobacheva, M. I., Pravdin, A. B., Romakina, M. Y., Sinichlin, Y. P., and Tuchin, V. V. "Laser spectroscopy of carotenoids in plant bioobjects." *International Conference on Laser Applications in Life Sciences Part 1 (of 2), Aug 27-31 1990*, Moscow, USSR, 159-160.

Lebey, M., and Rivoalen, E. (2002). "Experimental study of the working principal and efficiency of a superposed inclined planes wave absorber." *Ocean Engineering*, 29(11), 1427-1440.

Lee, H. J., Kayen, R. E., Gardner, J. V., and Locat, J. (2003). "Characteristics of Several Tsunamigenic Submarine Landslides." Submarine mass movements and their consequences : 1st international symposium, J. Locat and J. Mienert, eds., Kluwer Academic Publishers, Boston, 357-366.

Lee, J. J., Chang, C., and Zhuang, F. "Interaction of nonlinear waves with coastal structures." *Proceedings of the 23rd International Conference on Coastal Engineering, Oct 4-9 1992*, Venice, Italy, 1327-1340.

Liu, P. L. F., Wu, T. R., Raichlen, F., Synolakis, C. E., and Borrero, J. C. (2005). "Runup and rundown generated by three-dimensional sliding masses." *Journal of Fluid Mechanics*, 536, 107-144.

Locat, J., and Lee, H. J. (2002). "Submarine landslides: Advances and challenges." *Canadian Geotechnical Journal*, 39(1), 193-212.

Lommer, M., and Levinsen, M. T. (2002). "Using Laser-Induced Fluorescence in the Study of Surface Wave Turbulence." *Journal of Fluorescence*, 12(1), 45-50.
Lynett, P. J., Borrero, J. C., Liu, P. L. F., and Synolakis, C. E. (2003). "Field survey and numerical simulations: A review of the 1998 Papua New Guinea tsunami." *Pure and Applied Geophysics*, 160(10-11), 2119-2146.
Mariotti, C., and Heinrich, P. (1999). "Modelling of submarine landslides of rock and soil." *International Journal for Numerical and Analytical Methods in Geomechanics*, 23(4), 335-354.
Martel, S. J. (2004). "Mechanics of landslide initiation as a shear fracture phenomenon." *Marine Geology*, 203(3-4), 319-339.
McAdoo, B. G., Pratson, L. F., and Orange, D. L. (2000). "Submarine landslide geomorphology, US continental slope." *Marine Geology*, 169(1-2), 103-136.
Mori, N., and Chang, K.-A. (2003). "Experimental study of a horizontal jet in a wavy environment." *Journal of Engineering Mechanics*, 129(10), 1149-1155.
Murty, T. S. (2003). "Tsunami wave height dependence on landslide volume." *Pure and Applied Geophysics*, 160(10-11), 2147-2153.
New Scientist. (2004). "Hawaiian Tsunami Left a Gift at the Foot of Kohala Volcano." *New Scientist*, 2464(2464), 14.
Nokes, R. I. (2005a). "FluidStream v6.01: System Theory and Design." Christchurch, New Zealand, Particle Tracking Velocimetry (PTV).
Nokes, R. I. (2005b). "FluidStream v6.01: User's Guide." Christchurch, New Zealand, Particle Tracking Velocimetry (PTV).
Nokes, R. I. (2005c). "ImageStream v5.01: System Theory and Design." Christchurch, New Zealand, Image Processing.
Okal, E. A. (2003). "T waves from the 1998 Papua New Guinea earthquake and its aftershocks: Timing the tsunamigenic slump." *Pure and Applied Geophysics*, 160(10-11), 1843-1863.
Ouellet, Y., and Datta, I. (1986). "A Survey of Wave Absorbers." *Journal of Hydraulic Research*, 24(4), 265-280.
Papadopoulos, G. A., and Kortekaas, S. (2003). "Characteristics of Landslide Generated Tsunamis From Observational Data." Submarine mass movements and their consequences : 1st international symposium, J. Locat and J. Mienert, eds., Kluwer Academic Publishers, Boston, 367-374.
Peacock, K. (2002). "Stations Should Have a Tsunami Tactical Plan." Star, 14.
Raichlen, F., and Synolakis, C. E. "Run-up From Three-Dimensional Sliding Masses." *Long Waves Symposium*, AUTh, Thessaloniki, Greece, 247-256.
Ruff, L. J. (2003). "Some aspects of energy balance and tsunami generation by earthquakes and landslides." *Pure and Applied Geophysics*, 160(10-11), 2155-2176.
Rzadkiewicz, S. A., Mariotti, C., and Heinrich, P. (1997). "Numerical simulation of submarine landslides and their hydraulic effects." *Journal of Waterway Port Coastal and Ocean Engineering-Asce*, 123(4), 149-157.
Satake, K., and Tanioka, Y. (2003). "The July 1998 Papua New Guinea earthquake: Mechanism and quantification of unusual tsunami generation." *Pure and Applied Geophysics*, 160(10-11), 2087-2118.
Shiono, K., and Feng, T. (2003). "Turbulence measurements of dye concentration and effects of secondary flow on distribution in open channel flows." *Journal of Hydraulic Engineering*, 129(5), 373-384.
Shuto, N. (1991). "Tsunami Intensity and Disasters. Proceedings of the Fifteenth Interbational Tsunami Symposium, 1991, Vienna, Austria." Tsunamis in the World, S. Tinti, ed., Kluwer Academic Publishers, 197-216.
Shy, S., Yeh, W. J., and Chu, C. C. "Velocity measurements and flow visualizations of jet interaction with a sharp density interface." *Proceedings of the 1997 ASME Fluids*

Engineering Division Summer Meeting, FEDSM'97. Part 13 (of 24), Jun 22-26 1997, Vancouver, Can, 3.

Synolakis, C. E. (1987). "The Runup of Solitary Waves." *Journal of Fluid Mechanics*, 185, 523-545.

Tappin, D. R., Watts, P., and Matsumoto, T. (2003). "Architecture and Failure Mechanism of the Offshore Slump Responsible for the 1998 Papua New Guinea Tsunami." Submarine mass movements and their consequences : 1st international symposium, J. Locat and J. Mienert, eds., Kluwer Academic Publishers, Boston, 383-389.

Tappin, D. R., Watts, P., McMurtry, G. M., Lafoy, Y., and Matsumoto, T. (2001). "The Sissano, Papua New Guinea tsunami of July 1998 - offshore evidence on the source mechanism." *Marine Geology*, 175(1-4), 1-23.

Tarman, H. I., and Kanoglu, U. "Numerical Simulation of Long Wave Runup on a Sloping Beach." *Long Waves Symposium*, AUTh, Thessaloniki, Greece, 273-279.

Tian, X., and Roberts, P. J. W. (2003). "A 3D LIF system for turbulent buoyant jet flows." *Experiments in Fluids*, 35(6), 636-647.

Tinti, S., Armigliato, A., Manucci, A., Pagnoni, G., Zaniboni, F., Yalciner, A. C., and Altinok, Y. (2006). "The generating mechanisms of the August 17, 1999 Izmit bay (Turkey) tsunami: Regional (tectonic) and local (mass instabilities) causes." *Marine Geology*, 225(1-4), 311-330.

Tinti, S., and Bortolucci, E. (2000). "Energy of water waves induced by submarine landslides." *Pure and Applied Geophysics*, 157(3), 281-318.

Tinti, S., Bortolucci, E., and Romagnoli, C. (2000). "Computer simulations of tsunamis due to sector collapse at Stromboli, Italy." *Journal of Volcanology and Geothermal Research*, 96(1-2), 103-128.

VanLerberghe, W. M., Santiago, J. G., Dutton, J. C., and Lucht, R. P. (2000). "Mixing of a sonic transverse jet injected into a supersonic flow." *AIAA Journal*, 38(3), 470-479.

Walters, R. "Tsunami Runup: Model Development and Testing." *Long Waves Symposium*, AUTh, Thessaloniki, Greece, 289-296.

Wang, H. J., and Davidson, M. J. (2001). "A profile tracking system for investigating the behaviour of discharges in moving environments." *Experiments in Fluids*, 31(5), 533-541.

Ward, S. N. (2001). "Landslide tsunami." *Journal of Geophysical Research-Solid Earth*, 106(B6), 11201-11215.

Watts, P. (1997). "Water Waves Generated by Underwater Landslides," PhD, California Institute of Technology, Pasadena, California.

Watts, P. (1998). "Wavemaker curves for tsunamis generated by underwater landslides." *Journal of Waterway Port Coastal and Ocean Engineering-Asce*, 124(3), 127-137.

Watts, P. (2000). "Tsunami features of solid block underwater landslides." *Journal of Waterway Port Coastal and Ocean Engineering-Asce*, 126(3), 144-152.

Watts, P., and Grilli, S. T. "Underwater Landslide Shape, Motion, Deformation, and Tsunami Generation." *Proceedings of the Thirteenth (2003) International Offshore and Polar Engineering Conference, May 25 2002-May 30 2003*, Honolulu, HI, United States, 1709-1716.

Watts, P., Grilli, S. T., Tappin, D. R., and Fryer, G. J. (2005). "Tsunami generation by submarine mass failure. II: Predictive equations and case studies." *Journal of Waterway, Port, Coastal and Ocean Engineering*, 131(6), 298-310.

Watts, P., Imamura, F., Bengston, A., and Grilli, S. T. "Benchmark cases for tsunamis generated by underwater landslides." *Proceedings of the Fourth International Symposium Waves 2001, Sep 2-6 2001*, San Francisco, CA, 1505-1514.

Wiegel, R. L. (1955). "Laboratory studies of gravity waves generated by movement of submerged body." *American Geophysical Union -- Transactions*, 36(5), 759-774.

Wright, S. G., and Rathje, E. M. (2003). "Triggering mechanisms of slope instability and their relationship to earthquakes and tsunamis." *Pure and Applied Geophysics*, 160(10-11), 1865-1877.

Yeh, H. H., and Ghazali, A. "Nearshore Behaviour Of Bore On A Uniformly Sloping Beach." *Twentieth Coastal Engineering Conference, Proceedings of the International Conference.*, Taipei, Taiwan, 877-888.

Zhou, J., Lu, D., Li, Z., Sheng, K., and Duan, Y. (1994). "C2 concentration measurement in the exhaust gas of a gasoline engine by laser-induced fluorescence." *Zhongguo Jiguang/Chinese Journal of Lasers*, 21(3), 230-232.

Appendix

A.1 Water Surface Profiles

Water surface profiles are presented for all fifteen combinations of specific gravity and initial submergence in Figures A1-A15. Profiles are plotted at times of 0.600, 1.600, 2.600, 3.600, 4.600, and 5.600 seconds after landslide release.

A.2 Two-Dimensional Wave Field

The 2-dimensional water level contour plots of all fifteen combinations of specific gravity and initial submergence are presented in Figures A.16-A.30. Note that the colours within each plot are assigned such that red is the maximum positive water level, blue is the minimum water level, and the intermediate colours are assigned relative to these extremes. The black line in these figures plot the landslide's centre-of-mass horizontal position time history.

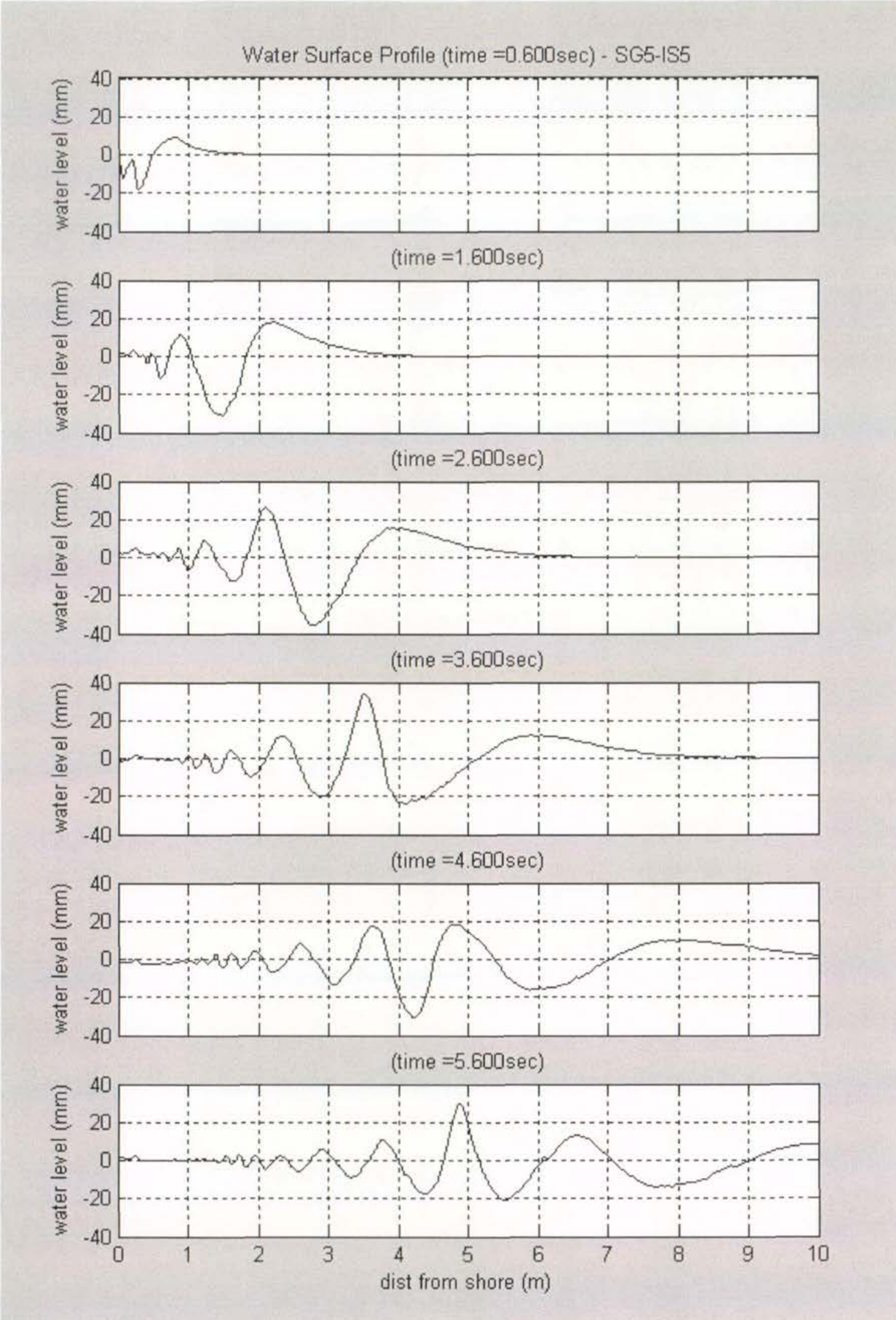

Figure A.1. Water surface profiles for the SG5_IS5 test. Specific gravity=4.02 and initial submergence=0.1.

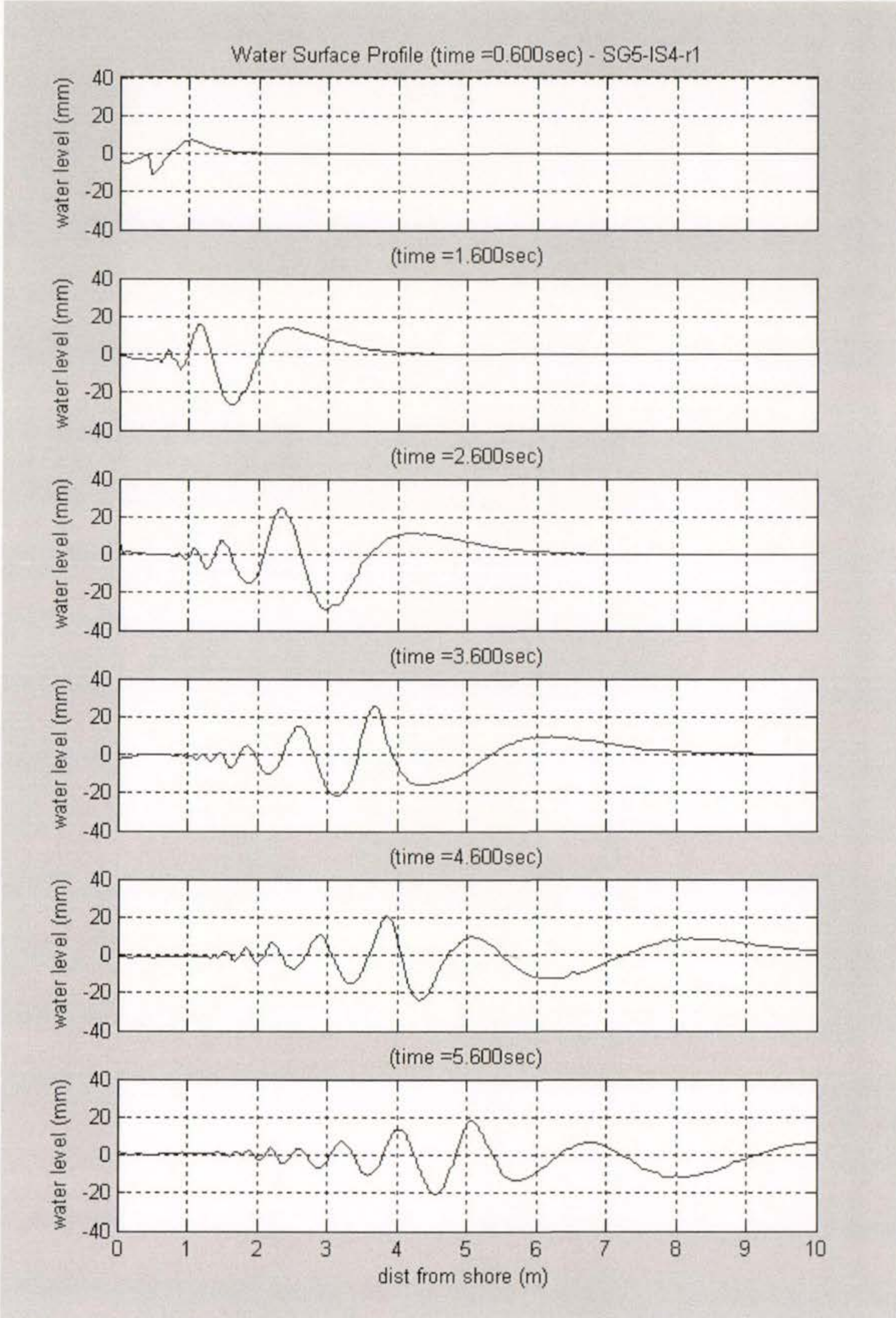

Figure A.2. Water surface profiles for the SG5_IS4 test. Specific gravity=4.02 and initial submergence=0.2.

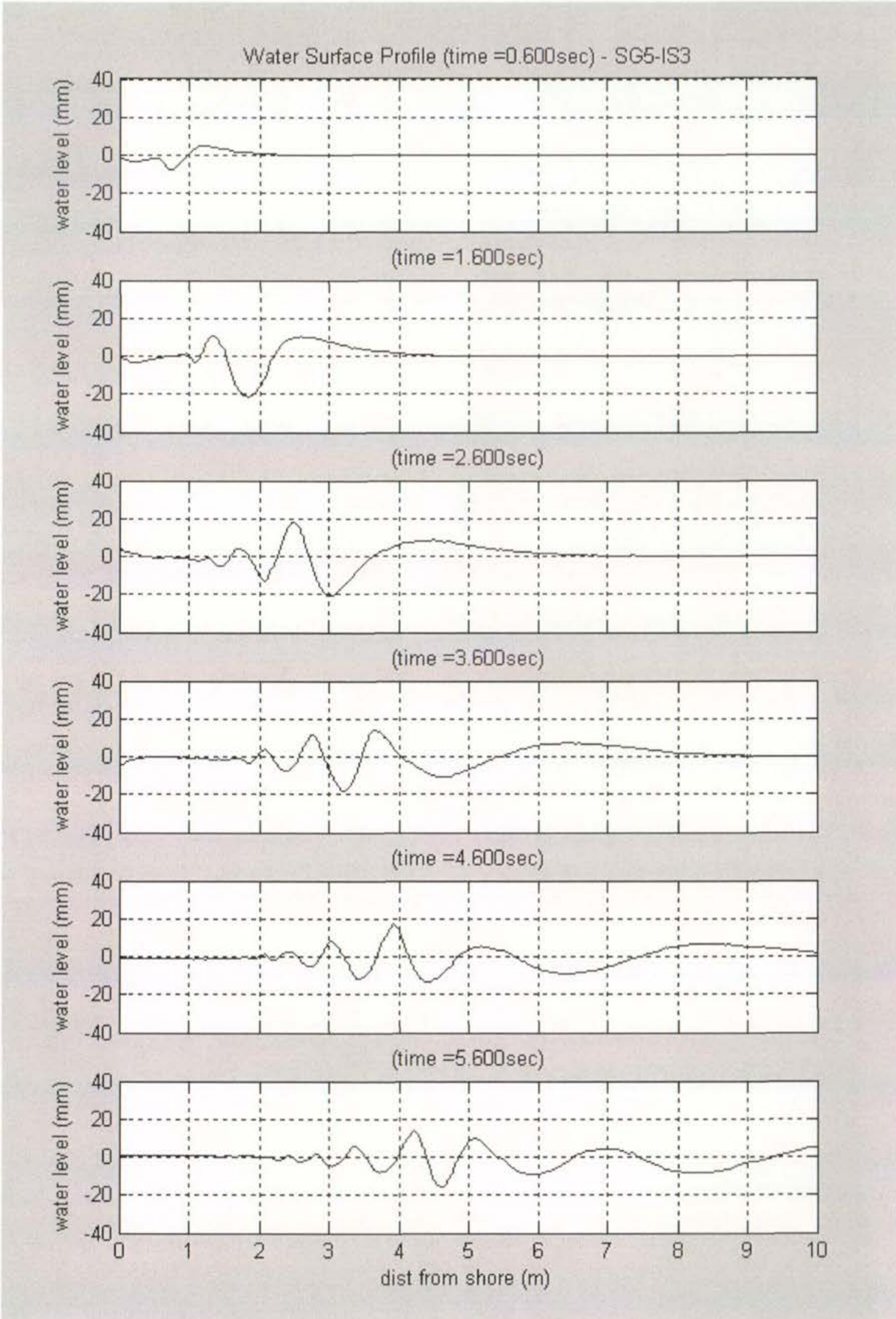

Figure A.3. Water surface profiles for the SG5_IS3 test. Specific gravity=4.02 and initial submergence=0.3.

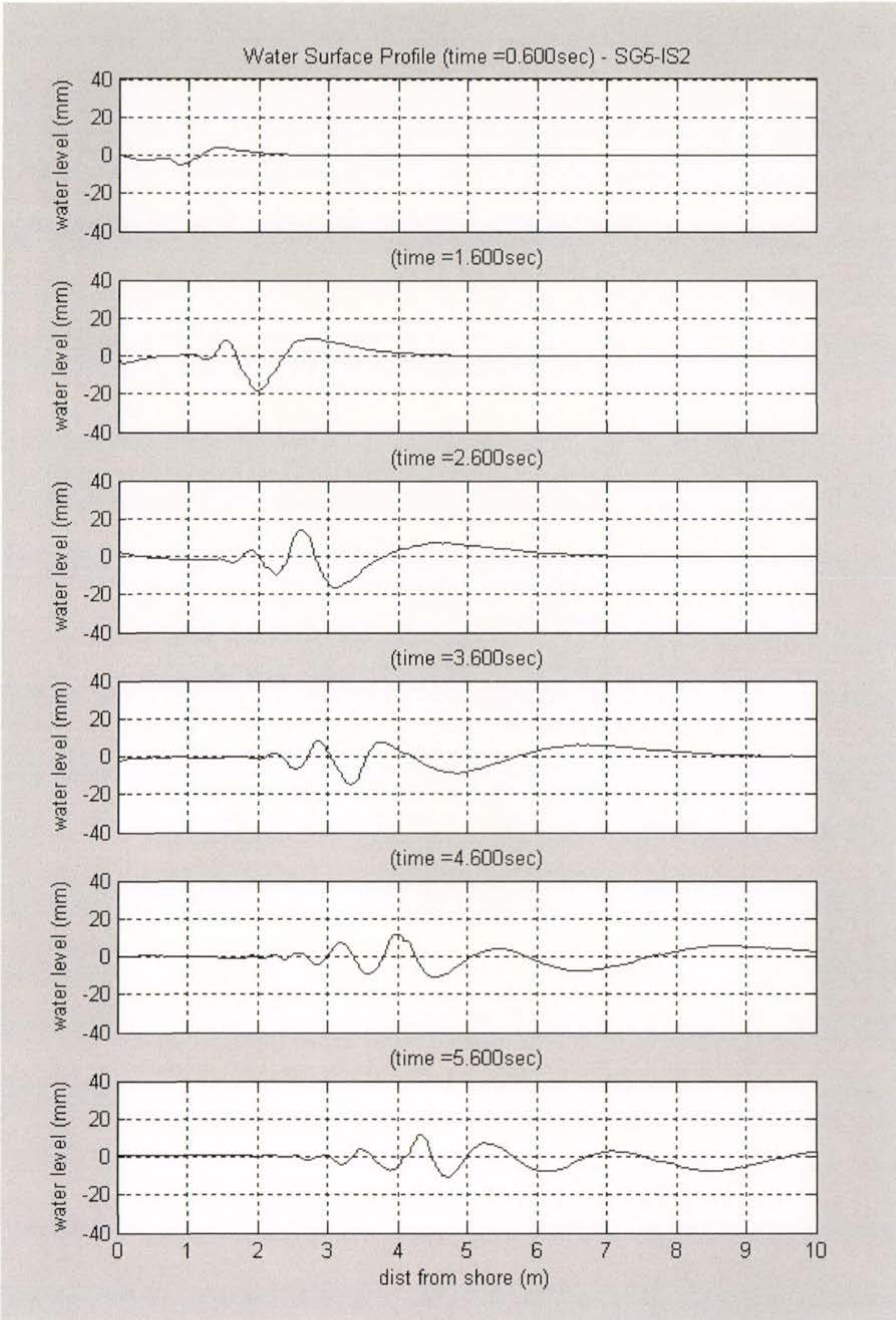

Figure A.4. Water surface profiles for the SG5_IS2 test. Specific gravity=4.02 and initial submergence=0.4.

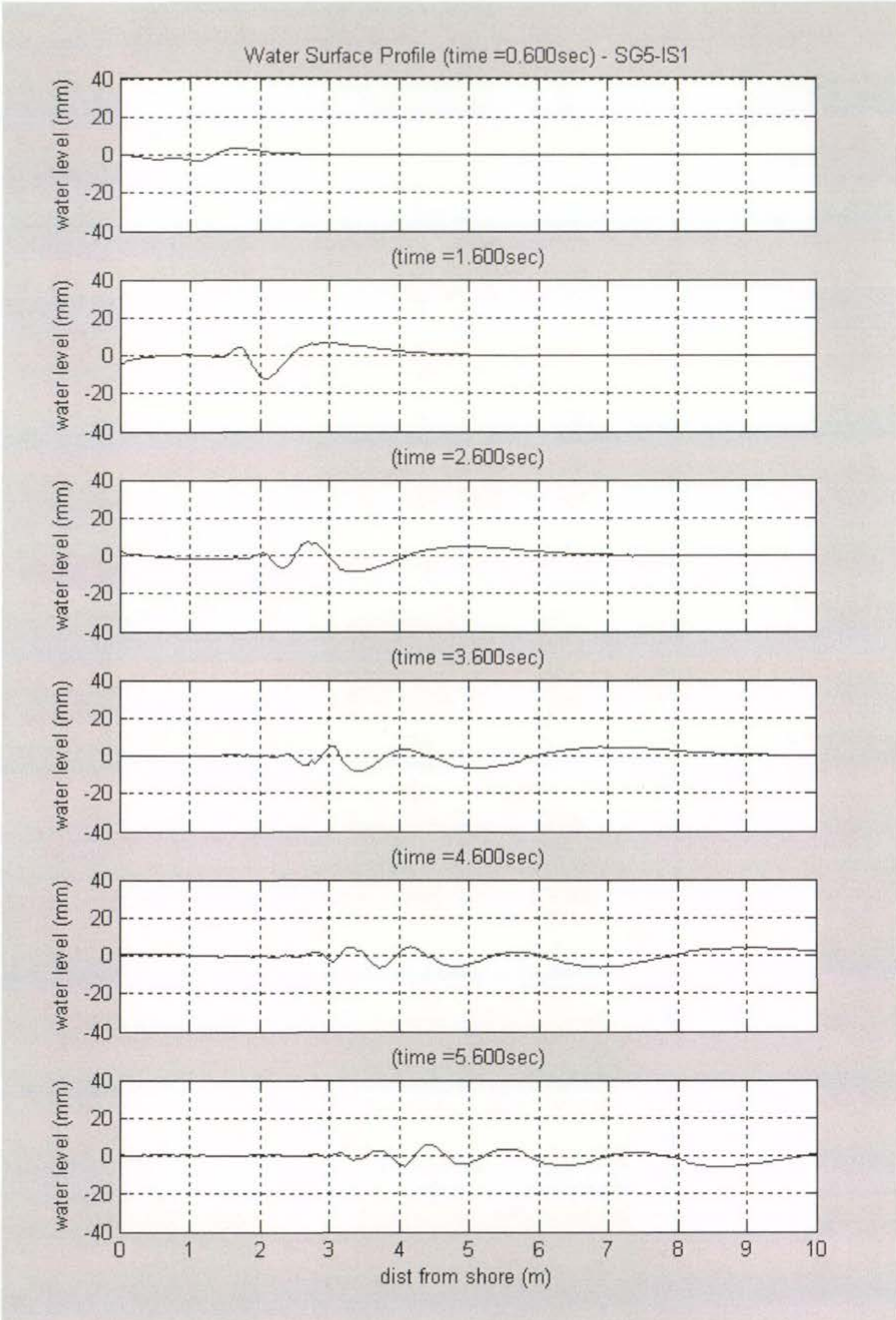

Figure A.5. Water surface profiles for the SG5_IS1 test. Specific gravity=4.02 and initial submergence=0.5.

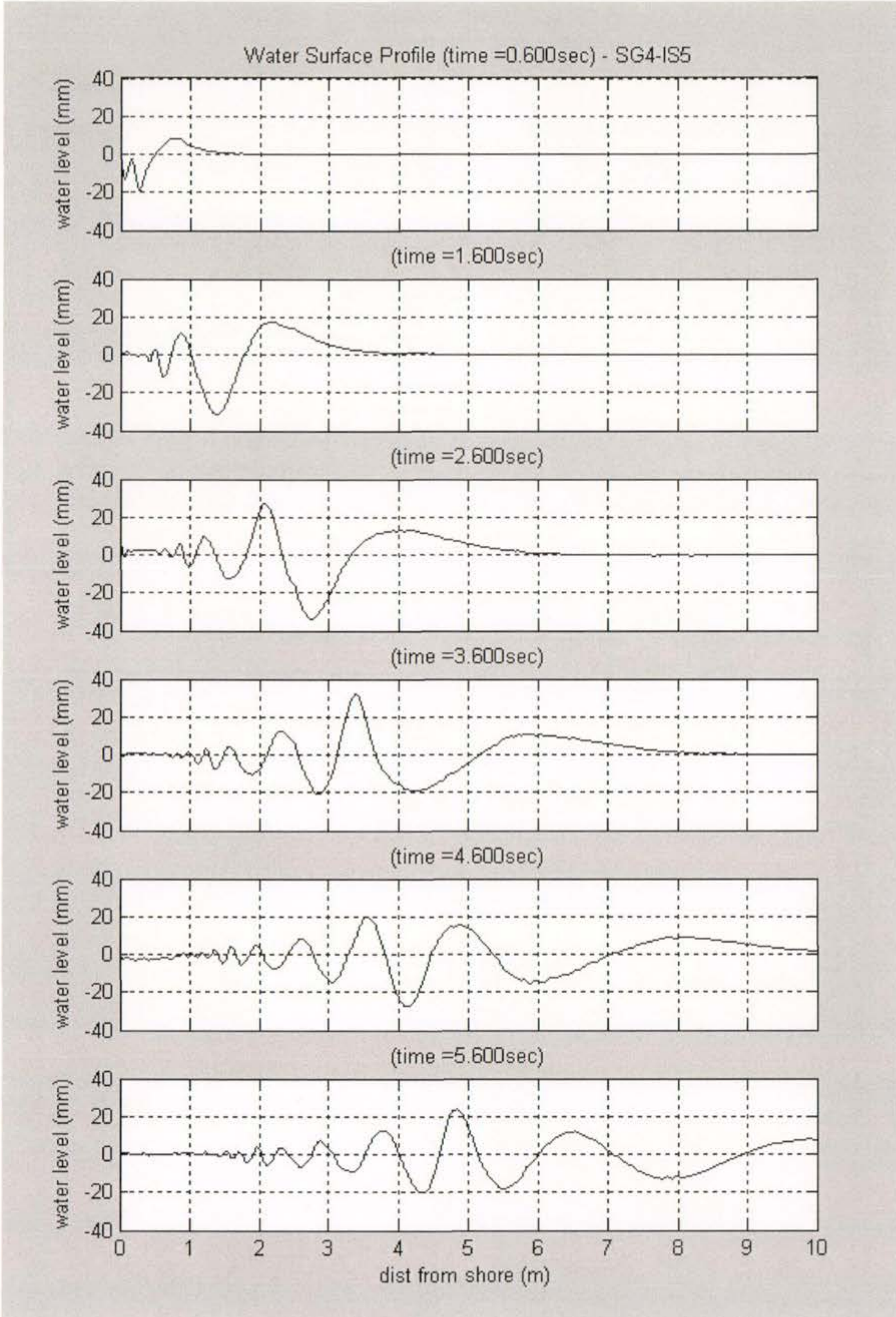

Figure A.6. Water surface profiles for the SG4_IS5 test. Specific gravity=3.42 and initial submergence=0.1.

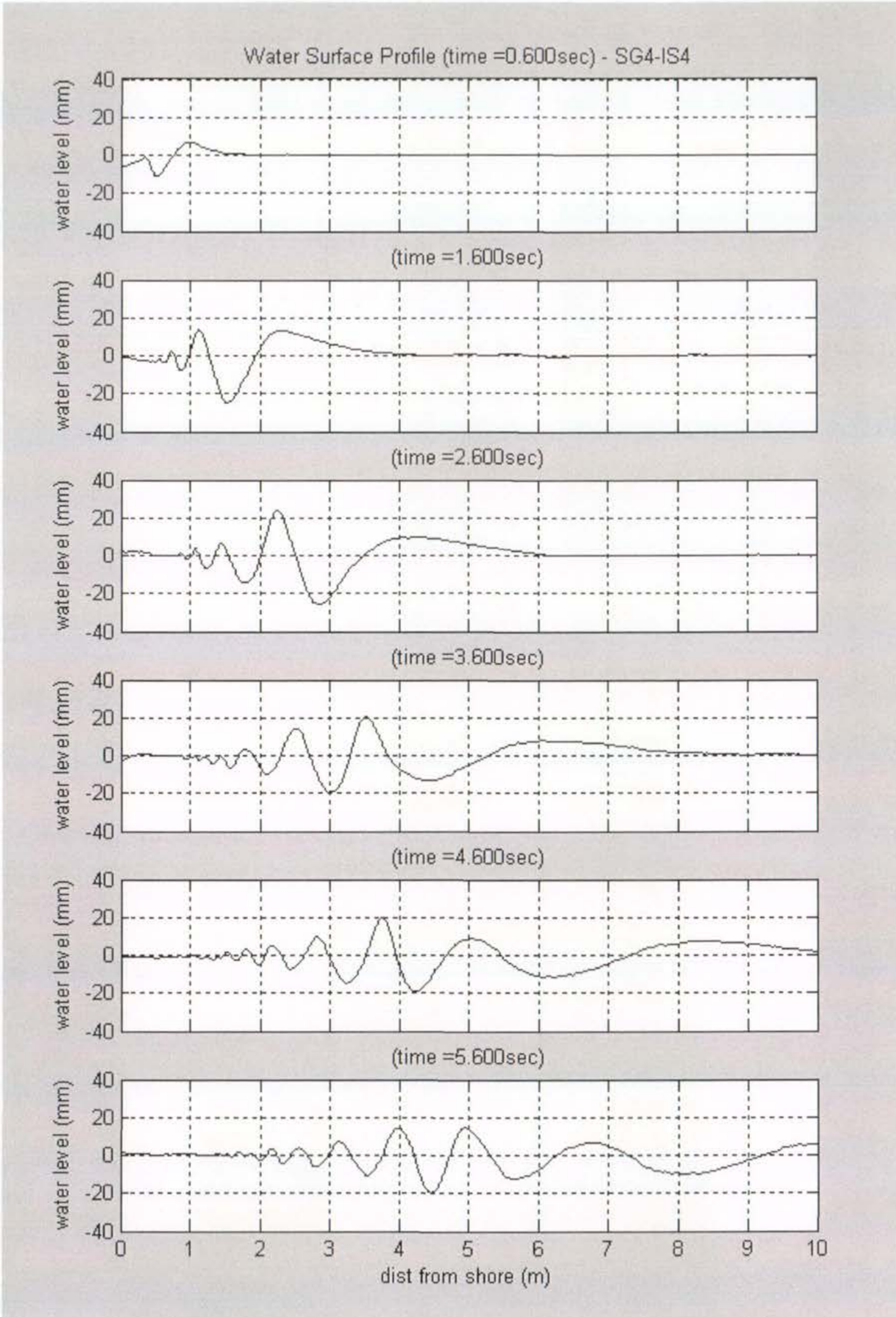

Figure A.7. Water surface profiles for the SG4_IS4 test. Specific gravity=3.42 and initial submergence=0.2.

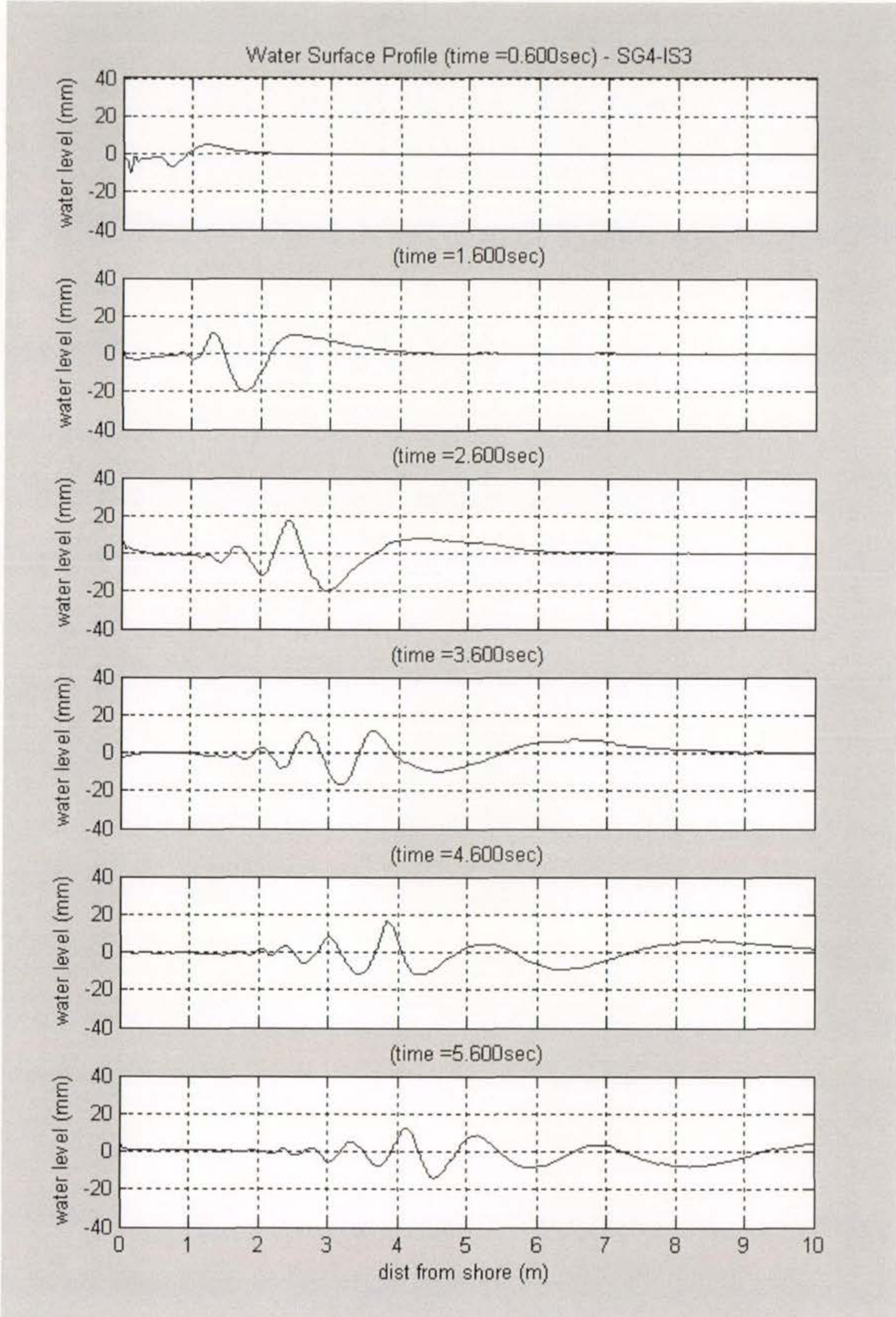

Figure A.8. Water surface profiles for the SG4_IS3 test. Specific gravity=3.42 and initial submergence=0.3.

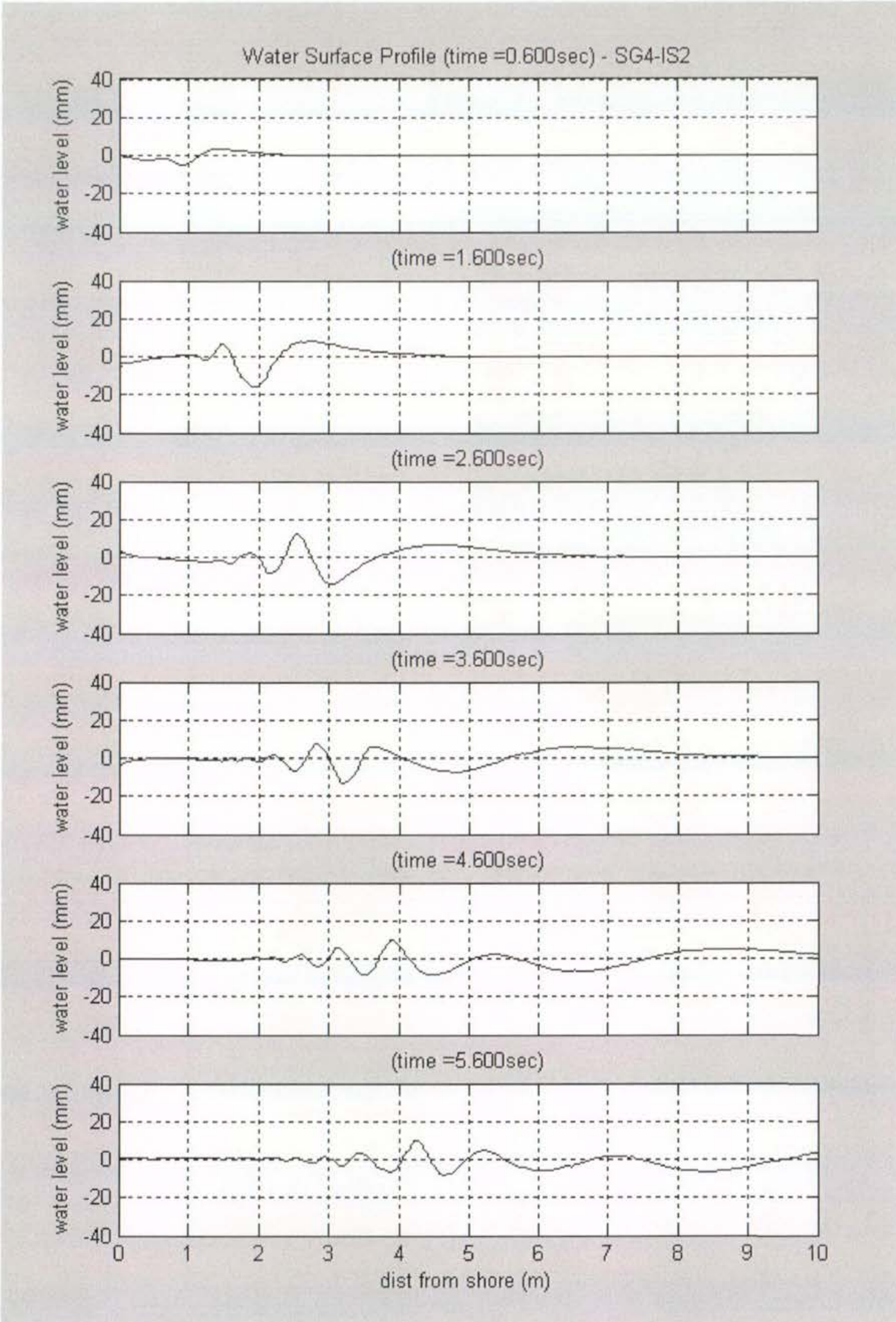

Figure A.9. Water surface profiles for the SG4_IS2 test. Specific gravity=3.42 and initial submergence=0.4.

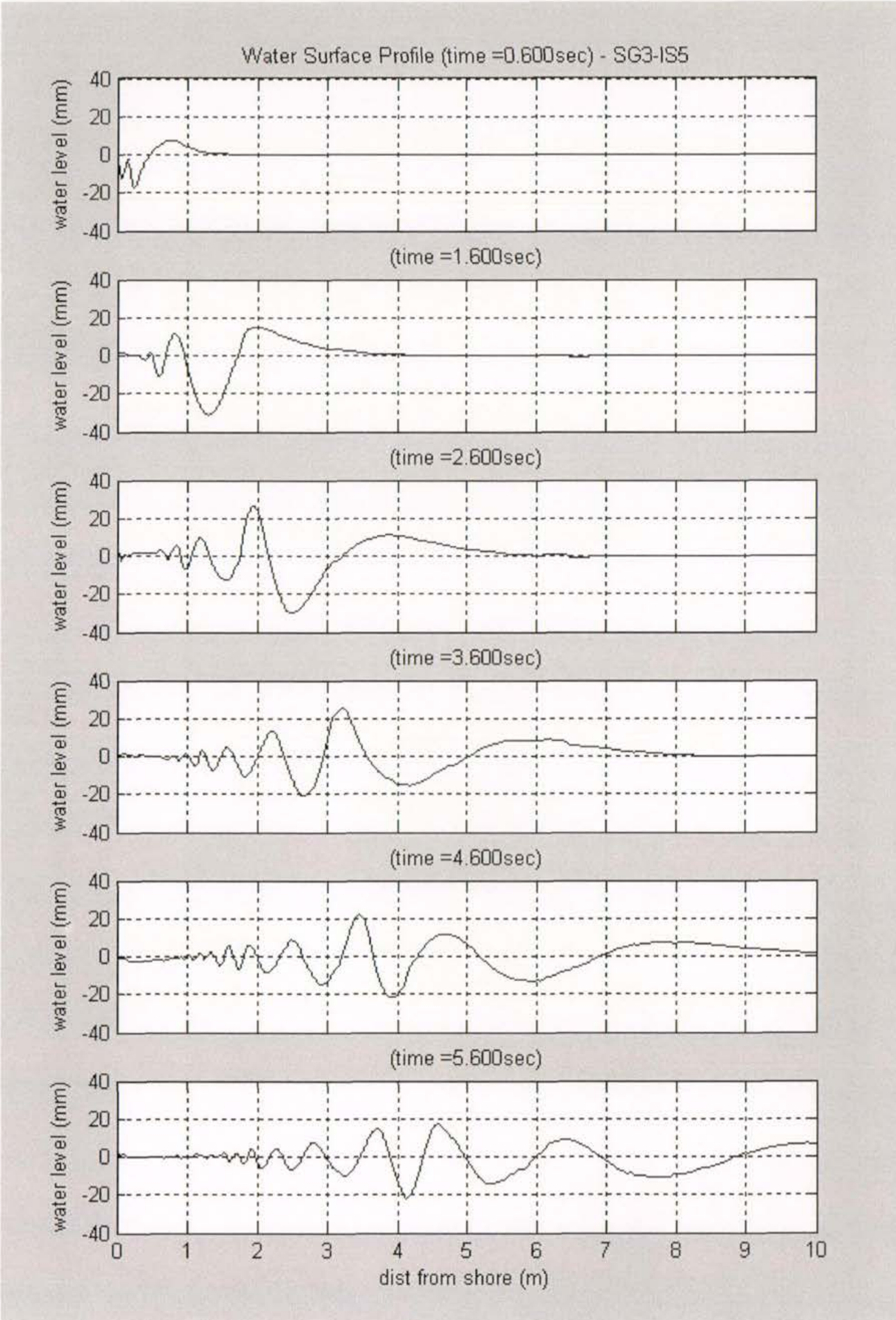

Figure A.10. Water surface profiles for the SG3_IS5 test. Specific gravity=2.83 and initial submergence=0.1.

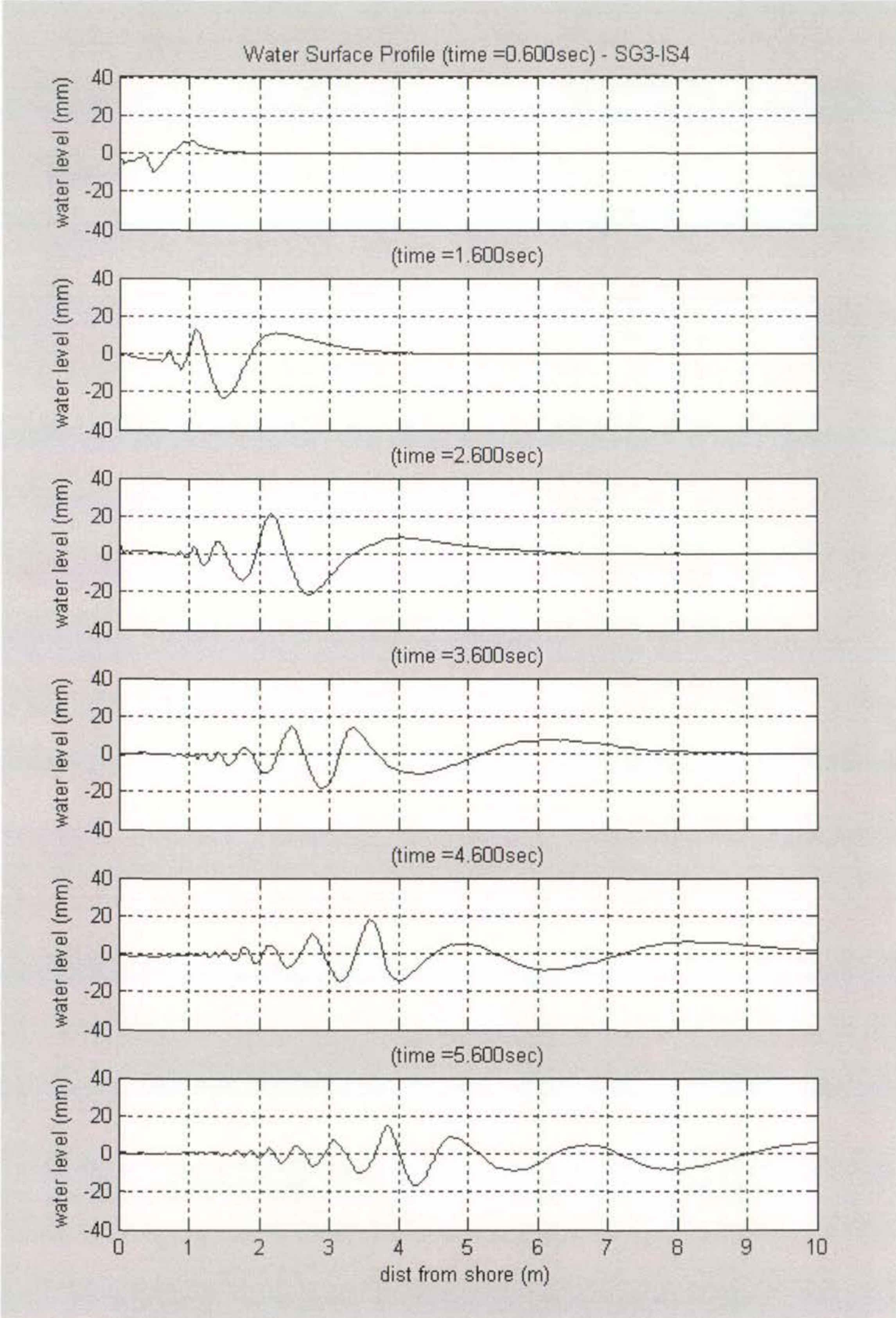

Figure A.11. Water surface profiles for the SG3_IS4 test. Specific gravity=2.83 and initial submergence=0.2.

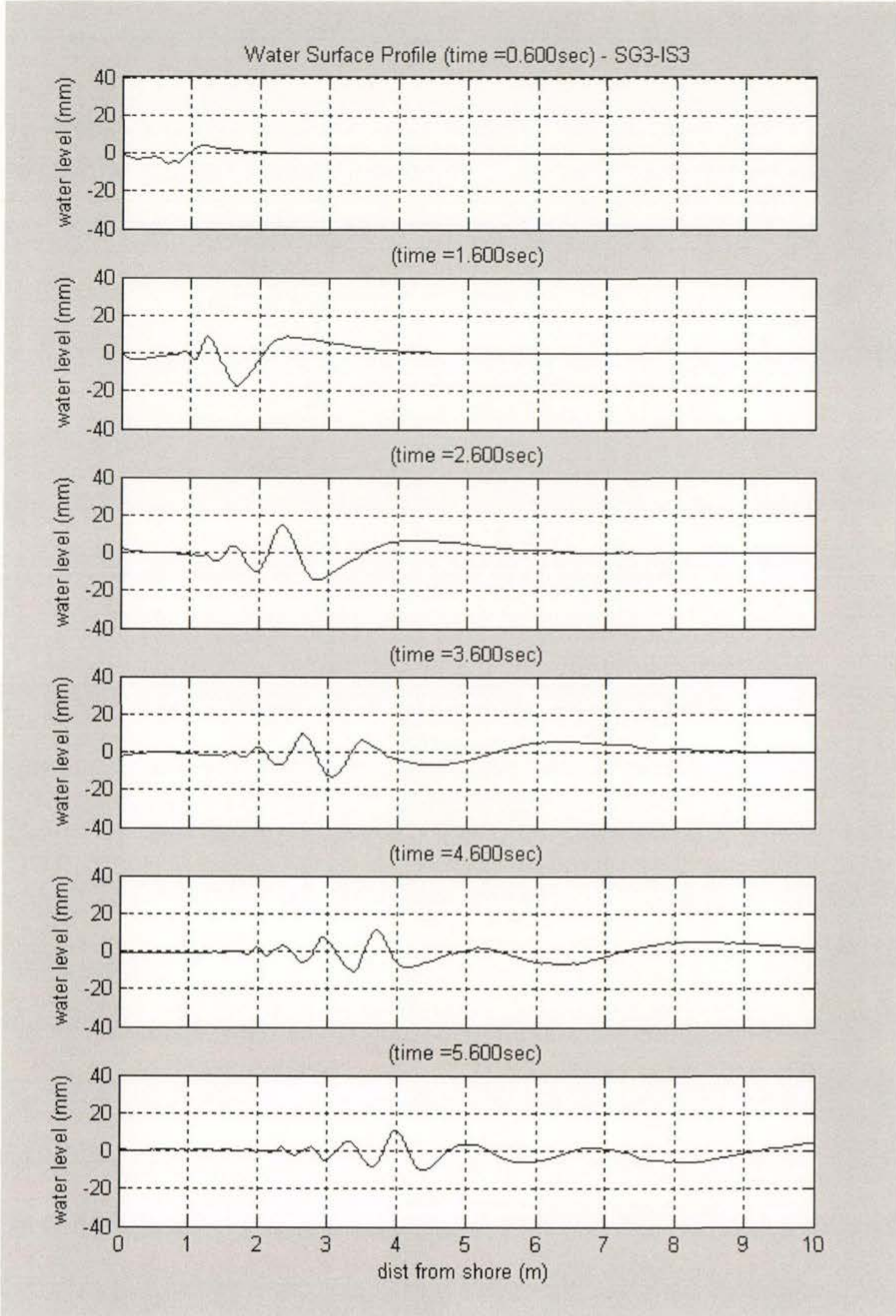

Figure A.12. Water surface profiles for the SG3_IS3 test. Specific gravity=2.83 and initial submergence=0.3.

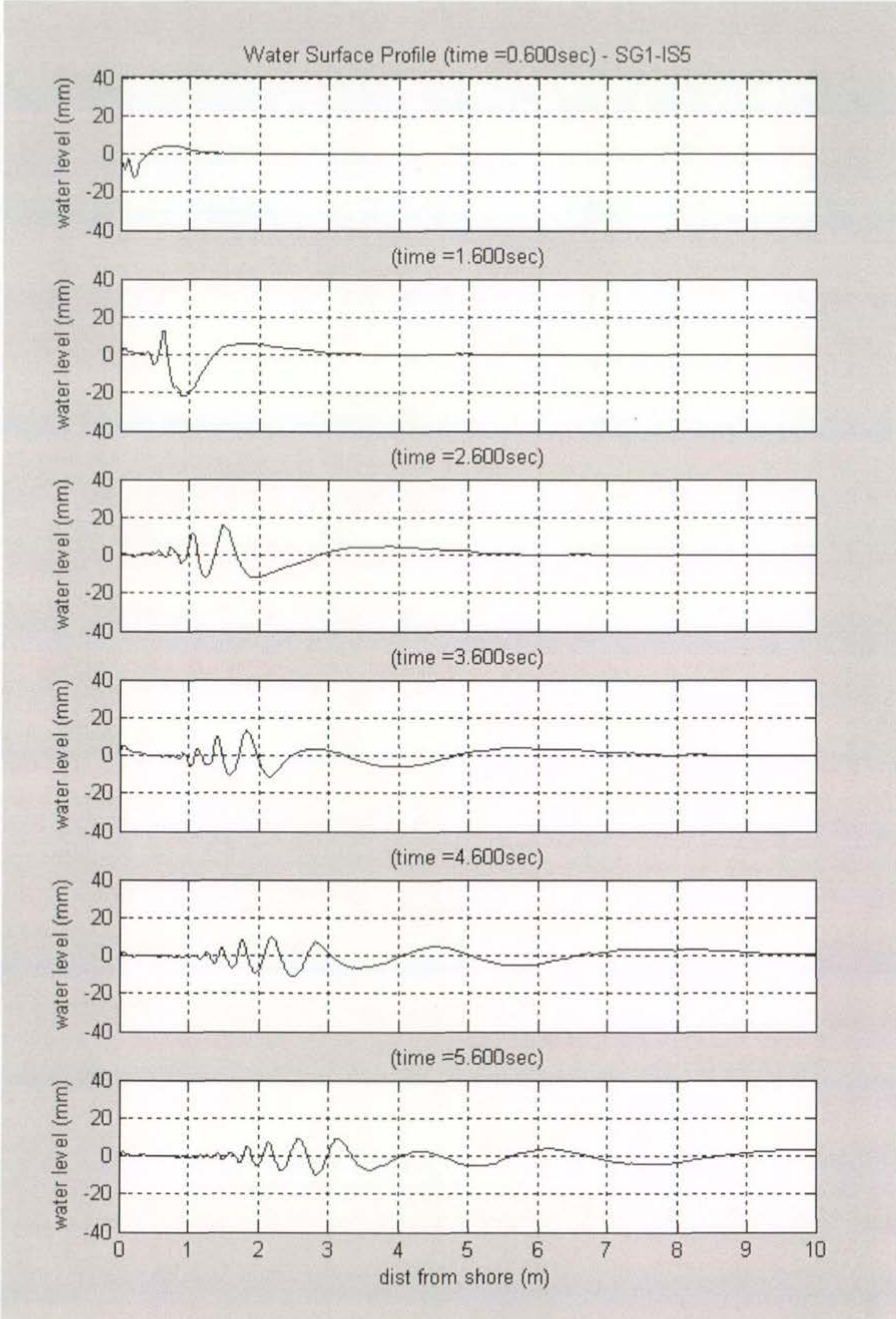

Figure A.15. Water surface profiles for the SG1_IS5 test. Specific gravity=1.63 and initial submergence=0.1.

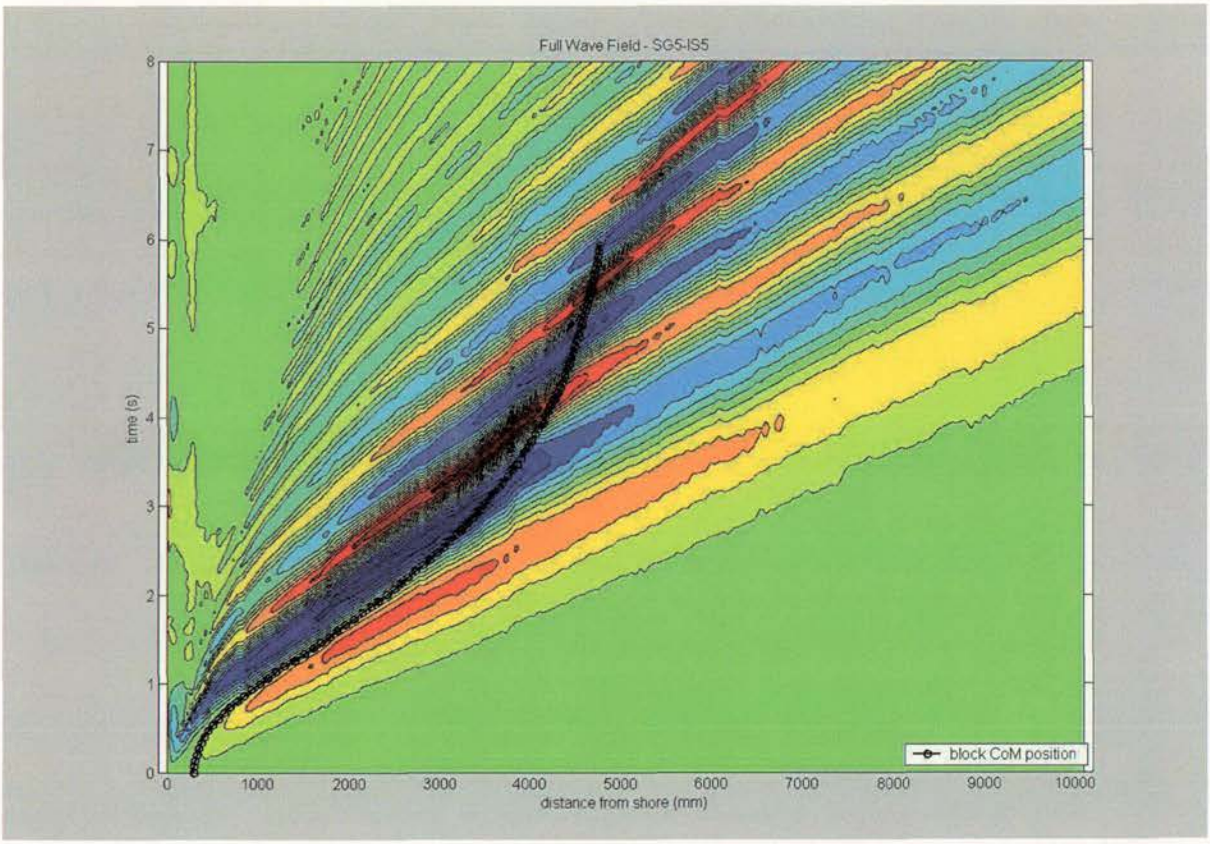

Figure A.16. 2-dimensional water level contour plot for the SG5_IS5 test. Specific gravity=4.02 and initial submergence=0.1.

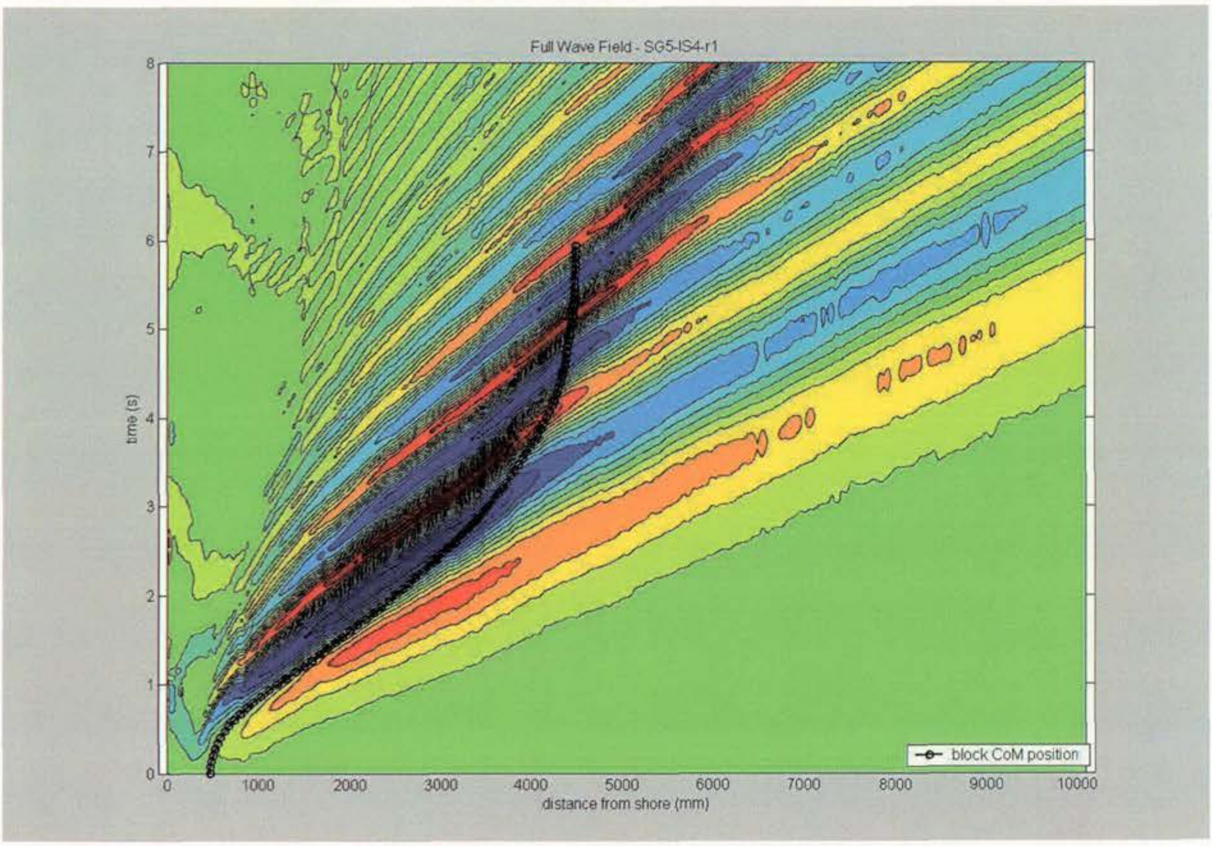

Figure A.17. 2-dimensional water level contour plot for the SG5_IS4 test. Specific gravity=4.02 and initial submergence=0.2.

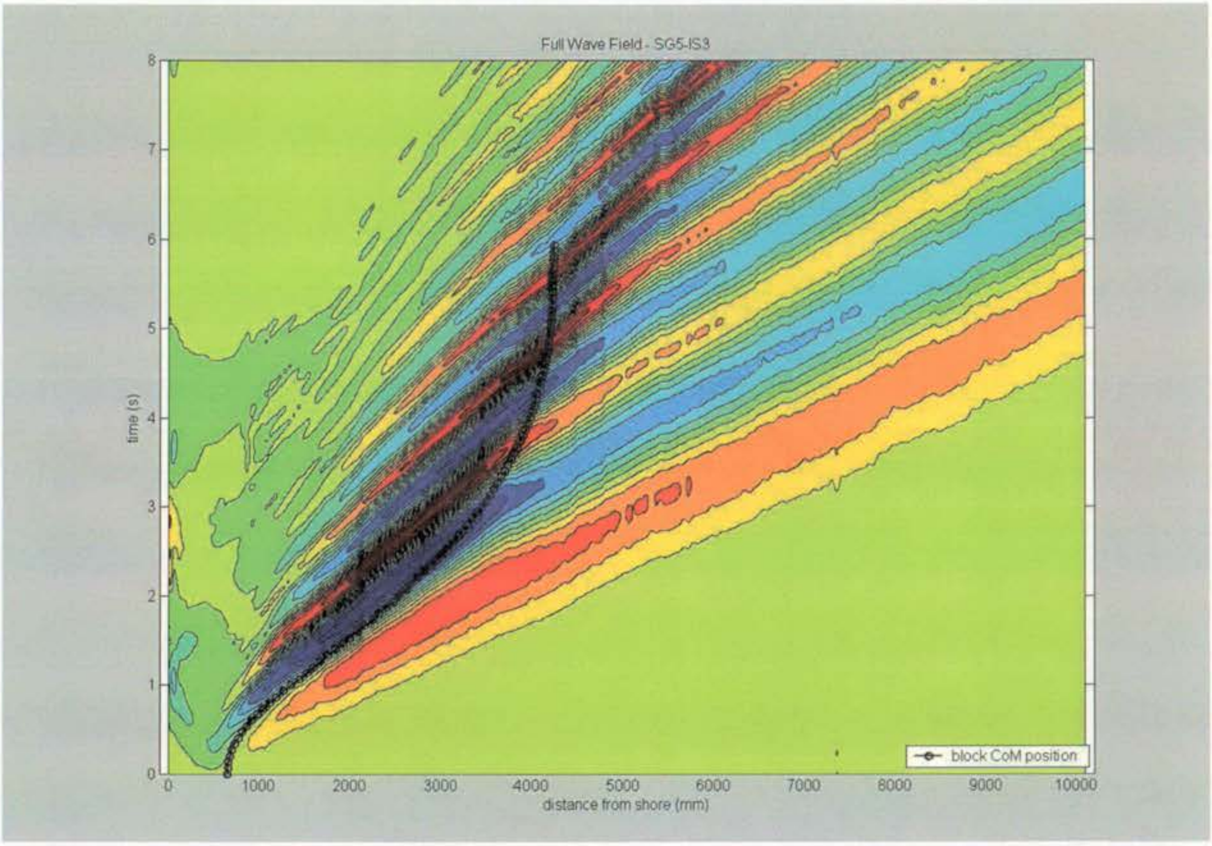

Figure A.18. 2-dimensional water level contour plot for the SG5_IS3 test. Specific gravity=4.02 and initial submergence=0.3.

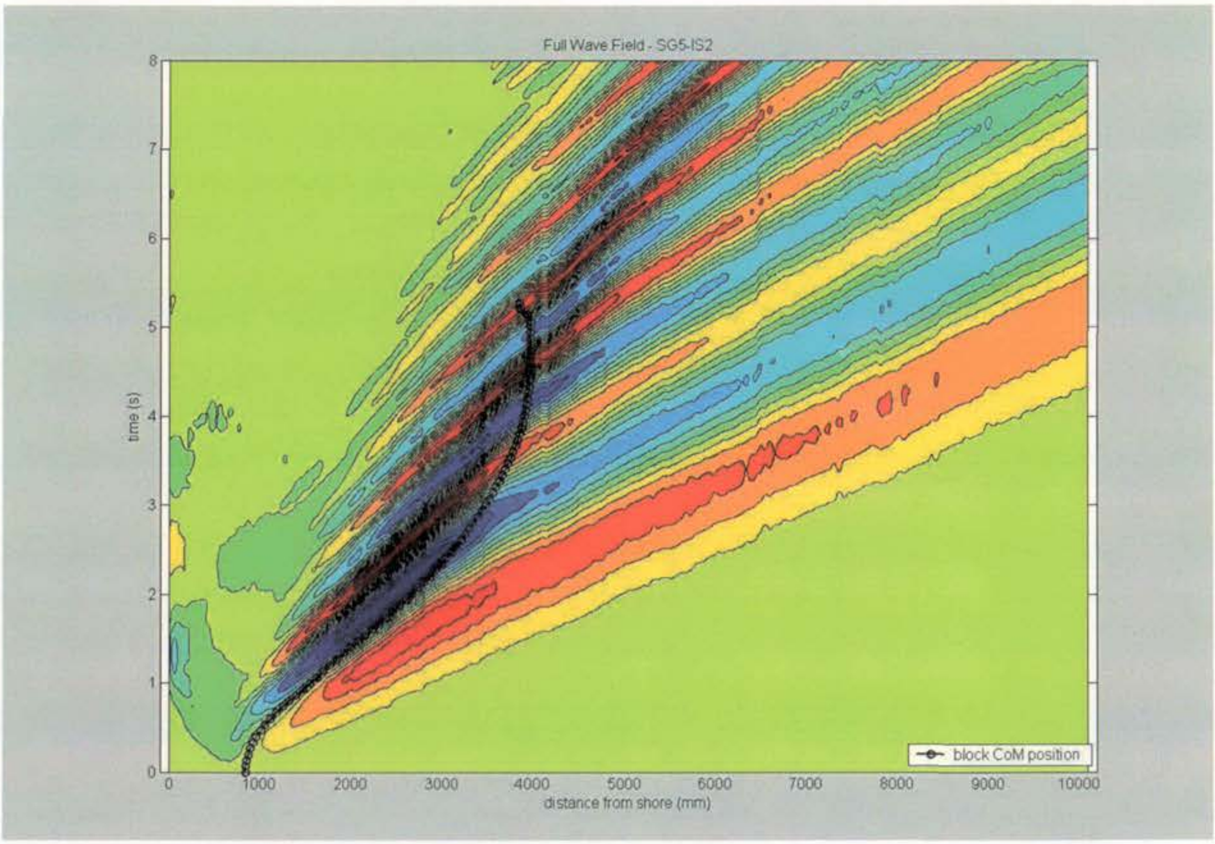

Figure A.19. 2-dimensional water level contour plot for the SG5_IS2 test. Specific gravity=4.02 and initial submergence=0.4.

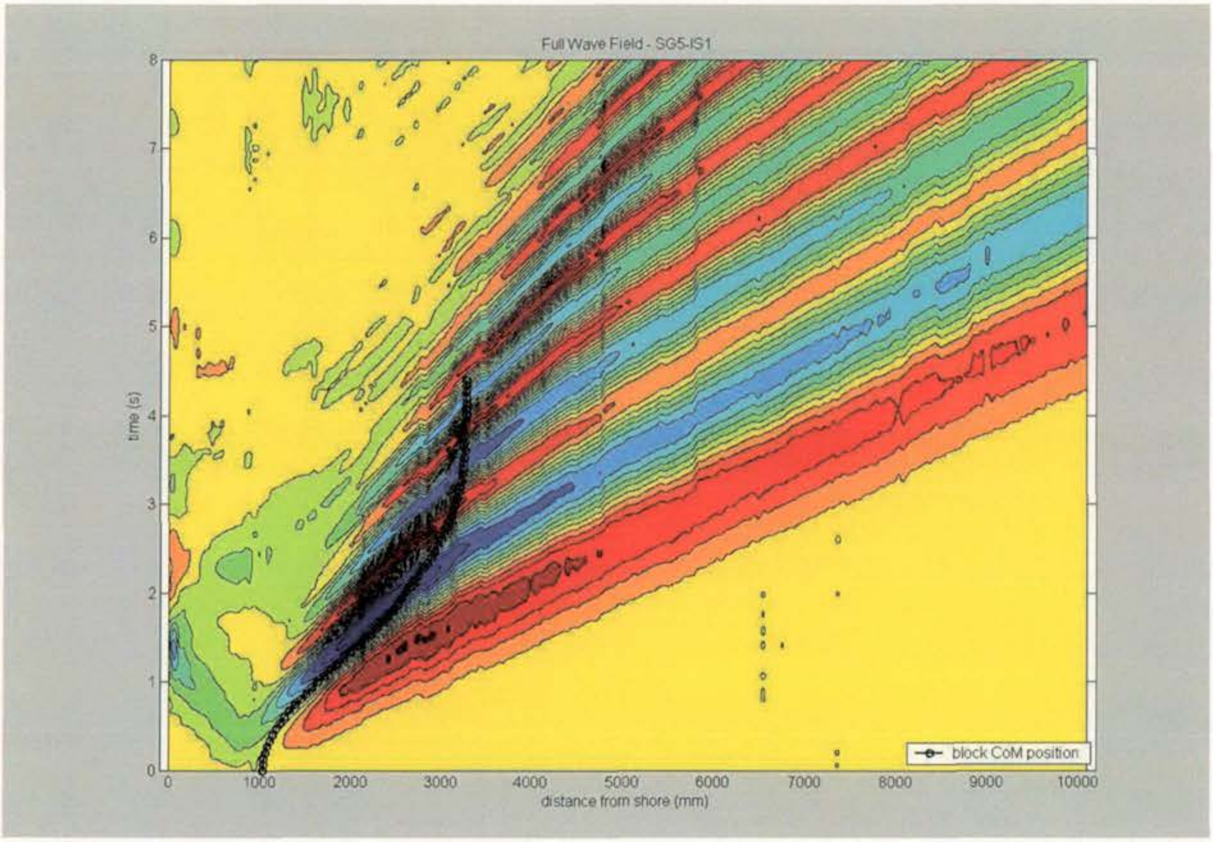

Figure A.20. 2-dimensional water level contour plot for the SG5_IS1 test. Specific gravity=4.02 and initial submergence=0.5.

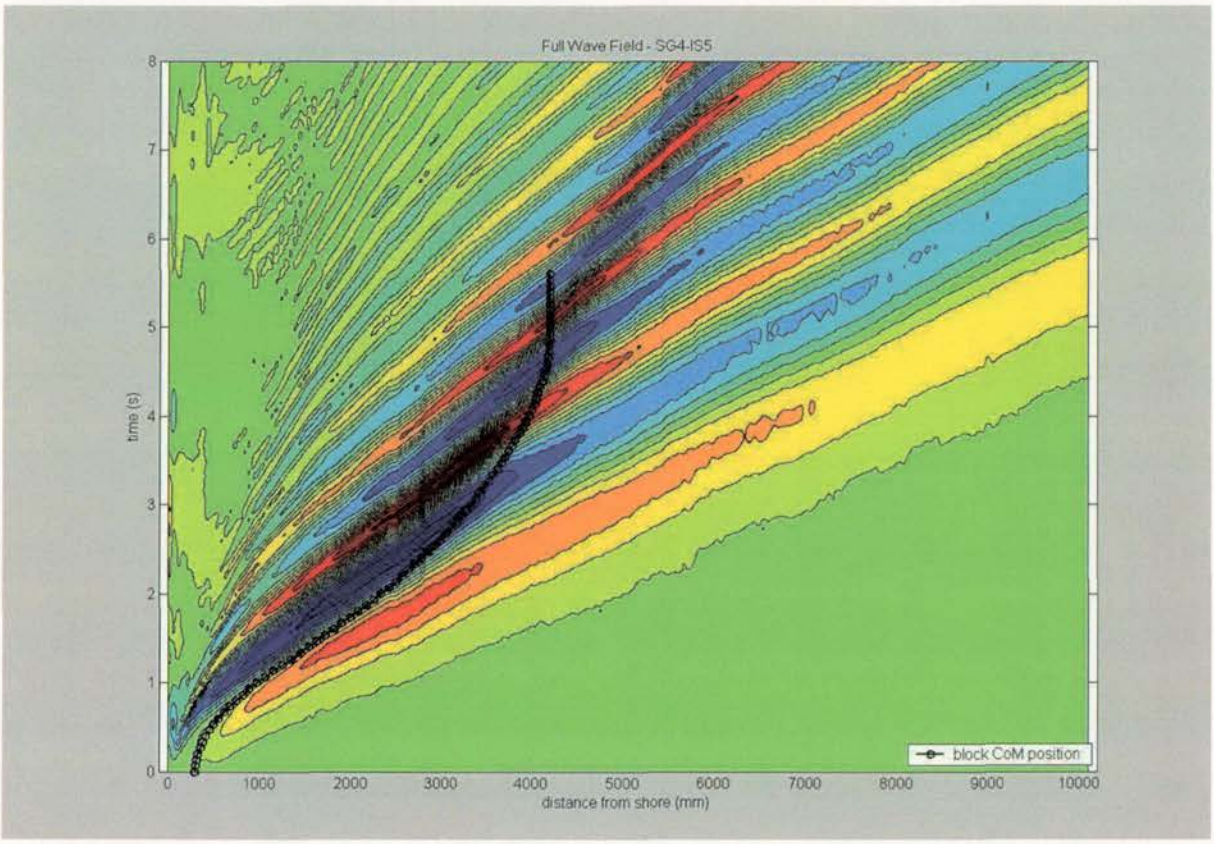

Figure A.21. 2-dimensional water level contour plot for the SG4_IS5 test. Specific gravity=3.42 and initial submergence=0.1.

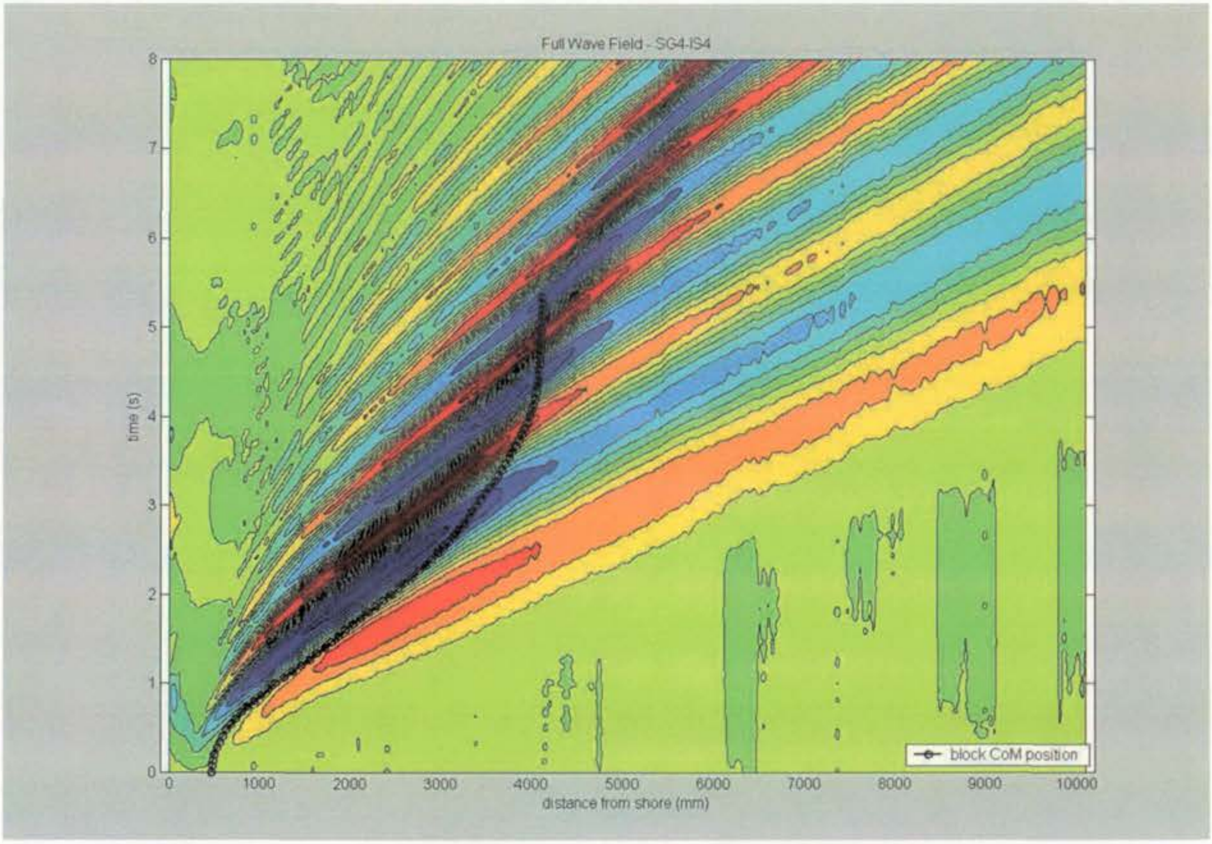

Figure A.22. 2-dimensional water level contour plot for the SG4_IS4 test. Specific gravity=3.42 and initial submergence=0.2.

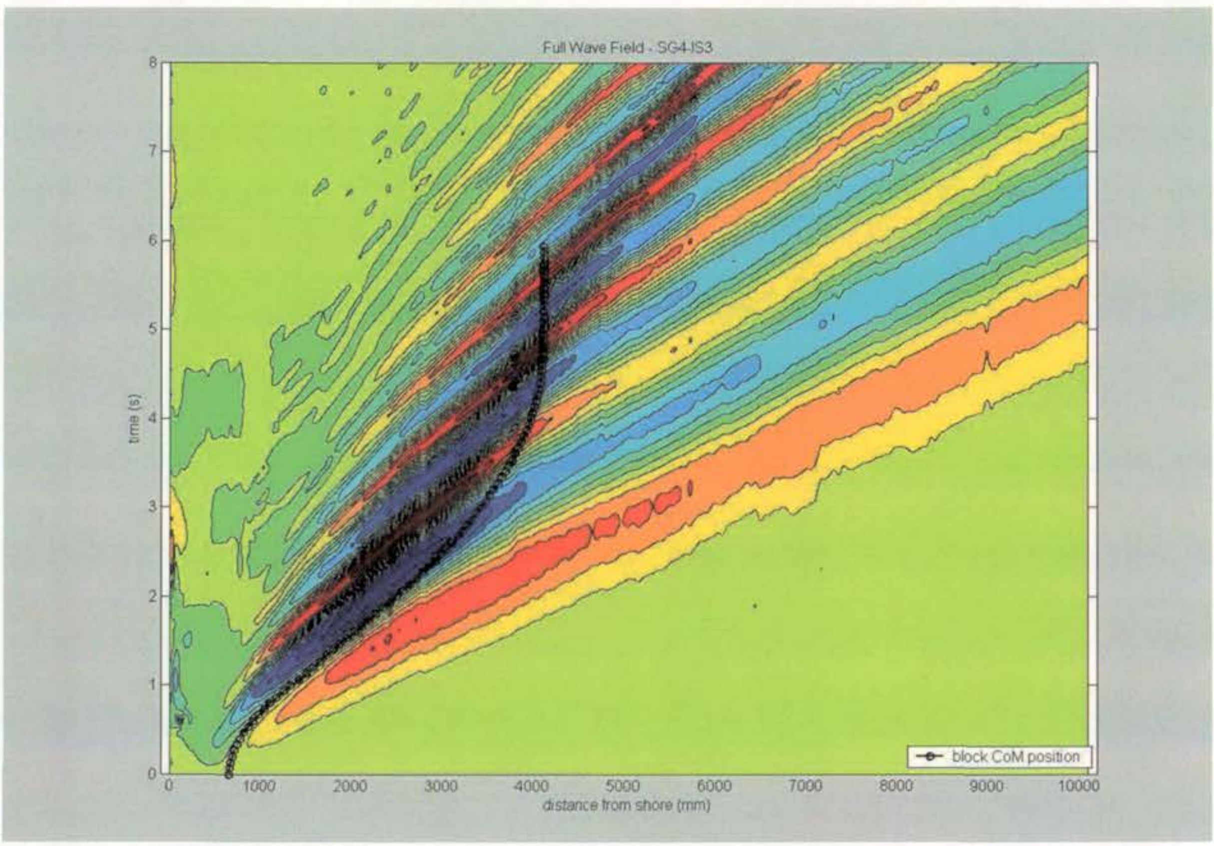

Figure A.23. 2-dimensional water level contour plot for the SG4_IS3 test. Specific gravity=3.42 and initial submergence=0.3.

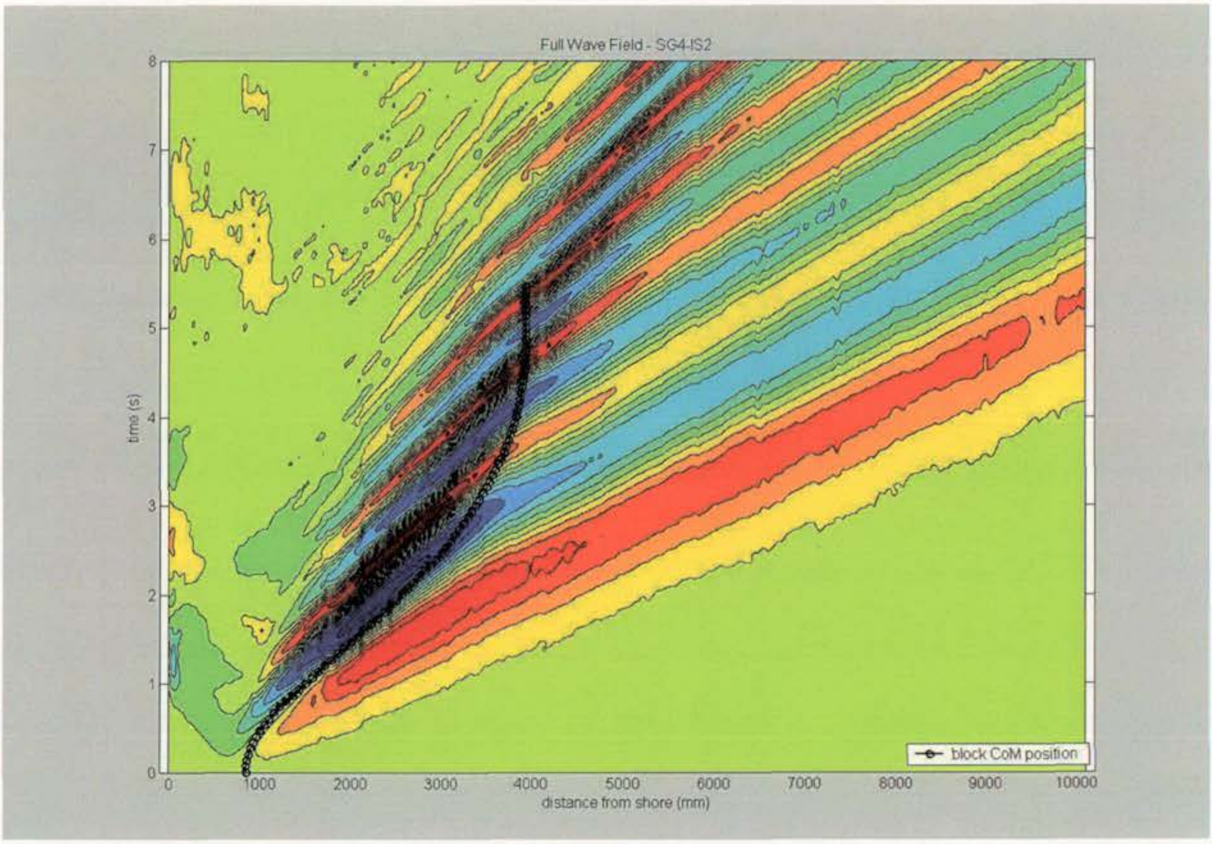

Figure A.24. 2-dimensional water level contour plot for the SG4_IS2 test. Specific gravity=3.42 and initial submergence=0.4.

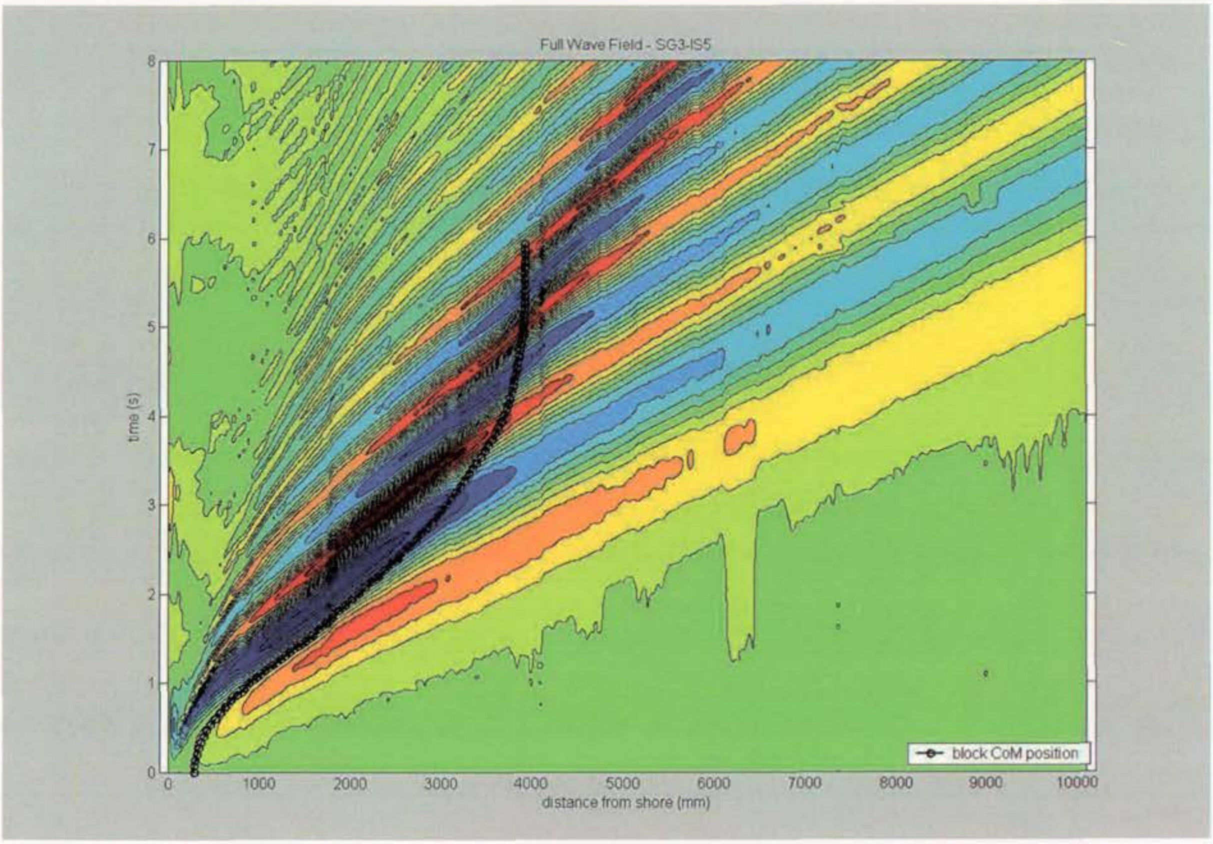

Figure A.25. 2-dimensional water level contour plot for the SG3_IS5 test. Specific gravity=2.83 and initial submergence=0.1.

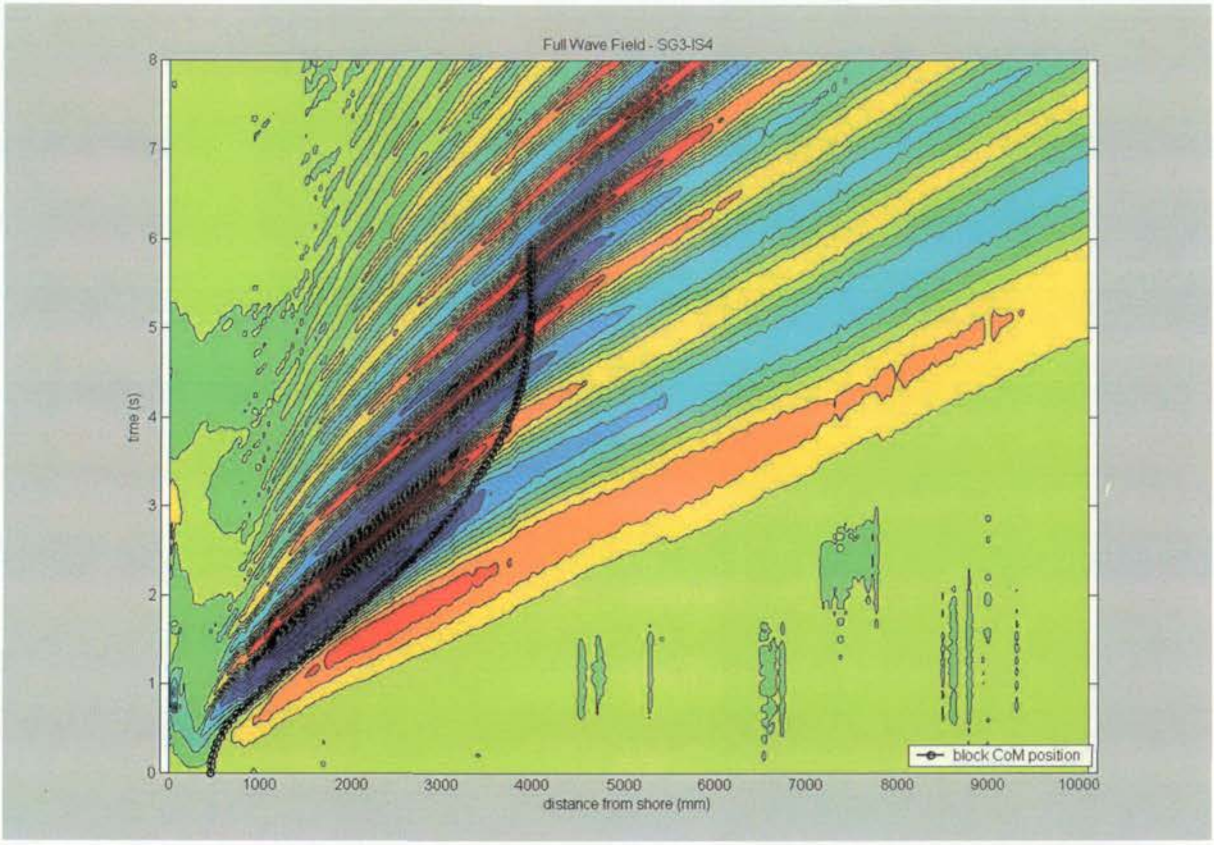

Figure A.26. 2-dimensional water level contour plot for the SG3_IS4 test. Specific gravity=2.83 and initial submergence=0.2.

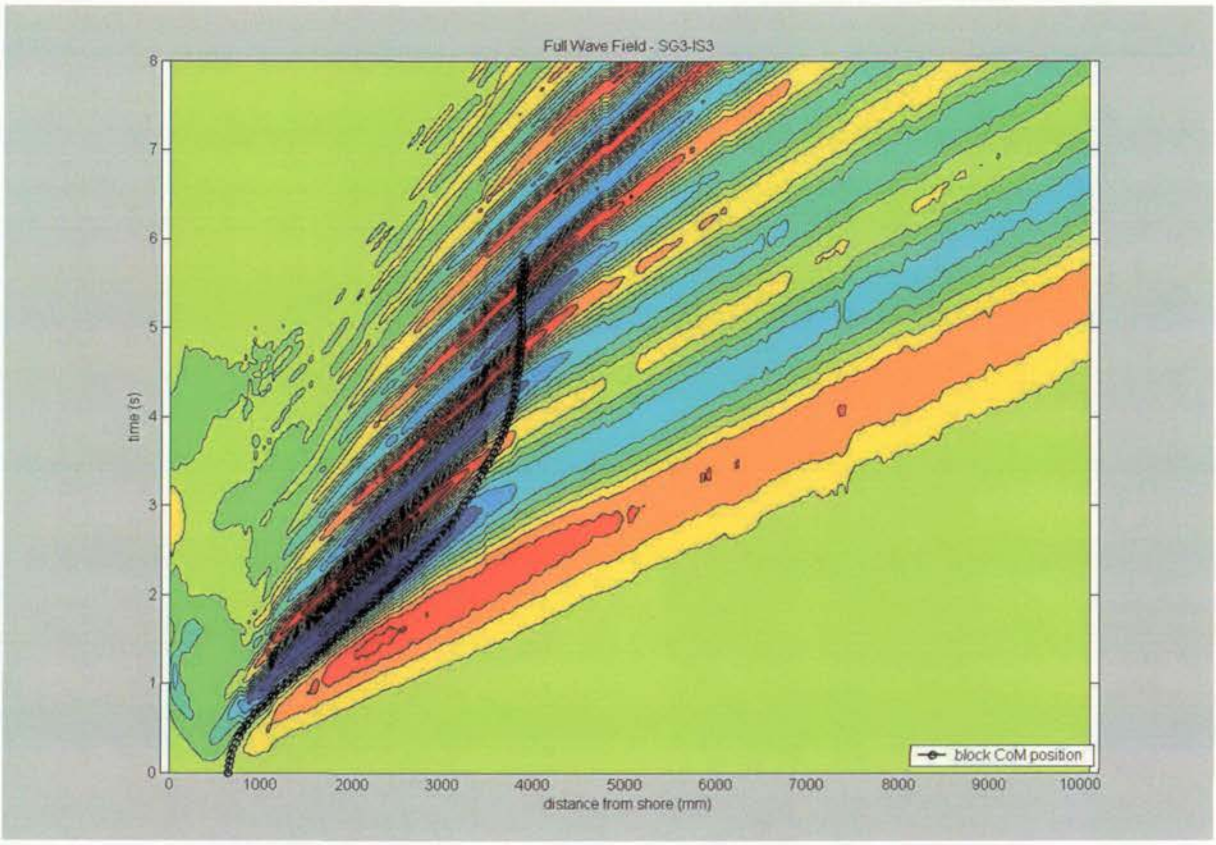

Figure A.27. 2-dimensional water level contour plot for the SG3_IS3 test. Specific gravity=2.83 and initial submergence=0.3.

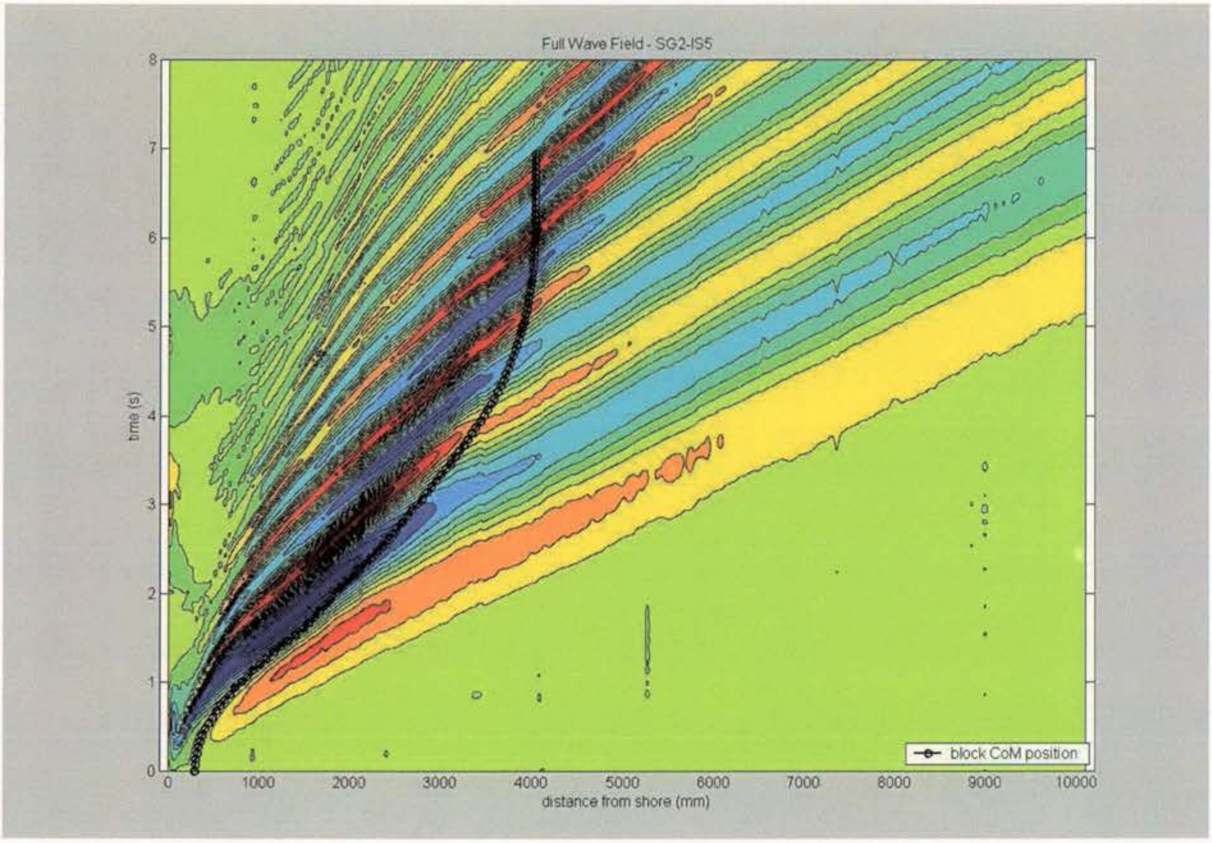

Figure A.28. 2-dimensional water level contour plot for the SG2_IS5 test. Specific gravity=2.23 and initial submergence=0.1.

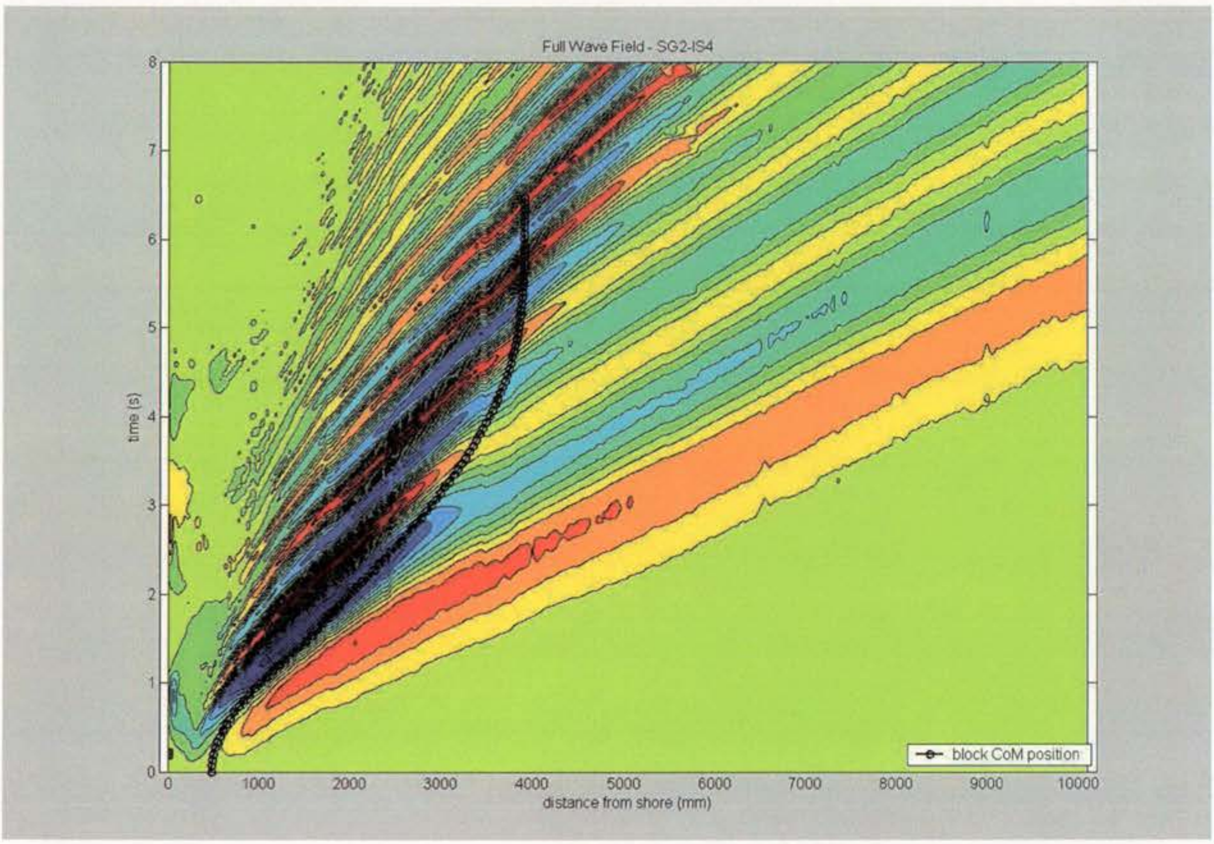

Figure A.29. 2-dimensional water level contour plot for the SG2_IS4 test. Specific gravity=2.23 and initial submergence=0.2.

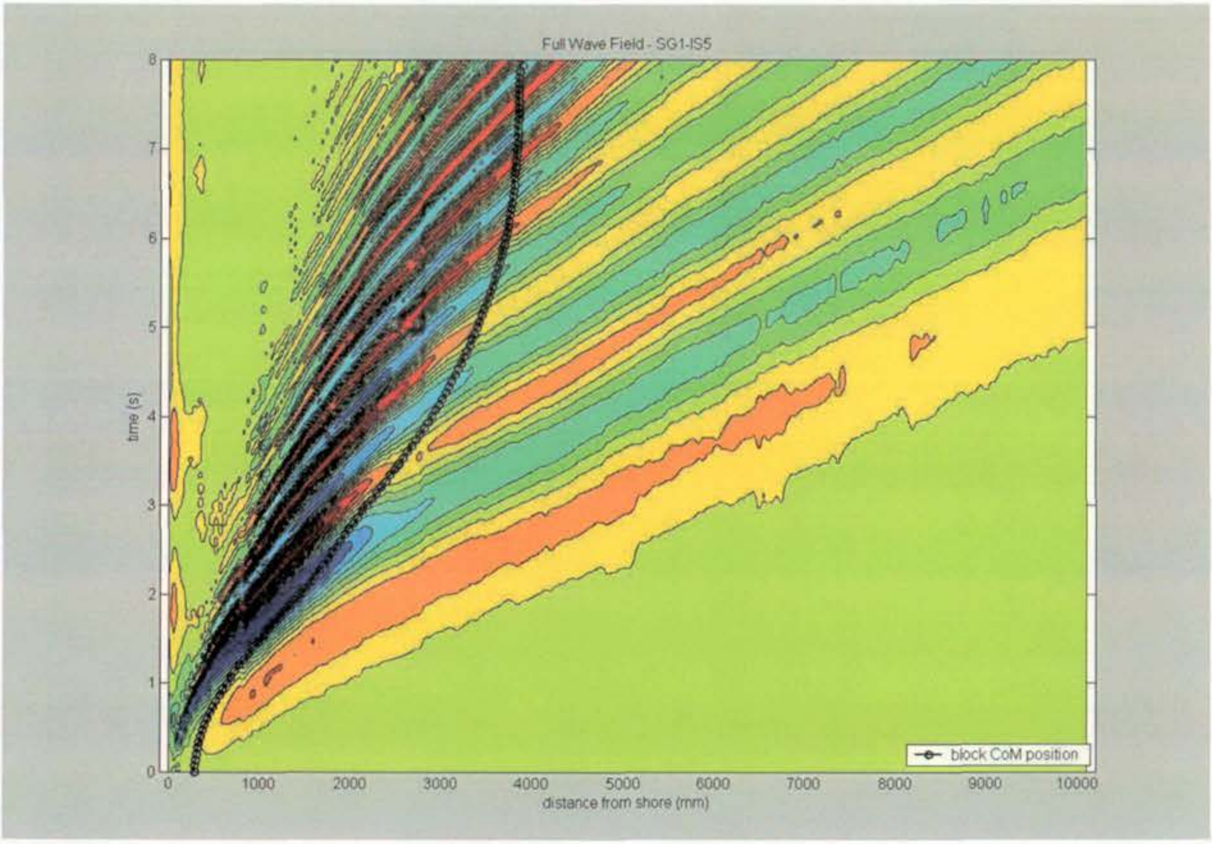

Figure A.30. 2-dimensional water level contour plot for the SG1_IS5 test. Specific gravity=1.63 and initial submergence=0.1.